EXPERIMENTAL AND COMPUTATIONAL STRATEGIES FOR ENHANCING MASS TRANSPORT AND CRYOPRESERVATION OF BIOLOGICAL TISSUES

by

Balasubramanian Karthik Kumar

A dissertation submitted to the faculty of
The University of North Carolina at Charlotte
in partial fulfillment of the requirements
for the degree of Doctor of Philosophy in
Mechanical Engineering

Charlotte

2012

Approved by:

_____
Dr. Robin N. Coger

_____
Dr. Charles Y. Lee

_____
Dr. Laura W. Schrum

_____
Dr. Ahmed El-Ghannam

_____
Dr. Xiuxia Du

ABSTRACT

BALASUBRAMANIAN KARTHIK KUMAR. Experimental and computational strategies for enhancing mass transport and cryopreservation of biological tissues (Under the direction of Dr. ROBIN N. COGER and Dr. CHARLES Y. LEE)

A bioreactor is a large-scale engineered *in vitro* device that maintains a 3D arrangement of functioning cells for use in various bioengineering applications. The current work is focused on heat and mass transfer issues related to the bioreactor's performance and applications. Firstly, for bioreactors to achieve high functional output, the cells within its 3D tissues constructs must have adequate supplies of nutrients and gases (O_2, CO_2 etc). Among these, O_2 transport has been a major challenge since regions of hyperoxia and hypoxia can develop. Hence, in the first phase of this work, an O_2 transport based computational model is proposed to help simulate the distribution of O_2 through the volume of the 3D tissue constructs under various operational conditions. The advantage of such a predictive model is that it can supply preliminary data, helpful for optimizing O_2 delivery to the cells. Secondly, the off the shelf availability of the cells and tissues utilized in the bioreactors is maintained mainly through cryopreservation techniques. In the case of large tissues, cryopreservation success is governed by the cryopreservation protocol used. Therefore, in the second phase of this work, a user friendly computational tool able to predict and compare the effectiveness of various cryopreservation protocols is developed. The computational tool's predictions are briefly validated against experimental results to verify its predictive accuracy. The package is designed to offer a cost effective solution for designing protocol's for cryopreserving 3D tissues and tissue equivalent. Thirdly, with specific relevance to the cryopreservation of liver cells and tissues, it was hypothesized that increased aquaporin (AQP) (integral

membrane proteins which aid water transport) expressions on the cellular membrane would improve cellular water transport and thereby improve the cryopreservation efficiency. Experimental results showed increased cell viability following cryopreservation of liver tissues equivalents treated for translocation of AQPs to the cellular membrane, thus confirming the hypothesis to be true. Overall, the computational and experimental strategies proposed in the current work would help enhance heat and mass transport to biological tissues, resulting in potential improvement in the performance of bioreactors and other large scale tissue replacement systems.

ACKNOWLEDGMENT

I would never have been able to finish my dissertation without the valuable guidance of my committee members, help from friends and support from my family.

I would like to express my deepest gratitude to my advisor, Dr. Robin Coger, for her excellent guidance, intellectual support and constant encouragement. Her outstanding mentoring coupled with care, patience and inspiration has been critical throughout the course of my research and I will be forever indebted to her. I would also like to express my utmost gratitude to my co-advisor, Dr. Charles Lee, for his dedication of time and efforts and his valuable guidance that enabled me to complete my dissertation. Without the help of his numerous animal surgeries, the experimental part of this dissertation would never have been possible to complete.

I would also like to thank Dr. Laura Schrum, for her important contribution, comments and guidance, which were crucial for the completion of the last part of this dissertation. My sincere thanks go to the rest of my committee members, Dr. Ahmed El-Ghannam and Dr. Xiuxia Du for agreeing to be on my committee and for reviewing this dissertation.

I feel fortunate to be blessed with many wonderful friends who have helped and supported me throughout the course of my research and would like to extend my sincere thanks to all of them.

Finally I would like to acknowledge National Institute of Health (NIH #1R21 EB004982-01A11) and Carolinas Medical Center for funding my research work.

DEDICATION

To my beloved parents, Balsubramanian K and Indrani B.

TABLE OF CONTENTS

LIST OF FIGURES

LIST OF FIGURES

LIST OF ABBREVIATIONS

3D	Three-dimensional
ANOVA	Analysis of variance
AQPs	Aquaporins
BALs	Bioartifical liver devices
Bt_2cAMP	DiButyly cyclic adenosine monophosphate
cAMP	Cyclic adenosine monophosphate
CFD	Computational fluid dynamics
CPA	Cryoprotective agent
DBMS	Database management system
DMEM	Dulbecco's modified eagle medium
DNA	Deoxyribonucleic acid
ECM	Extracellular matrix
FBS	Fetal bovine serum
HBSS	Hanks buffered salt solution
$HgCl_2$	Mercuric chloride
HTML	Hypertext markup language
IIF	Intracellular ice formation
IMCD	Inner medullar collecting duct
MEM	Minimum essential medium

MMT	Multi-scale modeling tool
mRNA	messenger ribonucleic acid
pO_2	Oxygen partial pressure
PBS	Phosphate buffered saline
PCR	Polymerase chain reaction
PFCs	Perfluorocarbons
PIIF	Probability of intracellular ice formation
PTFE	Polytetrafluoroethylene
RNA	Ribonucleic acid
RT PCR	Reverse transcription polymerase chain reaction
UV	Ultraviolet
XML	Extensible markup language

LIST OF SYMBOLS

Symbol	Description	Unit
L	Latent Heat of fusion	kJ
A	Area	m^2
h	Height of the liquid column	m
Q	Volumetric flow rate	m^3/s
$D_{i,m}$	Diffusivity of the *i*th substance in medium m	m^2/s
S_m	Source of mass generation	kg/m^3s
p	Partial pressure	-
k_{eff}	Effective heat diffusivity	W/m K
E	Heat Energy	J
φ	Concentration of the oxygen	-
C	Coefficient of resistance	-
μ	Viscosity of the liquid	kg/(m·s)
S_{oxy}	Oxygen consumption rate	kg/m^3 s
R_{oxy}	Oxygen consumption rate per cell	kg/m^3 s
ρ	Density of the substance	kg/m^3
Y_i	Mass fraction of the substance	-
$\vec{V}$	Velocity vector	m/s
γ	Porosity	-
N	Number of cells	-
Vol	Volume	m^3
C_l	Specific heat capacity of the liquid	kJ/kg K

T_m	Melting temperature	K
T_{sol}	Temperature at the end of solidification	K
T_{liq}	Temperature at the beginning of solidification	K
μ	dynamic viscosity	kg/(m·s)
ρ	Density	kg/m^3
c	Concentration of the CPA	mol/m^3
V_{is}	Volume of the cell	m^3
R	Universal gas constant	J/mol K
v_s	Disassociation coefficient	-
n_s, n_d	Number of moles of salt, CPA	-
L_p	Hydraulic permeability	$m^3/N\ s$
ΔH_f	Latent heat of fusion for water	kJ/mol
$A(t)$	Effective plasma membrane surface area	m^2
I	Nucleation rate	-
Ω	Kinetic rate coefficient	$m\text{-}^2s^{-1}$
L_{pg}	Hydraulic permeability at 273K	$m^3/N\ s$
E_a	Activation energy to initiate water transport	J

CHAPTER 1: INTRODUCTION

Tissue engineering is a field that aims to address the clinical problem of tissue failures in the human body. It combines the principles and methods of engineering and life science for the purpose of designing and developing biological replacements to restore, maintain or improve the functions of tissues or organs [1]. It involves understanding the principles, behavior and functions of cells, tissues and/or organs and applying it to produce biological substitutes for structural and functional disorders of tissues and organs [2]. Tissue engineering utilizes the process of combining living cells with biomaterials for implementation in clinical applications such as therapeutic treatments, diagnostics and generation of *in vitro* tissues and organs for implantation [3], life support [4,5] and pharmaceutical testing [6,7].

One major challenge in the tissue engineering field is to develop devices to house, support and grow functional cells and tissues in large scales. This led to the development of bioreactors. Bioreactors are engineered devices or systems capable of maintaining a physiological environment for the growth of large number of cells and tissues [8]. One of the design configurations that has been used for these devices , supports functioning cells (e.g., liver hepatocytes or stem cells) immobilized in a porous scaffold or extra cellular matrix (ECM) – which will be referred to in this study as “tissue constructs”. The bioreactor facilitates the transport of nutrient and metabolites to these tissue constructs and also provides the necessary chemical and mechanical stimuli to sustain high cell functionality.

Bioreactors are used for a wide variety of applications ranging from the *in vitro* growth of cells/tissues for bioremediation [3, 9, 10]; to extracorporeal patient support devices (eg: Bio-artifical liver devices) [4, 5, 11, 12]; to pharmaceutical test devices [6, 7, 13, 14]. With such a variety of applications, various types of bioreactors have been developed for the tissue engineering of tissues including skin [15], liver [9, 11, 12], muscles [10], retina [16], and cartilage [17]. Fig 1.1 shows some of the types of bioreactors used. The difference in the designs of these bioreactors are based on a number of different factors such as the bioreactors' requirements and applications, the type of cell/tissue employed, the scaffold choice, its mass transport properties, etc.

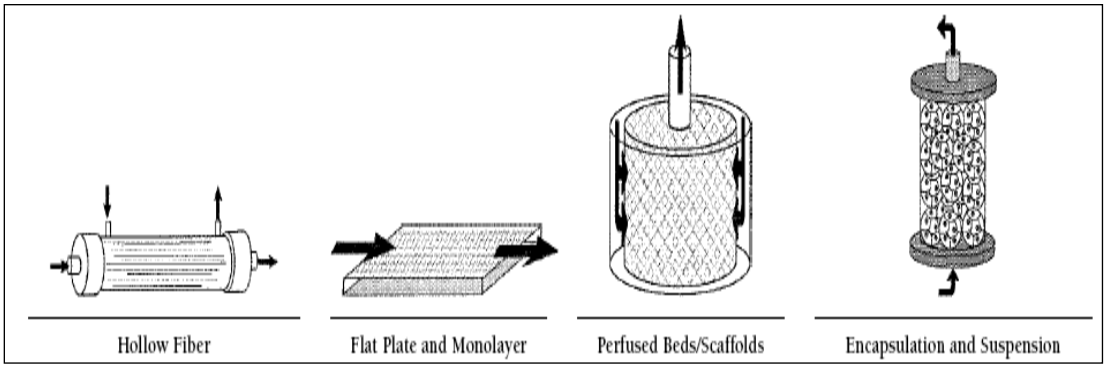

FIGURE 1.1: Examples for some of the bioreactor designs. The arrow indicates the direction of media flow within the device. Reprint from [18].

However, despite of the advent of different types of bioreactors, its capability and applications are currently restricted by a number of factors. Some of the limiting factors include: total number of cells that can be supported, cell density, transport of adequate nutrients and metabolites, off the shell availability, ease of use etc. Therefore, in order to address these limitations, there is a need for developing new strategies and techniques in the field of Tissue Engineering.

In the current work, two major factors that restrict the capability and utilization of bioreactors are analyzed. Firstly, the functional performance and efficiency of a

bioreactor is mainly limited by its mass transport capabilities, i.e., the ability to transport nutrient, O_2, CO_2, waste, etc. to and from cells. Among these, viability and function of cells in the bioreactors have been found to be particularly sensitive to the quantity of oxygen (O_2) to which the cells are exposed [19]. Exposure of the cells to low levels of O_2 (i.e., hypoxic conditions) results in decreased cell function as well as cell death [20-22]. Contrastingly, exposure to very high levels of O_2 (hyperoxic condition) can lead to oxidative stress resulting in deteriorating cell function [23, 24]. Thus the effectiveness and efficiency of a given bioreactor design is at least partially dependent on its ability to sustain optimal O_2 levels required of cells being supported within its 3D cellular space.

Unfortunately, this task has proven to be a major challenge [25]. For those designs that rely on liquid-based nutrient flows (e.g., blood, plasma, nutrient media, etc..) as the main source of O_2 to the cells of the bioreactor, O_2 content then gets transported to the cells through permeation, diffusion, and/or convection [22, 26-28]. This transport of O_2 to the cells is thus affected by multiple factors specific to the bioreactor's design. For instance, for bioreactor designs consisting of ECM, transport properties of the ECM add resistance to O_2 diffusion from the source flow to the cells. Also the O_2 capacity of the source (i.e., the nutrient media) and the rate, in which it is replenished, influence the level of O_2 available to the cells. Then the continuous consumption of O_2 by the cells reduces the levels of O_2 available to adjacent cells within the cell space [29]. Consequently, if the thickness of the 3D cell space within a given bioreactor is not optimized, there will be heterogeneous O_2 transport across the thickness resulting in regions of hypoxia [30]. Such hypoxic conditions can lead to poor cell viability and function, resulting in deterioration of the bioreactor's performance and effectiveness over time.

These challenges to O_2 transport in bioreactors have been identified and addressed by various research groups in the literature. One solution involves increasing the supply of O_2 to the cells by introducing additional sources of O_2. This can be done by increasing the level of O_2 in the supply media [31], introducing oxygenators [32, 33], incorporating O_2 generating materials [19, 34, 35], etc. Another solution is to improve the O_2 transport mechanism. This can be achieved by improving the diffusive and convective properties within the bioreactor by using various flow conditions and patterns, by employing different ECM materials, and by enhancing the diffusivity of the ECM [36-39]. Additionally, to elucidate the dynamics of O_2 transport in bioreactors, several mathematical and computational models have been developed [26, 27, 40, 41]. Yet effective tools for quantifying and visualizing the O_2 available to the cells housed within their 3D spaces are still needed. Such a capability would enable the cells' functional output to be quantitatively correlated to the degree of O_2 exposure. It would also provide valuable information for use in optimizing bioreactor designs to enhance their performance and effectiveness.

In Chapter 2, Computational Fluid Dynamics (CFD) based modeling [42] is utilized to quantify and visualize the O_2 distribution in relevant 3D cell spaces. The CFD-based computational model of this study is developed around a simple experimental test setup that incorporates key basic features common to many bioreactor designs. The test system enables experimental conditions such as flow conditions, type and number of cultured cells, ECM material, dimensions of the 3D cell space, level of O_2 content in the supply media etc., to be varied as needed. Next, a steady state, CFD-based O_2 transport model based on this test setup, and quantified by the Navier Strokes and mass transport

equations, was developed. The model combines approaches presented by Ledezema et al [43] which uses the Navier Stokes equation to simulate and predict steady state O_2 transport in a radial micro-channel and that of Williams et al [44] which uses CFD to compute steady state momentum and mass transport of O_2 in a bioreactor for cartilage tissue engineering.

Furthermore, to aid the model's adaptability for broader use, the CFD model of this study was deliberately built using a commercially available software platform. Consequently, the model's results can be correlated and extended to the cell spaces of various bioreactors designs, to provide preliminary and predictive O_2 transport information. Because of its predictive capabilities, the model can be used as an effective tool in understanding the mechanism of O_2 transport within a bioreactor system; and in the planning and development stages of new bioreactors.

Another factor that influences the applicability of bioreactors for clinical uses is the off-the-shelf availability of cells/tissues. The off-the shelf availability of the cells/tissues is critical to enabling physicians to treat the patients with tissue failures as the need arises. One method that addresses this issue is the use of cryopreservation techniques to safely store cells and tissue at sub-zero temperatures then thaw them for use.

Cryopreservation is a branch of cryobiology [45], where cryopreservation techniques are usually carried out in the presence of cryoprotective agents (CPAs). The CPAs are high molecular weight chemicals that help prevent cell damage during the cooling process. These CPAs protect the cells by increasing the solute concentration in the cells and lowering the freezing point temperature of the intracellular water [46].

Traditionally, cryopreservation techniques are carried out via two methods, either by vitrification or by the freeze-thaw method. Vitrification is a cooling process in which a liquid solidifies into an amorphous glass state [47]. It requires very rapid cooling (~10000 ^{0}C/min) of the liquid sample to its glass transition temperature. Care should be taken to maintain a high viscosity of the sample to avoid crystallization. Consequently, vitrification processes require high concentrations of cryoprotectant agents to avoid crystallization and achieve the desired vitrified form. Introduction of such high concentrations of CPAs can lead to toxicity in the cells and tissue and also cause osmotic stress due to excessive dehydration of the cells [48], all of which are magnified when seeking to vitrify large 3D tissues and tissue equivalents. Hence, vitrification in practice has most commonly been applied to the cryopreservation of cell suspensions and small tissues.

Freeze-thaw cryopreservation methods involve transitioning biological samples from the liquid phase to the ice phase and back under controlled thermal conditions, known as cryoprotocols, using either constant cooling/warming rates or by applying a sequence of cooling/warming rates over time. These cryoprotocols have been demonstrated to be successful for cryopreserving cartilages, sperm, skin, embryos, blood and suspensions of liver cells [49-53]. Yet with larger 3D tissue equivalents and organs, the process is complicated by cell damage due to the escalation of several possible occurrences: 1) The formation of extracellular ice could cause mechanical damage and rupture the cell membrane; 2) Excessive dehydration of the cell; 3) Solution effects that expose the cells to heightened solute concentrations, especially during slow cooling processes; and 4) The formation of intracellular ice effects due to either supercooling or

the development of high osmolarity gradients [54, 55]. Among these the latter, intracellular ice formation (IIF), has been found to be the most common cause of cell damage during freeze-thaw cryopreservation processes.

Furthermore, the cryopreservation of 3D tissues and organs has inherent problems due to the large dimensions as compared to individual cells and suspensions. Different regions within the tissue/organ can experience different thermal and concentration histories during the process of freezing, leading to differences in cell survival at various regions [56]. As such, the thermal and concentration histories are dependent on the cryoprotocol adopted for the freezing process. Therefore, an understanding of the thermal and concentration histories associated with various protocols, and the corresponding biophysical processes that govern freeze injury, can be useful to achieving the safe cryopreservation of 3D tissues or organs.

Currently, the development of cryoprotocols for tissues is largely achieved through empirical approaches. Such empirical approaches involve high costs and time, thus emphasizing the need to utilize computational models to predict and analyze the effects of cryoprotocols in cryopreserving tissues. Although many cryopreservation relevant computational models already exist [57-60], most of them are based on specific devices, application or experimental conditions, limiting their potential for use by persons who are not specialists in the field of cryobiology, yet interested in cryopreserving biological samples. Members of the clinical, research, and commercial communities in this category require a user-friendly model to aid them in the design of effective cryoprotcols.

Chapter 3 describes the development of one such user friendly mutli-scale computational model that seeks to optimize freeze-thaw cryopreservation protocols for 3D tissue samples. The multi-scale modeling tool (MMT) is designed to predict the cell injury occurring due to IIF based on the thermophysical events the sample experience during the freezing process.

The MMT was developed by combining two sub-models. The macro sub-model was based on the work by Balasubramanian and Coger [61] which predicts the temperature and concentration (for CPA) distribution within the sample at any point of time during the freezing process, for a given cryoprotocol. The temperature distribution over time within the sample is modeled based on the heat transfer equation and incorporated solid-liquid phase transition which takes place during the freezing process [62]. The concentration distribution of CPA is governed by the mass transport equation [63]. These equations are discretized and solved using successive relaxation method in Matlab.

The micro sub-model of the MMT was developed based on Mayur's model [64], and makes use of the thermal and concentration gradients acquired from the macro sub-model. Based on the thermal history experienced by the sample, the micro sub-model predicts the cellular water transport and the probability of IIF within the sample. The micro sub-model utilizes nucleation theory [65] and the water transport equation [66] to predict cell survival from the probability of IIF. Furthermore, the MMT is coupled to a HTML and database management system (DBMS), thus making it user friendly and easy to use. The user friendly feature enables practitioners with minimal computational capabilities and technical background to use the MMT. As such, the MMT

computational model was designed to enable practitioners to identify the best suitable freezing protocol for safely storing their tissue samples – thus reducing cryopreservation cost and time.

The predictive capability of the MMT was then compared to experimental results to verify the accuracy of the model. During the process, isolated rat hepatocytes were cultured on a collagen gel ECM and subjected to two different cryoprotocols. The frozen samples were then thawed back after 3 days in -80^{o}C, and a Live/Dead assay was used to estimate cell viability. The experimental results where then compared to the predictions from the computational model to establish the accuracy of the MMT model.

Completion of the MMT's validation experiments also had another benefit. It revealed that the post-thaw viability of the hepatocytes seeded in the collagen gel matrix was significantly less than the viability of cell suspensions reported in literature. To date, while the cryopreservation of hepatocytes has yielded considerable success for individual cells and cell suspensions, the successful cryopreservation of liver tissue or tissue equivalents still presents challenges. One of the reasons is that the probability of IIF formation has been found to be high for liver tissue equivalents compared to the liver cell suspensions, thus resulting in low viability of cells [67, 68]. Hence accomplishing the successful cryopreservation of liver tissue and tissue equivalents by reducing the probability of IIF is a step towards the safe storage of whole livers.

One method of reducing the probability of IIF during cryopreservation of liver tissue is by improving its water transport properties. Theoretically, during freezing, the extracelluar space becomes more concentrated and water permeates out through the cell membranes due to osmotic gradients. This process continues until a crystalline ice form is

achieved. However, if water permeation rate though the cell is low, the increasing osmotic gradient causes intracellular water to freeze, resulting in IIF [54, 55, 66]. Therefore, if the water permeability of the cell membrane can be increased, the probability of IIF may be considerably reduced.

In fact, the permeability properties of the cell membrane of hepatocytes have been found to be less than that of kidney, embryos, oocytes – all of which have been successfully cryopreserved [69-72]. Generally, water movement through the cell membrane occurs through aqueous pores created by hollow protein cylinders embedded in the membrane and through direct diffusion across the lipid bilayer [73]. There are also a variety of water transport pores, known as aquaporins, that exists in certain cells. Aquaporins (AQPs) are water transport channels embedded in the cell membrane [74]. The presence of such water channels can assist in transporting of water in and out of the cells in accordance to the osmotic changes that occur during croprotocols [75]. Manipulation of AQPs can aid in preventing intracellular ice toxicity as well as IIF during freeze-thaw processes.

Such a strategy for regulating AQPs in the cellular membrane for cryopreservation has been successfully performed for oocytes, larvae and embryos [70-72, 76]. In these cases, the cells were treated to artificially express AQP3 prior to cryopreservation, and the post thaw survival rate was found to be significantly high. Similarly, regulation of AQPs during cryopreservation of kidney IMCD cells has been conducted [69] and it was seen that upregulation of AQPs resulted in a 25% increase in viability whereas down-regulation of AQPs resulted in a 55% decrease in viability.

However, no such research has been reported for hepatocytes despite the fact that AQPs are known to exist in hepatocytes.

In primary rat hepatocytes, aquaporins AQP0, AQP8, AQP9, AQP11 and AQP12 are known to exist. AQP0 is found mainly in the intracellular space and does not express itself on the cell membrane [77]. Little is known about AQP11 and AQP12. Hence AQP 0, 11 and 12 are not currently considered to be significant to cryopreservation goals. AQP9 is located on the basolateral side of the cell membrane [77, 78] but cannot be regulated. Yet AQP9, also known as an aquaglyceroporin, is a major transport channel for glycerol [79], a fact that can be taken advantage of during cryopreservation of liver slices when glycerol is used as the cryoprotective agent (CPA). AQP8 is present in large extent in the pericanalicular vesicles in the intracellular space, and also appears on the apical side of the cell membrane. However, the AQP8 present in the pericanalicular vesicles can redistribute themselves on the apical side of the cell membrane under the influence of a choleretic stimulus such as Bt_2cAMP and glucagon [77, 80]. Hence AQP8 is the aquaporin type in liver that is most significant to cryopreservation and water transport regulation goals. Therefore, Chapter 4 of this dissertation focuses on experimentally verifying the hypothesis that translocating AQPs in hepatocytes can increase the cryopreservation success of liver tissue equivalents.

Specifically, rat hepatocytes cultured in collagen gel ECM were treated with choleretic stimulus (Bt_2cAMP/ glycerol) to initiate translocation of AQP8, and with $HgCl_2$ to inhibit the water channels [81]. The treated and untreated (controls) were then subjected to a freeze-thaw process with DMSO/glycerol as the CPAs. The results indicate

a significant increase in the cell survival rate due to the increased AQPs quantity on the cellular membranes. Thus the hypothesis was found to hold true for hepatocytes.

To summarize, this dissertation explores two important strategies for improving the capabilities and applicability of bioreactors in clinical use: 1) Assisting in developing better bioreactor designs by implementing an O_2 transport model to understand and analyze the distribution of O_2 within such systems; and 2) Aiding the success of cryoprotocols for storing cells/tissues, thereby advancing the off-the-shelf availability of cells/tissues for use in bioreactors and other applications. Furthermore, Chapter 4 focuses specifically on the cryopreservation of liver tissue, introducing a new experimental strategy to improve its cryopreservation efficiency.

CHAPTER 2: OPTIMIZATION AND VISUALIZATION OF OXYGEN TRANSPORT IN BIOREACTORS USING COMPUTATIONAL MODEL

2.1 Summary

The availability of suitable levels of oxygen (O_2) to the cells maintained within tissue bioreactors is critical to their functionality and performance. Hence having a good understanding of the O_2 transport mechanism and O_2 distribution throughout the cell space of such systems is valuable to optimizing their performance. This can be achieved with the help of predictive computational models. In the current chapter, transport of O_2 and its distribution in a 3D cell space configuration is modeled computationally. The model investigates the O_2 transport through a porous cell space by the mechanisms of convection, permeation, and diffusion of the O_2 dissolved-media circulated through the device. The model's accuracy in predicting transport was first confirmed by comparison with experimental results, and then applied to the study of O_2 transport within a liver tissue bioreactor system. The computational model captures the dynamics of nutrient media flow through the bioreactor system. The model also predicts the level of cellular O_2 exposure as a function of position within the 3D cell space. This enables the identification and visualization of hypoxic, normoxic and hyperoxic regions with the 3D cell space. The results show hypoxic regions existing near the walls of the bioreactors wherein the media flow is restricted by boundary layer effects. This suggests that the cells' survival and thereby their functionality are most successfully maintained in those regions more thoroughly perfused with media. The current work also analyzes the

penetration characteristics of O_2, with respect to the media's flow dynamics, its dissolved O_2 levels, and the number of cells within the cell space. This can subsequently be used to develop and test design criteria -- such as the optimum O_2 content of the inlet media and the relationship between cell seeding density and maximum cell survival for a range of flow and cell culture conditions -- of future bioreactor systems. As such this predictive model has the potential to aid tissue engineers in the design and optimization of future bioreactor systems.

2.2 Introduction

Bioreactors are *in vitro* devices for maintaining cultured cells. These devices have become increasingly important due to their ability to perform the critical functions of the natural cell-based systems they seek to replicate [8]. Bioreactors are typically used for three main applications: 1. Maintenance of cell sources to carry out chemical processes (e.g., bioremediation applications) [82]; 2. Pharmaceutical testing [83]; or 3. As temporary extracorporeal organ replacement devices to bridge patients until a suitable organ transplant is available [84, 85]. For example, bioreactors consisting of hepatocytes have potential for use in extending the life of patients suffering from liver failure [4, 5].

With the increase in the usability of bioreactors in recent years, it is not surprising that various designs have been proposed. [83, 86, 87]. Despite the variations, the majority of the designs manage a large number of viable cells in a 3D arrangement with the goal of expressing high levels of functionality. Sustaining this performance output over a period of time requires the bioreactor to provide the cells it contains with adequate levels of nutrients and gases (O_2, CO_2, etc) [88]. Among these, the viability and function of cultured cells have been found to be particularly sensitive to the quantity of oxygen (O_2)

the cells are exposed to [89]. Existence of hypoxic and/or hyperoxic regions within the system might prove to be detrimental to the cells [20-24]. Thus, it is important to understand the mechanism of O_2 transport and also determine the distribution of O_2 for developing effective bioreactor designs.

In most bioreactors, the main source of O_2 is the nutrient media flow supplied to the device. The transport of this O_2 to the cell space of the bioreactor may be through permeation, diffusion, and/or convection [22, 26, 27, 90]. Such a transport of O_2 is affected by multiple factors. The current investigation identifies some of these factors and their effects on the O_2 distribution with a bioreactor system. This is achieved with the help of a Computational Fluid Dynamics (CFD) model.

The CFD model predicts the O_2 availability within 3D cell spaces when one or more of the factors affecting O_2 transport are varied. It also visually presents the O_2 distribution within the 3D cell space, to aid in identifying regions of normoxia, hypoxia, and hyperoxia. By employing such a model, bioreactor designers and practitioners can gain valuable information for selecting key variables such as the ECM choice, dimensions of the cell space, cellular density and O_2 content of the media prior to building the prototype or commencing an experiment.

In the current study, the model's capabilities are presented for the specific case of predicting O_2 transport for a cell space consisting of hepatocytes (i.e,. the parenchymal cell of the liver) seeded within collagen sponges.

2.3 Computational Methods

2.3.1 Design of the Test Device

The goal of this work is to present a computational model helpful for assisting in the design and interpretation of bioreactor experiments reliant on O_2 transport. Developing such a model required a complementary test setup for evaluating various experimental conditions. The key design criteria of the test setup were as follows:

- It must have a logical geometry, able to maintain both static and dynamic flows of nutrient medium.
- It must be able to sustain a 3D cellular space composed of cells packed within ECM for the duration of at least 3 days.
- It should enable the function of cultured cells to be assessed.
- The cell density and the thickness of the cellular space should both be adjustable.
- It should enable investigation of permeation and convection of media, through and across the 3D cell space, respectively.
- It should provide options for investigating multiple samples simultaneously, thus enabling the effects of ECM attributes, or the O_2 level in the medium, or the cell density in the cell space to be compared.

Fig 2.1 depicts the Pro E (PTC, Needham, MA) model of the generalized test device of this study. The device will be more fully described in the Materials and Methods section (2.4.1). Once the generalized test device was designed and developed, the next step in the modeling process was to develop its CFD analog. The CFD model was developed using Ansys 11 - CFD software packages [Ansys Inc, Canonburg, PA].

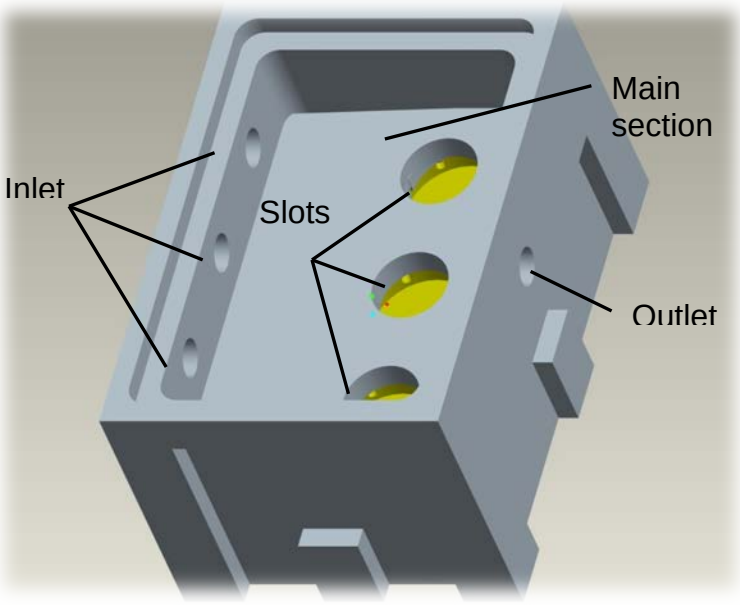

FIGURE 2.1: Pro-E design of the novel test device developed to test various experimental conditions[*].

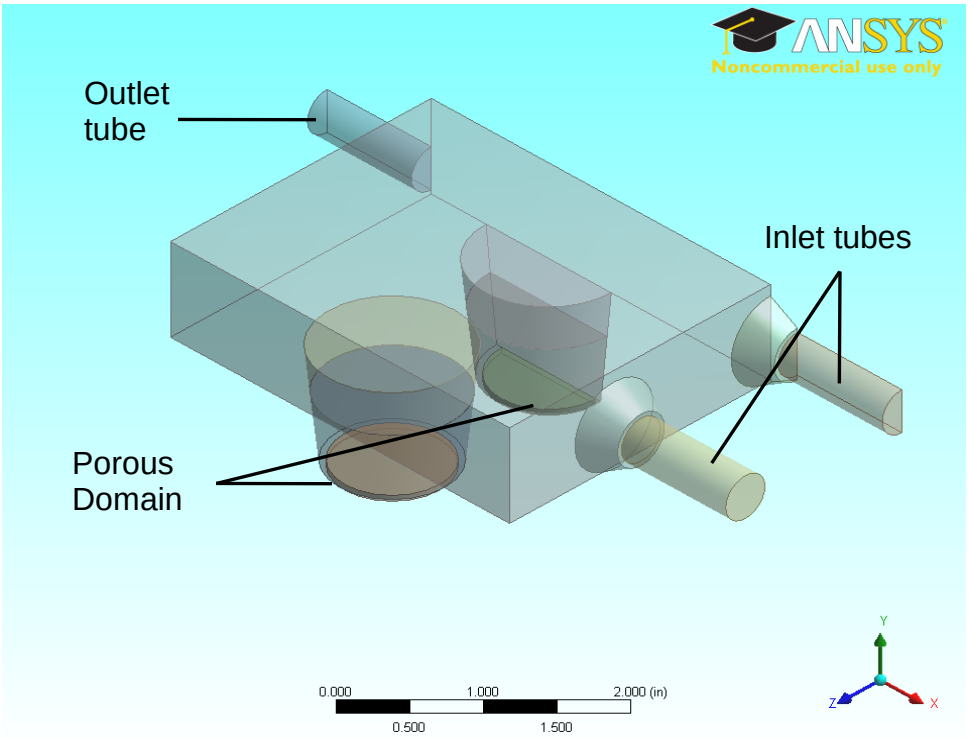

FIGURE 2.2: Isometric view of the half symmetry Ansys model of the flow region in the test device.

i. [*] The Pro-E design of the test device was done with the help of James Cassell from UNC, Charlotte.

2.3.2 Geometry and Mesh

The model's first requirement was to simulate the regions through which the nutrient media would flow. This was achieved using the Ansys Workbench 11.0 as shown in Fig 2.2. (Note: Although Fig 2.1 and Fig 2.2 represent the same geometry, Fig 2.1 is a Pro E design of the actual test device, whereas Fig 2.2 is a half symmetry Ansys 11 design of the flow region within the test setup). The Ansys design (Fig 2.2) neglects the trough region of the test setup, since it does not influence O_2 transport within the cell space. The "porous domain", indicated in Fig 2.2, represents the 3D cell space through which media permeation (and thus O_2 transport) takes place. Meshing of the generated volume was done using Ansys CFX mesher 11.0. Prismatic meshes were used in the wall boundary layer region to account for boundary layer effects whereas fine tetrahedral meshes (mesh size < 0.2 cm) were used everywhere else.

2.3.3 Governing Equations

For the simulation process it was necessary to provide the governing equations and boundary conditions that would accurately define media flow dynamics and O_2 transport mechanism within each 3D cell space.

2.3.3.1 Law of conservation of mass

First and foremost, the flow of the working fluids in the bioreactor system must satisfy the law of conservation of mass [91].

$$\frac{\partial(\gamma\rho Y_i)}{\partial t} + \nabla.(\gamma\rho\vec{V}Y_i) = \nabla.(\rho D_{i,m}\nabla Y_i) + \gamma S_m \qquad (2.1)$$

where ρ is the density of the working fluid, Y_i is the mass fraction of the working fluid, $(\nabla\cdot)$ is the divergence operator, $\vec{v}$ is velocity vector, γ is the porosity of the porous

material, $D_{i,m}$ is the diffusivity of i^{th} substance in medium *m*, and S_m is the mass source (positive if mass is generated, negative if mass is consumed).

2.3.3.2 Law of conservation of momentum

For problems involving fluid dynamics, the flow dynamics of the fluid is governed by the law of conversation of momentum. In the current model, since we consider a multi-phase fluid – a mixture of media and oxygen, law of conversion of momentum has to be satisfied for both the phases. The momentum conversation equation used for the model is as follows

$$\frac{\partial(\gamma\rho_m \vec{V_m})}{\partial t} + \nabla.(\gamma\rho_m \vec{V_m}\vec{V_m}) = -\gamma\nabla p + \gamma\nabla.\mu_m(\nabla\vec{V_m} + \vec{V_m}^T) - \frac{2}{3}\nabla.\vec{V_m} I + \gamma\rho_m \vec{g} + A + B \tag{2.2}$$

where

$$A = \nabla.(\sum v_k p_k \vec{V_{dr,k}}\vec{V_{dr,k}}) \tag{2.3}$$

$$B = -\left\{\frac{\mu_m}{\alpha} + \frac{C}{2}\rho\left|\vec{V_m}\right|\right\}\vec{V_m} \tag{2.4}$$

$$\vec{V_{dr,k}} = \vec{V_k} - \vec{V_m} \tag{2.5}$$

In Eq. 2.2, p is the partial pressure, μ is the viscosity of the phase *m*, and *g* is the gravitational effect. There are two additional factors included to the momentum conversation equation – terms *A* and *B*. The term *A* accounts for the momentum conversation of the diffusing species (diffusion of O_2 in the media) and given by the Eq. 2.3. In Eq. 2.3, $\vec{V_{dr,k}}$ represents the relative velocity of the diffusing species (O_2) in the working fluid (media). The term *B* accounts for the resistance offered by the porous cell space domain and is given in Eq. 2.4, where *C* is the coefficient of resistance. The term B

comes into consideration only for the region in which the fluid flow takes place in the porous domain.

2.3.3.3 Mass transport equation

To predict the diffusion of O_2 in the test system, the mass transport equation (Eq. 2.6) is considered.

$$\frac{\partial(\gamma\rho_m\phi)}{\partial t} + \nabla.(\gamma\rho_m \vec{V}_m \phi) = \nabla.(\gamma_m \Gamma \nabla\phi) + \gamma S_\phi \tag{2.6}$$

where ϕ is the concentration of the diffusing species in medium m and S is the mass source – representing the consumption of O_2 by the cells in the cell space.

Thus with the above mentioned governing equations as its foundation, the model for predicting the O_2 transport from the supply media to the cells distributed throughout the cell space was obtained.

2.3.4 Heat Transport Model

Directly verifying the accuracy of the model's mass transport predictions requires mass transport through the small volumes of the 3D cell space of the test setup to be experimentally measured. Since this is difficult to accomplish without evasively altering the transport kinetics, an indirect method was devised for evaluating the model's accuracy. An analogous heat conduction problem was setup experimental, the details of which are discussed in Section 2.4.2 and a corresponding computational model was generated. The governing equation consider for the heat transport model is as follows.

$$\frac{\partial(\gamma\rho_f E_f + (1+\gamma)\rho_s E_s)}{\partial t} + \nabla.(\rho_f \vec{V} E_f) = \nabla.(k_{eff} \nabla T) + S_f \tag{2.7}$$

$$k_{eff} = \gamma k_f + (1-\gamma) k_s \tag{2.8}$$

where E is the heat energy, k_{eff} is the effective heat diffusivity between the fluid phase f (water) and solid phase s (walls and porous domain), and T is the temperature.

The analogies between the principles and governing equations of heat and mass transport enabled the transient heat conduction problem (governed by Eq. 2.7) to be used as an appropriate benchmark experiment for O_2 transport through the thickness of the 3D culture space of this study. To clarify this point, considering the similarities between Eq. 2.6 and Eq. 2.7, it is evident that the forms of the two equations are equivalent. Hence to evaluate the accuracy of the CFD model's predictions, transient heat conduction through the volume of the 3D cell space was measured using water as the working fluid (instead of media), and using Teflon for the porous domain.

2.3.5 Mass Transport Model

Once the transport model's predictions were validated with the help of the benchmarking experiments and the heat transport model, the simulations of O_2 transport through the 3D cell spaces of the test device commenced. For these simulations the working fluid (O_2 dissolved media) was modeled as a two phase mixture, where the media was taken as the primary phase, while the dissolved O_2 was modeled as the secondary phase. The 3D cell space of the test system was considered to be collagen sponge and was modeled as the porous domain. The cells were assumed to be uniformly distributed within the collagen sponge and were modeled as a constant negative source of mass for the secondary phase, i.e., constant consumers of O_2 within the porous domain. Consequently each 3D cell space had a constant O_2 consumption rate, S_{oxy}. As such, the O_2 consumption rate S_{oxy} of the cell space would increase if either the consumption rate per cell (R_{oxy}) increases or the number of cells (N) it contains increases. This resulted in the following relationship for S_{oxy},

$$S_{oxy} = \frac{R_{oxy} * N * Vol_{ECM}}{\gamma * Vol_{cell}} \tag{2.9}$$

In addition to the S_{oxy} value, the model of this study requires other key inputs such as the inlet flow rate, the initial level of O_2 in the nutrient media, the material properties of the ECM, working fluid, etc. By varying and/or adjusting these inputs, different scenarios can be simulated to determine the corresponding O_2 distribution pattern within a given 3D cell space. In the current study, the computational model was used to evaluate the effects of six inlet flow rate variations ranging from 0-10 ms^{-1}, six O_2 capacity levels of the media ranging from 5-10 mg/l of O_2; and ten variations of S_{oxy} for the 3D cell space.

2.4 Material and Methods

To help ensure the accuracy of the computational model, several complementary experiments were conducted to evaluate key material properties for use as input to the computational model, and to calibrate the model's predictions. The details of each will now be described.

2.4.1 Test Device and the Circulation System

FIGURE 2.3: The experimental test device fabricated from a steel block based used to perform the benchmarking experiments[†].

ii. [†] The test device was fabricated by James Cassell from UNC, Charlotte.

Recall that Fig. 2.1 illustrated the experimental test setup designed for this study. It was designed in Pro-E, based on the criterion discussed in the Computational Methods section, then fabricated. Fig 2.3 shows the experimental test device fabricated from a steel block. The device consists of three inlet ports through which pump-driven flow media is able to enter the main cubical region, after travelling from a media reservoir source. The bottom face of the main section has three holes, designed for the placement of transwells culture dishes (Falcon Becton Dickinson labware, Model: 353091) for supporting individual culture samples. Since the base of each transwell consists of a semi-permeable membrane of 3 micrometers pore size, depending on the contents and permeative properties of the cell space, a fraction of the media would permeate through the cell space - to the bottom trough. The rest of the media would exit directly through the top outlet.

An Ismate peristaltic pump (BVP, Model: CP78002-01) pumps media in to the main section of the device via three inlet ports (refer to Fig. 2.4). The flow settings of the pump, as well as the permeation characteristics of the cell space direct the level to which the nutrient media is able to permeate through the thickness of each individual 3D cell space sample. The outputs from the two outlets of the device i.e., the top outlet and outlet connected to the trough are then collected, re-oxygenated in the gas chamber. The re-oxygenated media is then recombined in the media reservoir and recirculated – as illustrated in Fig. 2.4.

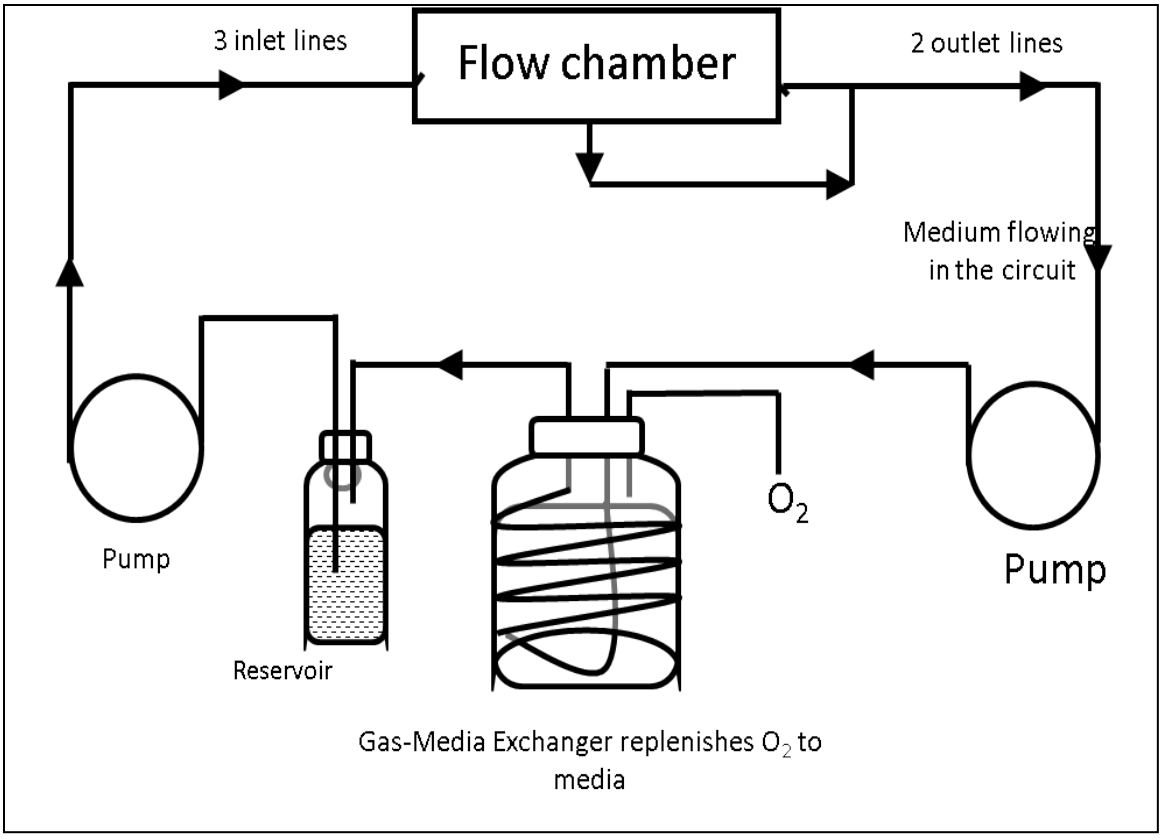

FIGURE 2.4: Schematics of the circulation system of the test setup circuit consisting of the test device (flow chamber) and other components which enables maintaining cell culture.

2.4.2 Benchmarking Experiments

In order to verify the accuracy of the CFD model's transport predictions, the models prediction for an analogous heat conduction problem was compared to experimental results. For these benchmarking experiments, and their corresponding CFD simulations, water was used as working fluid, and the 3D sample space in the transwell portion of the test device was packed with Teflon powder. The experiment was designed to measure the thermal transport through the 3D sample space where a higher temperature working fluid (i.e., H_2O) was supplied to the setup.

More specifically, in this benchmarking experiment 90^oC source water from the reservoir was pumped through the inlet ports at a velocity of 6.25 ms^{-1}, where the initial

temperature of the test device and the Teflon sample space were both 22^{o}C. The hot water then flowed over and through the 3D Teflon sample space, resulting in thermal variation across the sample space. The water was then collected and directed back to the reservoir for reheating to 90^{o}C and re-circulation. Also to minimize the effects of radial thermal variations along a given horizontal plane of the 3D sample space, the outside of each transwell was insulated using heat insulation tape [Model# 5541, Summit Equipments]. This resulted in an adiabatic boundary condition around the radial circumference of the sample - effectively reducing it to a 1D transient heat conduction problem.

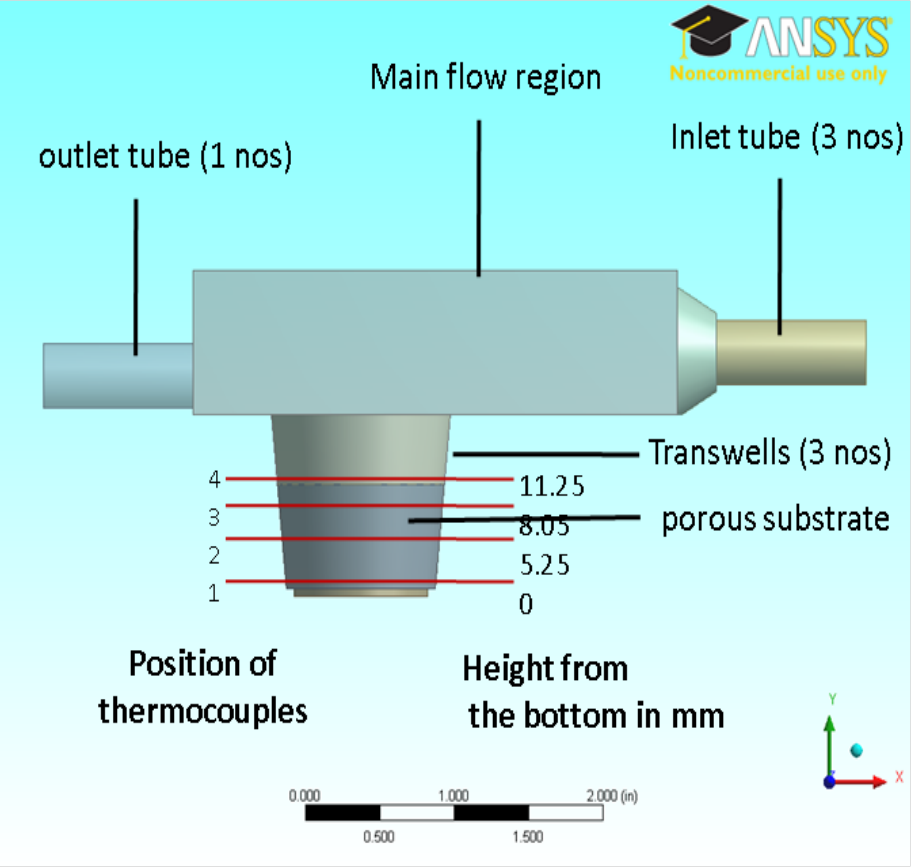

FIGURE 2.5: A representation of the test device depicting the positioning of the thermocouples in the porous subrate (packed Teflon) during the benchmarking experiments.

During the process, the transient change in the temperature at four locations (0, 5.25, 8.05, and 11.25 mm from the base – Indicated in Fig 2.5) along the vertical axis of each Teflon sample was recorded over time using T-type thermocouples connected to a multimeter (Keithley 2000. Model: 0703538). A minimum of three independent experiments were completed, and the averaged results were then compared to the CFD model's predictions of the transient thermal history of the Teflon sample space.

In a complementary experiment, the net volume of permeated fluid through the sample and into the bottom outlet of the trough of the test setup was collected in a graduate cylinder at specific time points, to quantify the rate of volumetric outflow through each individual sample space. These measurements were also available for comparison with the model's predictions.

2.4.3 Evaluation of Material Properties

A computational model is only as accurate as its inputs. Hence the accuracy of the CFD model of this study required measured values of the density of the working fluids and porous materials of the sample space; the viscosity of the working fluids, and the porosities and permeabilities of the ECM and Teflon, since these were not readily available in the literature for the conditions of this investigation. How each was determined is now briefly described.

2.4.3.1 Working fluids and its properties

The working fluid of the benchmarking experiments was de-ionized water, while the working fluid of the oxygen transport predictions was liquid minimum essential media (MEM). Liquid MEM was prepared by dissolving 12.5g of MEM dry powder (Mediatech Inc, Manassas, VA), 2.75 g of sodium bicarbonate in 1L of distilled water

and adjusting the pH value to 7.4. The densities of the working fluids at room temperature 22^{o}C and human body temperature 37^{o}C were measured by weighing 1 ml of the target fluid using an analytical balance (Mettler Toledo Excellence Plus XP Analytical Balance, Model XP205DR, Columbus, OH). The viscosity of each working fluid was also measured at 22^{o}C and 37^{o}C, using the Cannon-Fenske Routine Viscometer (Standard test ASTM DD 45, IP 71 and ISO 3104, State College, PA). In all cases, the fluid temperate was carefully monitored and regulated using a thermometer (Sper Scientific, Range: 0 - 260^{o}C, Accuracy 0.1^{o}C) and a hotplate (VWR, Model: VMS C7 S1, Radnor, PA), respectively.

2.4.3.2 Teflon column preparation and their properties

The Teflon PTFE powder (Dupont) was used as the porous material in the cell space region for the benchmarking heat transport experiments. The cell space region for these experiments was prepared by uniformly packing 2g of the Teflon PTFE powder in the transwells. Then the density of the Teflon was calculated by measuring the volume occupied by the Teflon in the transwell.

The porosity and permeability of the Teflon packing were also important as they directly affect the permeation success of the working fluid through the cell space. For the Teflon columns, the packing firmness directly influences the porosity. As such the porosity of each Teflon column was calculated as the ratio of the difference between the measured volume (i.e., the physical volume occupied by the uniformly packed Teflon in the transwell insert) and the calculated volume, against the measured volume. The calculated volume of the Teflon column of each transwell was calculated by multiplying the theoretical mass density of the Teflon PTFE powder by its known mass of 2g.

2.4.3.3 Collagen sponge preparation and their properties

For the oxygen transport model, Gelfoam absorbable gelatin collagen sponge (Pharmacia and Upjohn) was considered for the 3D cell space. Determining the density of the ECM sponge required a slightly more elaborate approach due to its changes in hydrated cell culture environments. Specifically, the dry ECM sponge was initially cut into 35 mm diameter disks of 1 cm thickness each, and measured on an analytical balance to determine its dry weight. Next to condition the sponges for tissue culture, each sponge was placed in a Redi-Pak straight wall glass jar (VWR, Radnor, PA) and soaked in 25ml of antibiotic/antimycotic solution (sterile de-ionized water containing 400 Unit penicillin G, 400 g streptomycin and 1g amphotericin B per ml). The glass jar was then placed in the Fisher Isotemp 280A vacuum oven (ThermoFisher Scientific) with a relative pressure of -28 inHg for 12 hours to degas the sponge completely. The prepared sponges were then transferred to a standard 6-well plate and soaked for one hour in 5ml of 1x Hanks Buffered Salt Solution (HBSS) to sufficiently dilute the antibiotic/antimycotic solution. Next the HBSS was aspirated and 5 ml of liquid MEM was added to each sponge, followed by 1 hour of incubation. The prepared sponge's wet weight and dimensions were then measured using an analytical balance and caliper, respectively. The mass densities were then calculated as the measured mass per measured volume.

The porosity of each prepared ECM sponge was measured using the water displacement method. For this method a wet sponge of known mass (m_1) was dropped into a known mass of water (m_2), then after equilibration the combined mass (m_3) is measured. Thus the ratio difference between the total mass (m_1+m_2) and the combined mass (m_3) to the mass of the sponge (m_1) yields the porosity of the prepared ECM sponge.

The permeability of the Teflon column and the ECM sponge samples were measured using the Constant Head Permeability test. In this process, a constant water head, h, is maintained over a known thickness L and the discharge of water, Q, in time, t was measured. This allowed the hydraulic permeability, k, to be calculated as: $k = \frac{QL}{\mathrm{Aht}}$.

2.5 Results

2.5.1 Validation of the Transport Model

The aim of this study was to develop CFD model able to predict O_2 transport and distribution through 3D cell spaces. To confirm the model's accuracy, its ability to successfully predict the analogous thermal transport through a specified sample volume was first evaluated (using parameters shown in Table 2.1) and compared to the transient heat conduction experimental results.

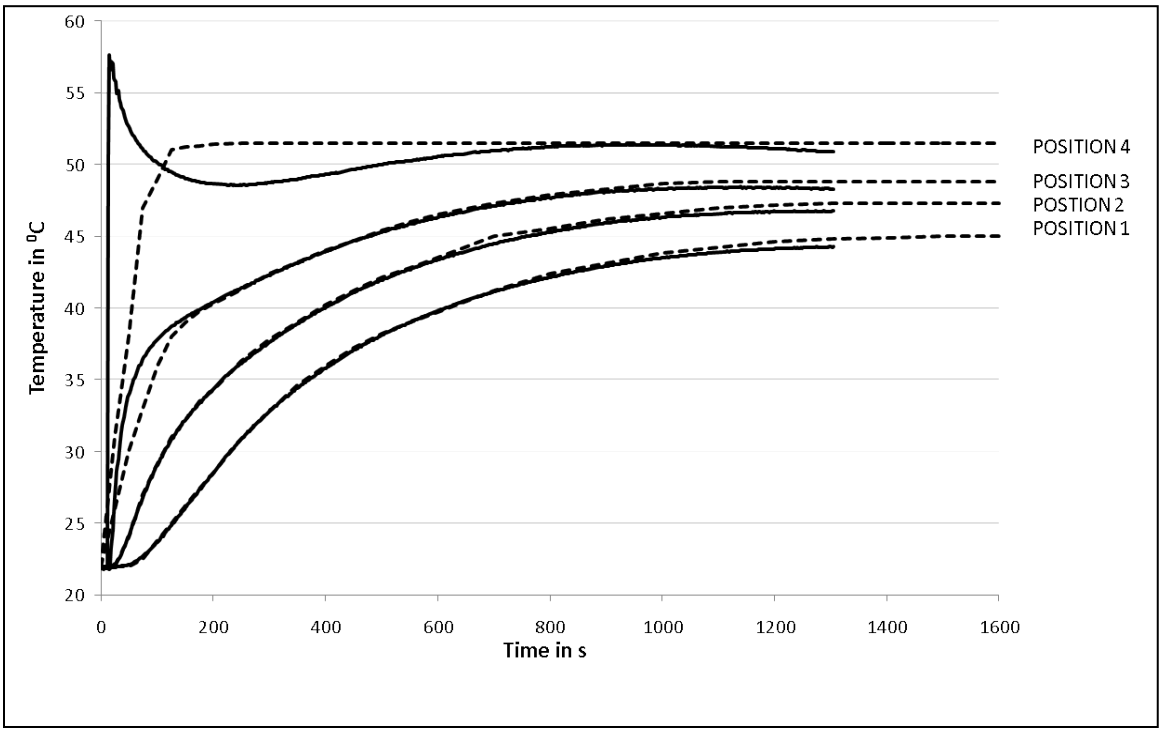

FIGURE 2.6: Time vs temperature comparison obtained during the benchmarking process via the transient heat conduction problem. The solid lines indicate data obtained from experiments and the dotted lines denote the results obtained from the computational model.

As shown in Fig 2.6, the experimentally measured (solid lines) and computationally predicted (dotted lines) temperatures for four positions (Refer Fig 2.5) throughout the columnar sample, with respect to time, are plotted. From the plot it is clear that there is a close correlation between the two methods, with few exceptions. One notable exception is visible in the initial time periods, for thermocouple positions 3 and 4. These two thermocouples are positioned closest to the convective bulk fluid flow of the sample surface. It is thus probable that these variations are attributable to unavoidable experimental fluctuations incurred as the flow's streamlines adjust during the early timepoints of the experiment. Specifically, the discrepancy visible for thermocouple 4 is surmised to be due to the thickness and position of that sensor, such that instead of being fully embedded in the Teflon column, it is instead partially exposed to the hot water inflow of the test setup. In contrast, since the simulated position 4 is modeled as fully embedded in the Teflon substrate, it is unsurprising that its temperature rise is predicted to be more gradual. Excluding that, the computational model otherwise matches the experimental results with 98% accuracy.

In addition to the temperature measurements of these benchmarking experiments, the volumetric flow rates of the water through the bottom outlet (i.e., the water collected in the trough following permeation through the pores of the Teflon test sample) -- were also measured. Its value was 0.115 ± .002 ml/min from the experiments, and 0.11596 ml/min from the model's prediction. These two sets of benchmarking results thus confirm the accuracy of using the CFD model for transport predictions, within reasonable tolerances.

2.5.2 Oxygen Transport Model

Once the model was validated, simulations for O_2 transport were generated for specific scenarios of 3D liver systems. For each, liquid MEM media served as the flowing fluid, while collagen sponges embedded with primary rat hepatocytes comprised the 3D cell space. The number of cells was taken to be 4 million. Thus the value of the O_2 consumption rate for the 3D cell space S_{oxy} was calculated to be approximately 1e-11 kg/m^3 (Refer Table 2.1 for the values used). The initial level of oxygen in the media was taken to be 6.85 mg/l and the velocity of media at the inlet was 6.25 ms^{-1}. With these sets of conditions and properties from Table 2.1 as inputs to the model, the O_2 transport model was generated.

TABLE.2.1 Values of material properties and key parameters used for the simulations of the CFD model.

Symbol	Description	Material	Value	Unit	Reference
$\boldsymbol{\rho}$	Density	Water	1000	kg/m^3	measured
		Media	1009.67	kg/m^3	measured
		Collagen	1120	kg/m^3	[154]
		PTFE	2200	kg/m^3	MFG
		Oxygen	11	kg/m^3	[155]
$\boldsymbol{\mu}$	Dynamic viscosity	Water (22^{o}C)	0.9594	g/m.s	measured
		Water (37^{o}C)	0.6627	g/m.s	measured
		Media (22^{o}C)	0.70232	g/m.s	measured
$\boldsymbol{m}$	Molar mass	Water	18	g/mol	[155]
		Media	52.461	g/mol	calculated
		Oxygen	32	g/mol	[155]
$\dot{m}$	Mass flow rate	Outer inlet	0.201934	g/s	measured
		Middle inlet	.100967	g/s	measured
$\boldsymbol{C_p}$	Specific heat capacity	Water	4.18	J/kg K	[155]
		PTFE	1040	J/kg K	MFG

(Continued)

(Continued)

γ	Porosity	PTFE	0.45	-	measured
		Collagen sponge	0.66	-	measured
κ	Darcy's permeability	PTFE	1.53E-9	mm^2	measured
		Collagen Sponge	2.88E-8	mm^2	measured
D	Diffusivity in media	Oxygen	2.415E-5	cm^2/s	[156]
c	Coefficient of resistance	PTFE	2420238	-	calculated
		Collagen sponge	243900	-	calculated
R_{oxy}	Oxygen consumption per cell	Hepatocytes	6.4x10-12	mg/s	[157]
N	Total number of cells in the cell space	Hepatocytes	$4x10^6$	-	
Vol	Volume	Cell space	$5x10^{-6}$	m^3	measured
S_{oxy}	Oxygen consumption rate per unit vol. of cell space	Hepatocytes	$5.1x10^{-6}$	kg/m^3s	calculated

2.5.2.1 Visualization and analysis of the O_2 distribution

Fig 2.7 and Fig 2.8 illustrates the simulated contour plots of O_2 distributions for a 25mm diameter and 12mm length cylindrical collagen sponge seeded with hepatocytes. In the contour plots the O_2 distribution results have been expressed in terms of the volume fraction of O_2 in the media, since this is a convenient equivalent to partial pressure. In Fig. 2.7 and Fig. 2.8, the red regions represent regions of the 3D cell space that have the maximum O_2 availability value of 6.85 mg/l (equal to the O_2 content in the input media), while blue regions have negligible O_2 presence (hypoxic condition). It is important to mention that only half of the test setup is shown in the figures because of half symmetry exists for this geometry of this test setup, such that transport within the omitted regions are exact mirrors of the displayed regions.

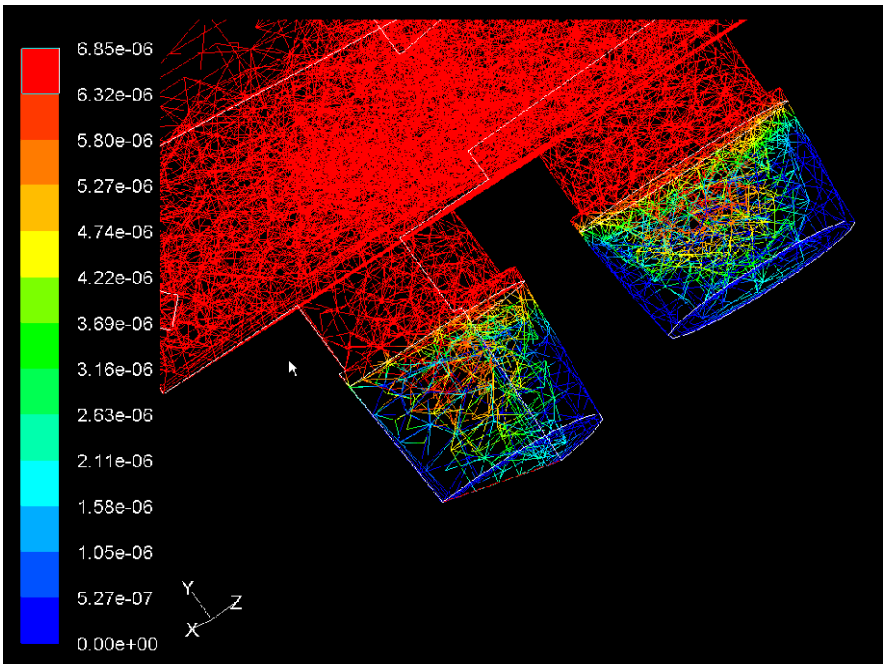

FIGURE 2.7: 3-D translucent image of the contour plot showing the O_2 distribution obtained in the test device with an inlet mass flow rate of 60 ml/min and dissolved O_2 level in media of 6.85 mg/l. The right hand side shows the bottom view perspective of the contours at the boundaries.

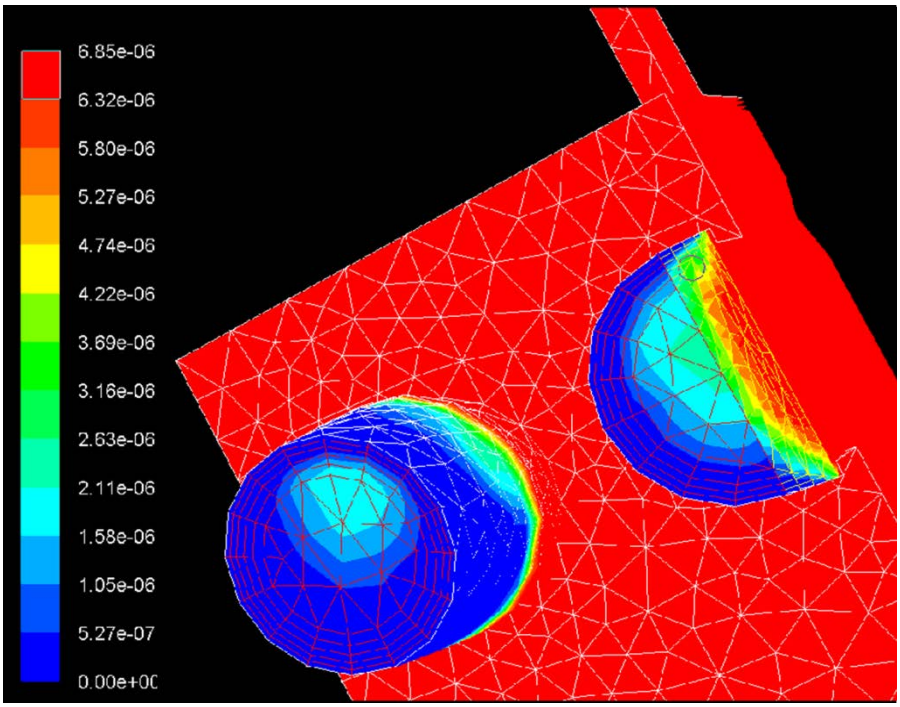

FIGURE 2.8: Contour plots showing the O_2 distribution along the walls and the bottom plane of the cell space obtained in the test device with an inlet mass flow rate of 60 ml/min and dissolved O_2 level in media of 6.85 mg/l.

Fig 2.7 represents 3D - translucent view of the O_2 distribution plot displaying the various gradients established within the cell space. It can be seen that an O_2 gradient was observed along the height of the cell space. Also cells located near the top of the cell space experience the highest levels of O_2 exposure, which then decreases with depth into the cell space. This is logical since O_2 transport from the media source is subsequently hindered by resistances due to the ECM's properties and continuous O_2 consumption by the cells. Consequently, for the geometry and flow conditions shown in Fig. 2.7, no O_2 was available for use by the cells near the bottom of the cell space. It is thus expected that cells in those regions are likely to experience hypoxic conditions, which has the potential to negatively affect performance and possibly lead to cell death [20].

In addition to the O_2 gradient along the axial direction, radial O_2 gradients within the 3D cell space were also observed. This is partially visible in Fig. 2.7, where for any horizontal plane of the 3D cell space, the O_2 availability was considerably higher near the center of the plane and lowest adjacent to the walls. This suggests that the equivalent to an O_2 boundary layer may form adjacent to the walls of the test device. The thickness of this O_2 boundary layer appears to increase as one advance along the depth of the 3D cell space. This can be much more clearly identified from the locations of the dominant blue regions in Fig 2.8 -- which shows the O_2 levels available to cells positioned along the sides of the cells space (along the walls) as well as the bottom most planes of the cell space. It can be clearly seen that the regions located near the walls have access to negligible O_2.

Another observation arising from Fig 2.8 is that the O_2 distribution in the middle cell space is higher compared to the outer cell spaces, suggesting that for the conditions

evaluated, the cells nearer to the axis of the cell space are likely to benefit with higher cell viability and function.

2.5.2.2 Effect of the media flow pattern

The patterns of O_2 distribution discussed in Section 2.5.2.1 were found to be consistent for several simulation scenarios. Hence, in order to understand the factors that influence O_2 transport and its distribution pattern in the 3D cell spaces, the flow patterns of the media were analyzed. Fig 2.9 and Fig 2.10 show the flow pattern of the media in the test device for the same conditions as discussed for the O_2 distribution. Fig 2.9 clearly illustrates ordered streamlines of media flow through the bulk flow region of the device. Yet in comparison, permeation flow through the 3D cell space appears to be negligible. However, when a detail of the permeation flow through the 3D cell space is visualized (Refer Fig 2.10), it becomes clear that a fraction of the nutrient media does percolate through the cell space, but with a velocity that is two orders of magnitude less than that in the main bulk flow region. The results from Fig. 2.9 and Fig 2.10 also reveal the following observations: In the bulk flow region of the test device, it is the middle cell test space that experiences a notable level of media flow uniformity, compared to the outer ones (see Fig. 2.10). The significance of this is that flow uniformity is expected to induce more favorable O_2 transport through the associated cell test space. This can be confirmed by the fact that in the O_2 distribution contour plots (Fig 2.7 and 2.8) the central cell space has comparatively lesser hypoxic region compared to the outer cell space.

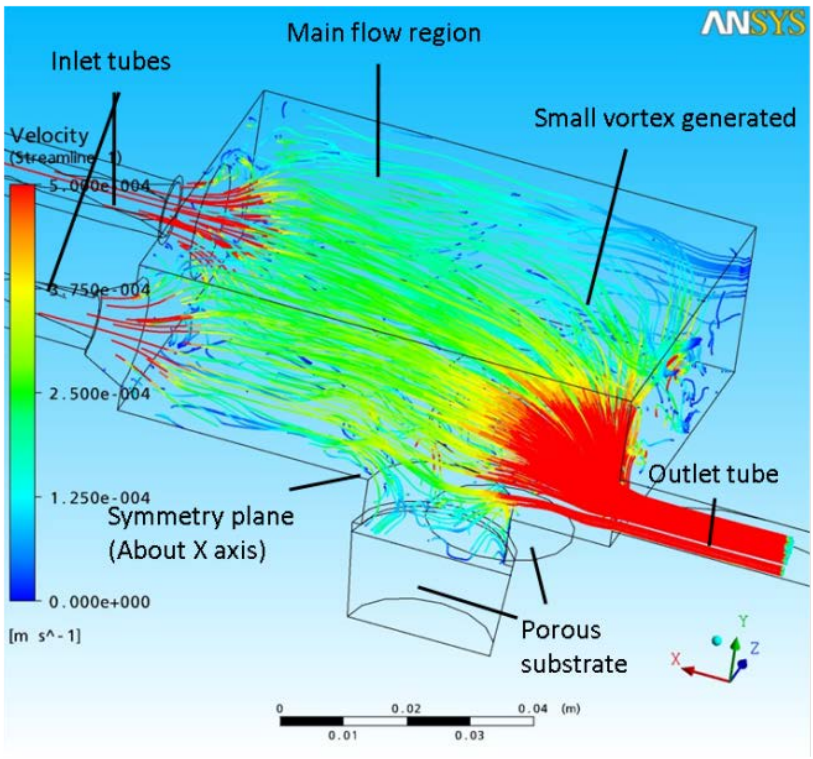

FIGURE 2.9: Velocity distribution contour of the flow in the flow region of the test device.

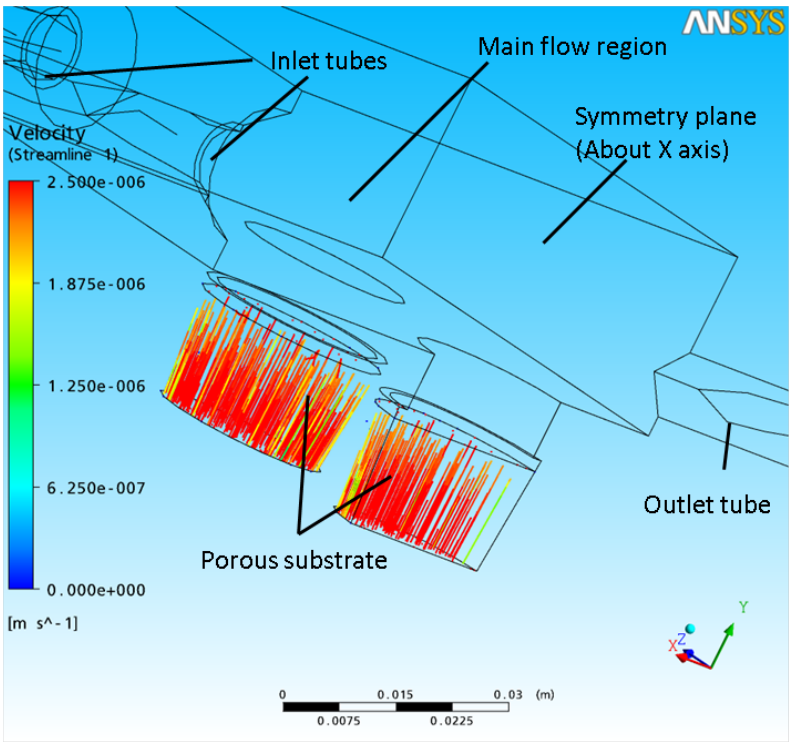

FIGURE 2.10: Velocity distribution contour of the flow in the porous substrate region contained within the cell space of the test device.

Also Fig 2.9 shows a relatively high media permeation rate visible along the central axis of the cell space, as compared to near the walls. This variation correlates directly to the patterns observed in the O_2 distribution plots (Fig 2.7 and Fig 2.8) wherein O_2 availability to the cells was high closer to the central axis and significantly low near the walls. Therefore, it is confirmed that the media flow pattern has a direct influence on the O_2 distribution patterns within the cell space.

2.5.2.3 Effect of the O_2 consumption rate

Using the mass transport model, several simulations were generated to analyze the effect of varying S_{oxy}, i.e., the O_2 consumption rate for the entire cell space on the resultant O_2 transport. Recall from Eq. 2.9, that the value of S_{oxy} can be altered by changing several parameters, including cell number and cell type. Therefore by applying the CFD model to such an analysis, it would help identify the optimal S_{oxy} value (thereby optimal cell numbers) that can be maintained for a given cell space design. In generating such simulations, it was assumed that the cells in the cell space can maintain high viability and performance for O_2 volume fractions ranging from 3e-06 to 9e-06 (equivalent to pO_2 of 100 – 300 torr), known as the normoxic range. This assumption hold true for primary rat hepatocytes [92] and hence was considered for presenting the results in the following sections.

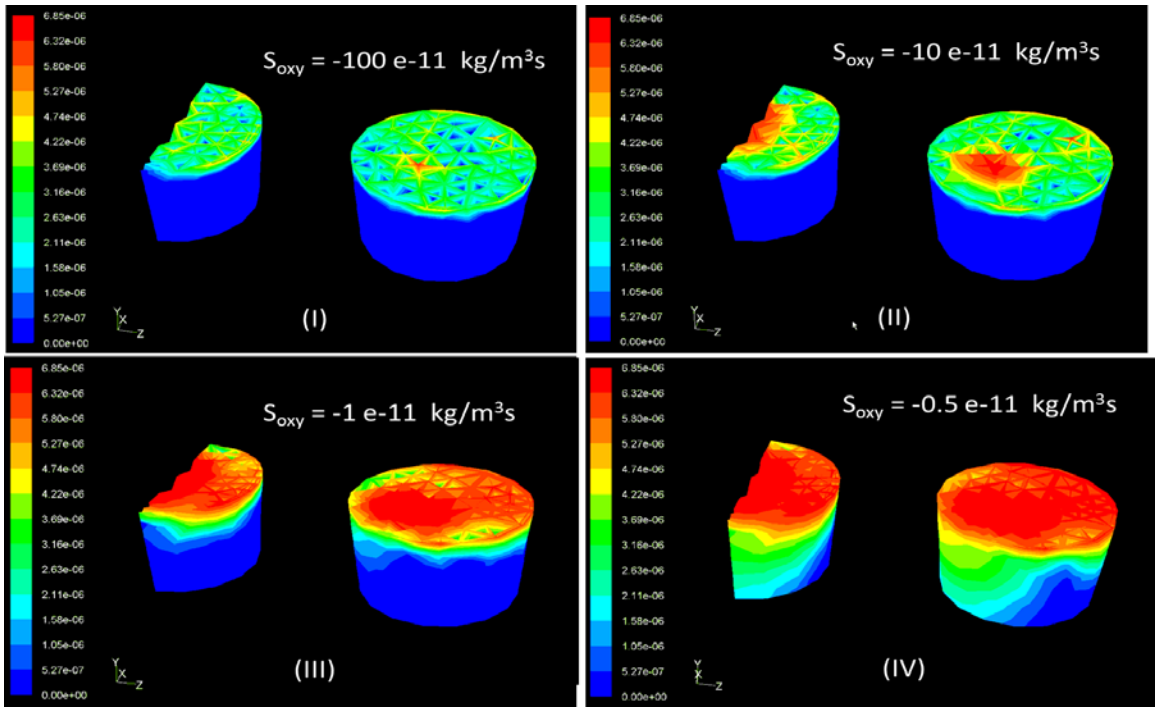

FIGURE 2.11: Oxygen distribution contour plots of the cell spaces for four different values for the O_2 consumption rate (S_{oxy}).

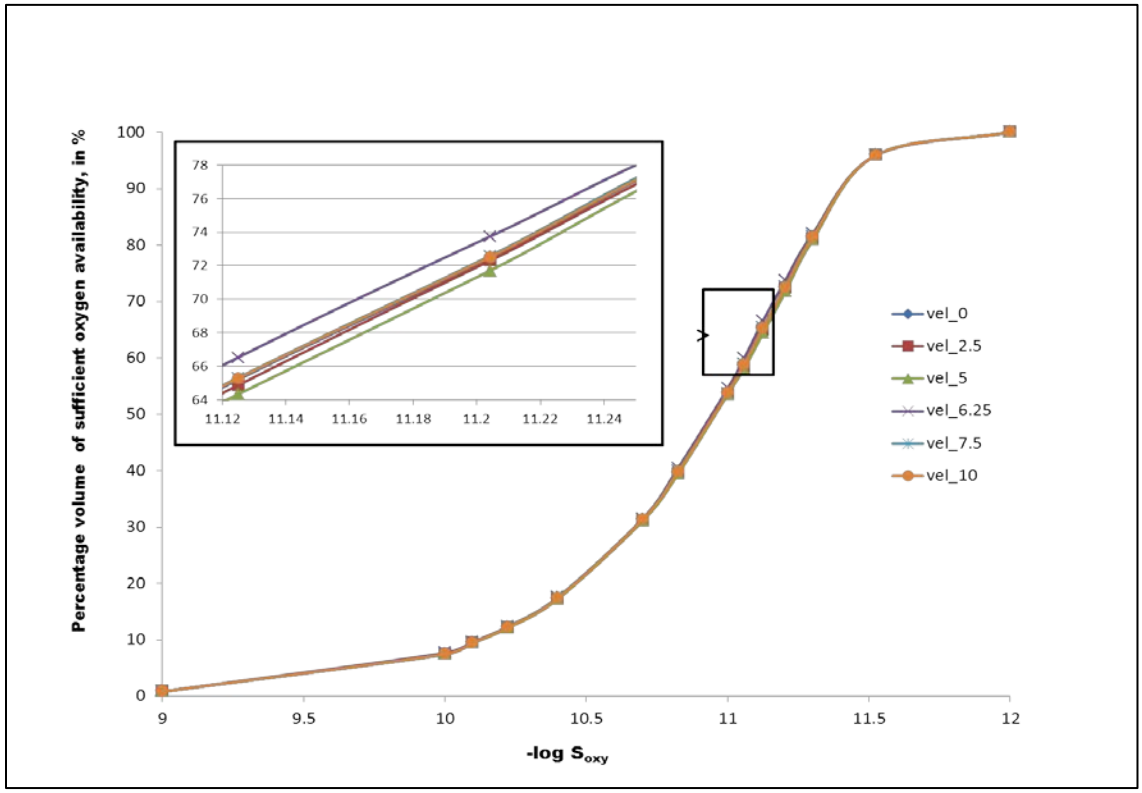

FIGURE 2.12: Graph showing the volumetric percentage of normoxic regions (i.e., O_2 volume fraction in media > 3 e-6) in the cell space, versus the log Soxy of the cell space -- for different inlet media velocities [m/s], more clearly visible in the detail view.

Some of the results from the simulations for the analysis of the effect of varying O_2 consumption rate within the cell space are represented in Fig 2.11. It was found that for a model with primary rat hepatocytes cultured in collagen sponge matrix, the most significant effects are visible for S_{oxy} values between 1e-12 to 1e-09 kg/m^{3}s. For (S_{oxy} < 1e-12 kg/m^{3}s), the O_2 consumption is low enough for normoxia to prevail throughout the entire cell space. On the contrary, for S_{oxy} values greater than 1e-9 kg/m^{3}s, the O_2 consumed by the cells is so high that it impedes O_2 transport from occurring within the cell space volume. Fig 2.11 depicts the O_2 distribution contour within the 3D cell space for four S_{oxy} values. In Fig 2.11(I) it can be clearly seen that for a high S_{oxy} of 1e-9 kg/m^{3}s, very little O_2 (blue colored regions) is available for the majority of the cell space. Also as the S_{oxy} value is reduced (Fig 2.11-II, III and IV), there is increased O_2 availability for the cell space volume. Compressing the data from the contour plot into graphical form yields the curve shown in Fig 2.12 - where the volumetric percentage of normoxic region within the cell space is plotted against the logarithm of "S_{oxy}" values within the same range (i.e., 1e-12 to 1e-09 kg/m^{3}s).

2.5.2.4 Effect of the varying the inlet media flow velocity

As already discussed in Section 2.5.2.2, the media flow profile has a direct effect on the O_2 distribution pattern. A factor that can affect the flow profile is the inlet media velocity. So the CFD model is used to elucidate the effect of varying the inlet media flow-velocity on the resultant O_2 distribution through the 3D cellular space, with the assumption that the flow remains laminar. This effect is also revealed by Fig 2.12. As can be seen, varying the inlet media flow velocity has very little effect - a maximum

difference of only 2% (refer to the expanded view insert of Fig 2.12) in the cell space volume fraction experiencing normoxic conditionss (i.e. O_2 volume fraction > 3e-06).

2.5.2.5 Effect of the O_2 content in the supply media

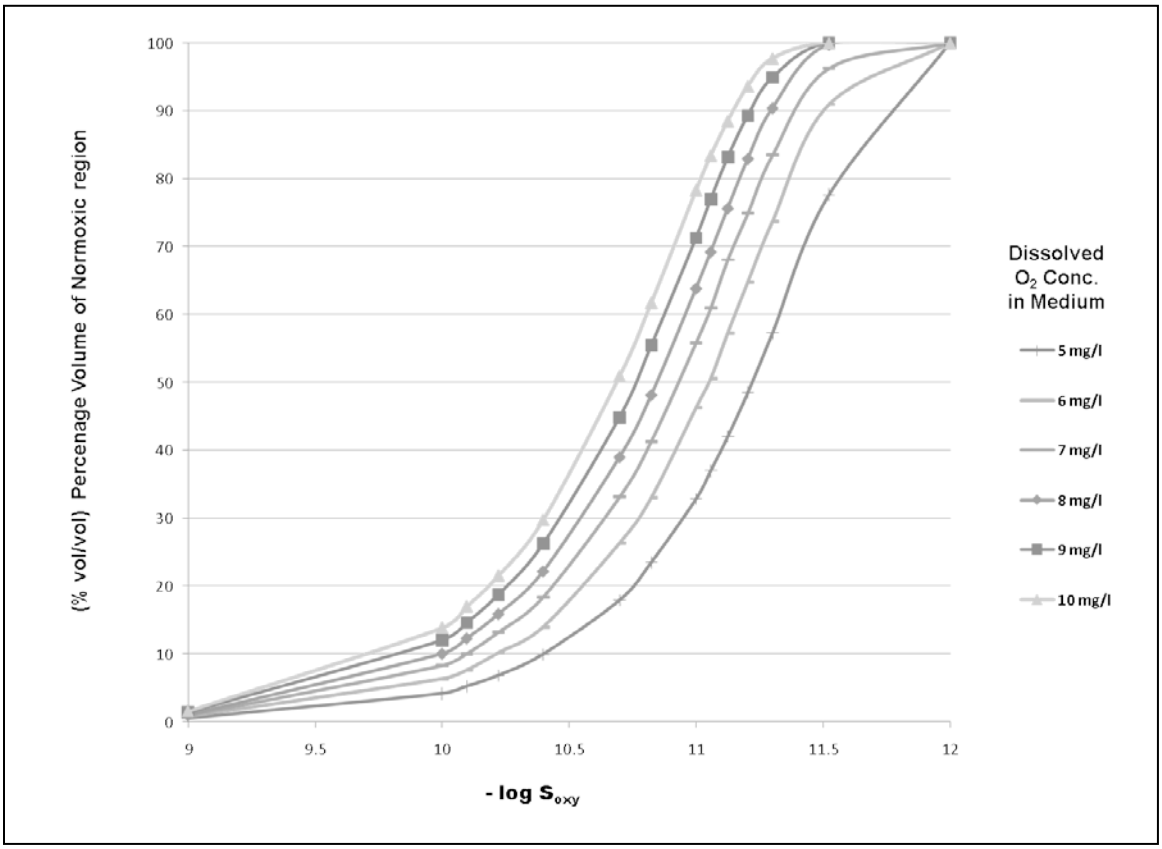

FIGURE 2.13: Graph showing the volumetric percentage of normoxic regions (i.e., O_2 volume fraction in media > 3 e-6) in the cell space versus a log $_{Soxy}$ of the cell space for different values of dissolved O_2 levels in the supply media.

Another critical factor that affects the performance of 3D tissue constructs is the level of dissolved O_2 in the supply media (i.e., the inlet media). The effect of altering the quantity of dissolved O_2 levels in the supply media is elucidated by the results of Fig 2.13. It also depicts the volumetric percentage of normoxic region of the cell space versus the logarithmic O_2 consumption rate (S_{oxy}) in the cell space, with the family of curves representing the effects of varying the level of dissolved O_2 in the supply media. As expected, increasing the level of dissolved O_2 in the media supply enhances the O_2

distribution within the cell space. In the Fig 2.13, the family of curves is limited to a maximum dissolved O_2 content in the media to 10 mg/l, since further increase might lead to hyperoxic conditions – the effects of which are not considered in the current analysis.

2.5.2.6 Effect of the thickness of the cell space

In considering the role of volumetric dimensions in directing O_2 transport within 3D tissue constructs, it has been established that the thickness of the cell space volume is a major factor that affects functionality [93]. This is particularly true for cases similar to that of the current study, in which O_2 is convectively delivered via bulk media flow to the surface of the 3D construct. For such systems, the CFD model can also be used to ascertain the maximum thickness of the 3D cell space for which hypoxic regions can be avoided. For the configuration of the test device of the current study, this translates to clarifying what height of the 3D cell space that can be used to avoid the formation of hypoxic regions near the base of the cell space (e.g., furthest from the O_2 supply). It is important to note that the optimal height (or thickness) of the cell space that the CFD model would predict would of course strongly depend on the O_2 consumption rate (S_{oxy}) of the target cell space. This capability is demonstrated in Table 2.2 for 6.25 ms^{-1} flow of media having 6.85 mg/L of dissolved oxygen content.

As shown, for different O_2 consumption rates (S_{oxy}) values of the cell space, the corresponding maximum thicknesses of the cell space experiencing normoxic conditions is tabulated. The results indicate that with increases in the S_{oxy} values -- i.e.,with higher cell packing densities within the 3D cell space -- the CFD model recommends the use of thinner cell space dimensions.

TABLE 2.2: Depth of oxygen penetration with respect to oxygen consumption rate of the cells within the cell space for dissolved oxygen content in media of 6.85 mg/l.

Oxygen consumption rate per unit area within the cell space, S_{oxy} (kg/m^3)	Depth of Oxygen penetration through 3D cell space (mm)	Oxygen consumption rate per unit area within the cell space, S_{oxy}(kg/m3)	Depth of Oxygen penetration through 3D cell space (mm)
1.00E-09	0.01016	1.00E-11	0.84258
1.00E-10	0.08916	8.75E-12	0.92316
8.00E-11	0.149	7.50E-12	1.02552
6.00E-11	0.20611	6.25E-12	1.13112
4.00E-11	0.31492	5.00E-12	1.2
2.00E-11	0.53039	3.00E-12	1.2
1.50E-11	0.67109	1.00E-12	1.2

2.6 Discussion

In the current work, a computational model was developed to predict and visualize the O_2 distribution within a 3D cell space. An expectation of developing such a model was that it could be used by practitioners during the planning and evaluation stages of bioreactor design to help ensure the effectiveness of such flow devices. While this is certainly not the first O_2 transport model applied to bioreactors [40, 41, 90, 94], its value is that its results are applicable to more than one design -- irrespective of the cell type, number of cells, media conditions and flow conditions. This was achieved by developing the model around a test setup that incorporated some of the broader features that multiple bioreactor configurations share in common. More specifically, the results of this study can be correlated with fixed wall bioreactors designs such as hollow fiber [26, 27], flat plate [83], and perfused bed bioreactors [18], yet it is not applicable to rotating wall bioreactor designs [95, 96]. Furthermore, the fact that the model's dimensions and parameters can be easily altered enables it to be used as a very flexible and versatile predictive tool.

To demonstrate the accuracy and potential of the model in predicting transport, this study took advantage of the analogies between mass and heat transport [97-99]. A complementary transient heat conduction acellular experiment was conducted using the test device (recall Fig 2.3). The strong correlation between the measurements and the computational model's predictions (whereby differences between the values was 2% or less for the majority of the sample regions), enabled the validation of the model's accuracy.

The model was then applied to predict the steady state O_2 transport for a number of varied experimental arrangements. Two assumptions were taken into consideration for simplifying the computational model. Firstly, it was assumed that the cells are uniformly distributed throughout the 3D cell space. This might not necessarily hold true in practice cases unless the cell seeding procedure was done with utmost care. However, such an uneven distribution of cells can be approximately modeled by sub-dividing the cell space volume in the model into multiple smaller volumes and assuming uniform cell distribution and O_2 consumption rate within these individual volumes. The more the sub-divided volumes, the more close it resembles the practical scenario. Secondly, the O_2 consumption by the individual cells was assumed to be constant. But a much better approximation would be to assume Michaelis -Menten reaction wherein the consumption of O_2 by cells is considered to vary with respect to the O_2 available to the cells, that is, if the O_2 available to the cells is low, then the cells can alter their functionality such that they can survive by consumption of lower quantity of O_2 [100-102]. Though the current computational model does not incorporate these two features, the computational model has the capability to be further expanded to incorporate them.

The strength of the current computational model is that it can be employed for a wide range of scenarios with respect to bioreactors. In the following discussions, some of the predictive capabilities of the model are discussed with specific reference to a 3D liver system (primary rat hepatocytes embedded in a collagen sponge matrix). The concepts from these predictions provide us with an insight on some of the major considerations the bioreactor users have to account for.

The most important consideration in designing bioreactors is to avoid regions of hypoxia which directly affects the performance of the bioreactors. The model identifies such regions and it is found to exist especially adjacent to the walls. The reason for the poor O_2 transport in near the walls is that the media permeates with a low velocity due to flow boundary layer effects along the walls. Therefore, the replenishment of the O_2 in these regions is impeded, resulting in the formation of an O_2 boundary layer near the walls. The thickness of this O_2 boundary layer is directly dependent on the flow velocity and the O_2 consumption capacity of the cells. Thus, the boundary layer concept for the media flow as well as O_2 becomes an important factor for bio-engineered device designers. This suggests that avoidance of contours such as sharp corners and dumps, which can potentially increase the boundary layer thickness, is important.

Furthermore, the O_2 distribution can be influenced by a number of factors such as the number and type of cells embedded in the 3D cell space, the O_2 content in the supply media, the thickness and dimension of the cell space etc. Using the model, varying one of the above factors keeping the other factors unaltered, helps to optimize its value for obtaining better O_2 distribution. Some of such predictive capabilities of model are discussed.

One of the significant capabilities of the model is its ability to visualize and quantitatively assess the effect of convection on O_2 transport. As an illustration, from the results pertaining to Fig 2.7 and 2.8, it was seen that the middle cell space had better O_2 transport than the other ones. This is mainly attributed to the fact that a more uniform convection flow of media with lesser disturbances prevailed over the middle cell space (refer Fig 2.9), thus improving O_2 transport [25, 26].

Another significant capability of the model is its ability to optimize the dimension of the cell space and its cell density. As an illustration, if the O_2 consumption rate within the 3D cell space is very high (either due to high cell density or due to the cell type), hypoxic regions would develop if the thickness is not optimized. This is evident from the decrease in the percentage of normoxic region with increase in S_{oxy} value in Fig 2.10 and 2.11. On the contrary, if the thickness is unaltered, then the number of cells within the cell space needs to be optimized to void hypoxia. For example, using the current reference of primary hepatocytes in collagen sponge, if the thickness is set to 0.5mm, then the number of cells must be optimized such that the calculated S_{oxy} value is less than 2e-11 kgm^{-3}.

Also, the O_2 content in the supply media can be optimized such that regions of hypoxia and hyperoxia are avoided. As an illustration, from Fig 2.13, for a S_{oxy} value of 1e-11, a 5 mg/ml O_2 media supply is able to provide sufficient O_2 to only 32.79% of the volume of the cell space, in contrast to 78.27% of the volume being normoxic if a 10mg/ml O_2 media supply was used instead. Thus Fig. 2.13 demonstrates how use of the computational model can be helpful to tailor the cell space in accordance with level of O_2 it is being supplied.

In addition, the model can also be utilized to predict the arrangement of cells within 3D cell space region. For example, if we have a media source with 8 mg/ml of dissolved O_2, then it is recommended to maintain a lesser cell density near wall boundaries. On the contrary, if the supply media contains very high levels of dissolved O_2 (> 10mg/ml) then hyperoxic condition may prevail in the cell space and it would be recommended to have a very high cell density near the boundary layer region. In such cases, having a thick boundary layer can actually have a positive effect on cell survival.

The model also has the capability to analyze O_2 transport within the 3D cell space for varying choice of the ECM material. This scenario has not been explicitly illustrated in the results. However, from Table 2.2, it can be seen that the O_2 transport can extend up to a thickness of about 1.2 cm with the collagen sponge. On the contrary, Nui et al.,[39] used an enhanced collagen gel matrix to support primary rat hepatocytes and found that the maximum thickness for which normoxic condition prevailed was only about 0.5 mm. This suggests that the collagen sponge is more effective that collagen gel with respect to O_2 transport. The high O_2 transport in a collagen sponge can be attributed to its porosity and permeability, further suggesting that use of high permeable ECM improves the O_2 transport immensely.

With such predictive capability, the current CFD model can prove to be a useful tool in planning and setting up a variety of bio-medical device related experiments. It can be used as an effective tool for understanding the mechanism of O_2 distribution within a 3D cell space. Hence this CFD model turns out to be valuable source which could help design effective bio-engineered devices as well as help in design optimizing various experimental trial and errors, thus reducing experimental time scales and costs.

CHAPTER 3: OPTIMIZATION OF CRYOPROTOCOL FOR CRYOPRESERVATION OF BIOLOGICAL TISSUES AND TISSUE EQUIVALENTS

3.1 Summary

Since biologically active cells and tissues are used in research and clinical studies for a variety of applications, it would be helpful for them to be readily available as needed by the practitioner. One strategy for achieving this is the cryopreservation of biological cells and tissues. Yet cryopreservation success is governed by the appropriateness of the cryoprotocol used, and developing suitable cryoprotocols becomes more complex as dimensions of the biological increase. This study was planned to help alleviate this obstacle. More specifically, a user friendly computational package – Multiscale Modeling Tool (MMT) has been developed to predict and compare the effectiveness of various cryoprotocols in storing biological tissue equivalents. The package is a multiscale tool composed of a macroscale model and a microscale model. The macroscale model predicts the non-linear thermal history and cryoprotective additive (CPA) concentration profile across a 3D tissue/tissue equivalent when it is exposed to a prescribed cryoprotocol. The microscale model uses results from the macroscale model to predict subsequent cellular water transport and probability of ice formation (PIIF) during the freezing process. Since PIIF is directly related to cell death, various cryoprotocols can be tested to optimize which cryoprotocol should be used for a given tissue/tissue equivalent. Hence this package is expected to offer a cost effective solution for designing

protocols for successful cryopreservation of 3D biologically active tissues, tissue equivalents, and organs.

3.2 Introduction

Several industries rely on the availability of viable cells, tissues, and/or organs for their success. Especially, the tissue and organ transplant industry and the pharmaceutical industry, which rely on the availability of suitable tissues and organs to benefit patient care [103, 104]. Unfortunately, a major challenge for these industries is the off-the-shelf availability of desired cell, tissue, and/or organ, i.e., they are often not readily available when needed for the targeted application. One method for increasing their availability is to utilize cryopreservation technology for the safe storage of cells, tissues, and organs at low temperatures.

A promising technique for the cryopreservation of tissue equivalents is the freeze-thaw method. It utilizes controlled rate freezing of tissue equivalents to store them safely at low temperatures in a crystalline form [48]. The freeze-thaw method has been very effective for cryopreservation of sperm, blood, skin, embryos, and individual liver cells [105-108]. The freeze injury occurring during freeze thaw method is often ascribed to two biophysically mediated factors: dehydration of cells at slow cooling rates and intracellular ice formation (IIF) at high cooling rates [109].

Extensive studies for various cell types using experimental methods and numerical models have been performed to understand the influence of the two biophysical factors during freezing [49, 58, 111, 112]. It has been demonstrated that IIF propagation in tissues differs significantly from that in isolated cells [112, 113]. This is primarily due to the fact that transport (thermal, mass and water) histories experienced by

the tissue during cryoprotocols is heterogeneous [114, 115]. Hence, for effective cryopreservation of tissues and tissue equivalents, it is critical to optimize the cryoprotocols by considering the effects of thermal and concentration gradients, the kinetics of water loss and the likelihood of IIF as a function of cooling rate.

So far, the development of protocols for safely storing tissue equivalents at low temperature has mostly been through empirical approaches. To aid such an approach, a number of computational models have been proposed [59, 61, 116, 117]. However, these models have been developed for specific experimental conditions and devices, restricting broader use of the models. So, in the current work, a user friendly multi-scale computational package was developed for simple geometries to estimate the probability of intra cellular ice formation (PIIF) in tissues based on the cryoprotocol employed.

The Multisacle Modeling Tool (MMT) package was designed to enable comparison of various cryoprotocols numerically, thus assisting in estimating an optimized cryoprotocol for specific tissues. Its user friendly features make it easy for a wider group of personnel, from diverse fields, to utilize the package. Thus the package has the potential to aid the clinical, commercial, and research industries in improving the off-the-shelf availability of tissues and tissue equivalents.

3.3 Computational Methods

The Multi-scale Modeling Tool (MMT) was developed by combination of two sub-models. The macro model was based on the computational model developed by Balasubramanian and Coger [61] which predicts the temperature and concentration (for CPA) history experienced by the tissue during the freezing process, for a prescribed cryoprotocol. The temperature distribution over time within the tissue was modeled based

on the heat transfer equation and incorporated solid-liquid phase transition which takes place during the freezing process [62]. The concentration distribution of the CPA was governed by the mass transport equation [63]. The micro model was developed based on the work of Mayur and Coger [65] which utilizes nucleation theory [64] and the water transport equation [64] to predict the cell survival from the probability of IIF. In addition, the MMT was coupled to a HTML and database management system (DBMS) interface to make it user friendly.

3.3.1 Macro Model

The macro model of the MMT was used to predict temperature distributions and concentration gradients within the tissue at any point of time during the freezing process, for a given cryoprotocol. The governing equations of numerically predicting transient thermal and concentration distribution are discussed in the following sections.

3.3.1.1 Heat transport model

The thermal history experienced by the cryopreserved tissue is predicted using the heat transport equation shown in Eq. 3.1 [118, 119]. It takes into consideration the liquid to solid phase transformation that occurs during the freezing process:

$$\rho \frac{\partial H}{\partial t} = k\nabla^2 T \tag{3.1}$$

$$H = \left[\beta C_l + (1-\beta) C_s\right] T + \beta \left(C_s - C_l\right) T_m + \beta L \tag{3.2}$$

$$\beta = \frac{T - T_{sol}}{T_{liq} - T_{sol}} \tag{3.3}$$

$$k_{mushy} = \beta k_l + (1-\beta) k_s \tag{3.4}$$

where C is the specific heat capacity (kJ/kg K) of the tissue in liquid phase l and solid phase s, T_m is the melting point temperature (K), L is the latent heat of fusion (kJ/ kg), k is the thermal conductivity (W/ m K), T_{sol} is the solidus temperature (K) and T_{liq} is the

liquidus temperature (K). A mushy region exists in the system when the tissue is partly frozen. A linear transition in properties was assumed between the liquid and solid phase, as given by the factor β and the thermal conductivity in this region is given by Eq 3.4.

3.3.1.2 Mass transport model

In order to represent the distribution of the CPA within the sample, the macro model makes use of the mass transport equation, given by Eq 2.5.

$$\frac{\partial c}{\partial t} = \nabla.\left(D\nabla c\right) + S \tag{3.5}$$

where c is the concentration of the CPA at any point in the tissue (mol/m^3), D is the diffusivity of the CPA in the tissue (m^2/s) and S is the source term (mol/m^3). In the current model, there is not generation of CPA within the tissue sample and hence the source term S is zero. It is to be noted that the time scale for this model is different from that of the heat transport model. In the former, the time scale is for the duration of the CPA loading process where in the latter, the time scale is for the duration of the freezing process.

3.3.2 Micro Model

The micro model utilizes the thermal and concentration gradients obtained from the macro model prediction. Based on the thermal history experienced by the tissue, the micro model predicts the cellular water transport and the probability of IIF within the sample.

3.3.2.1 Water transport Model

The water transport model used in the study was based on the work done by Mazur [66] and later modified by Toner and coworkers [111, 120]. Briefly, the osmotic balance between the intracellular space and the extracellular space is affected by the

solute concentration in the extracellular space during freezing. Eq. 3.6 models the water transport across the cell membrane required to achieve chemical equilibrium between the intracellular and extracellular space.

$$\frac{dV_{is}}{dt} = \frac{L_p ART}{v_w}\left(\frac{\Delta H_f}{R}\left(\frac{1}{T_{m,0}} - \frac{1}{T}\right) - \ln\left(\frac{V_{is} - (n_s v_s + n_d v_d)}{V_{is} - (n_s v_s + n_d v_d) + v_w(2n_s + n_d)}\right)\right) \quad (3.6)$$

In the above equations, V is the volume of the cell (μm^3); T is the absolute temperature (K); $T_{m,0}$ is the reference temperature (273 K); A is the surface area of the cell (μm^2); R is the universal gas constant (8.314 J/mol K); v_w is the molar volume of water (μm^3/mol); v_s is the disassociation coefficient of salt; v_d is the disassociation coefficient of the CPA; n_s is the number of moles of salt in the cell (mol); L_p is the hydraulic permeability of the cell (μm^3/N s); and ΔH_f is the latent heat of fusion for water (kJ/mol).

Variations in cell membrane permeability were modeled using an Arrhenius relationship [119] as given by the following equation:

$$L_p = L_{pg} \exp\left(\frac{E_a}{R}\left(\frac{1}{T_{m,0}} - \frac{1}{T}\right)\right) \quad (3.7)$$

where L_{pg} is the hydraulic permeability (m^3/ Ns)at the reference temperature of 273 K; and E_a is the activation of energy for water transport across the membrane (kJ/mol).

3.3.2.2 Intracellular Ice formation

The predictions for the probability of IIF (PIIF) was based on the nucleation theory [64].The IIF model used in the study was based on the formulations developed by Toner et al. [111]. It incorporates the IIF in the tissue due to heterogenous and/or

homogenous nucleation mechanisms. The PIIF as a function of concentration, temperature and time is given by Eq. 3.8

$$PIIF = 1 - \exp\left(- \int_{T_0(t)}^{T(t)} A(t) I(c,T) dt \right) \tag{3.8}$$

$$I(c,T) = \Omega(c,T) \exp\left(\frac{-k(c,T) T_m^5}{T^2 \Delta T^2} \right) \tag{3.9}$$

where $A(t)$ is an effective plasma membrane surface area for nucleation (m^2), I is the nucleation rate, T_m is the melting temperature of the solution (K), ΔT is the super cooling (K), k is the thermodynamic rate coefficient and Ω is the kinetic rate coefficient ($m^{-2}s^{-1}$). The thermodynamic rate coefficient and the kinetic rate coefficient were determined for heterogeneous and homogeneous nucleation mechanism separately as indicated in Karlsson et al. [120, 122].

3.3.3 Discretization of the Equation

The MMT was modeled to predict the thermal and concentration distribution and the resulting probability of IIFfor the two simple geometries shown in Fig 3.1. Fig 3.1 also shows an illustration of the applicability of such geometries to bioreactor designs.

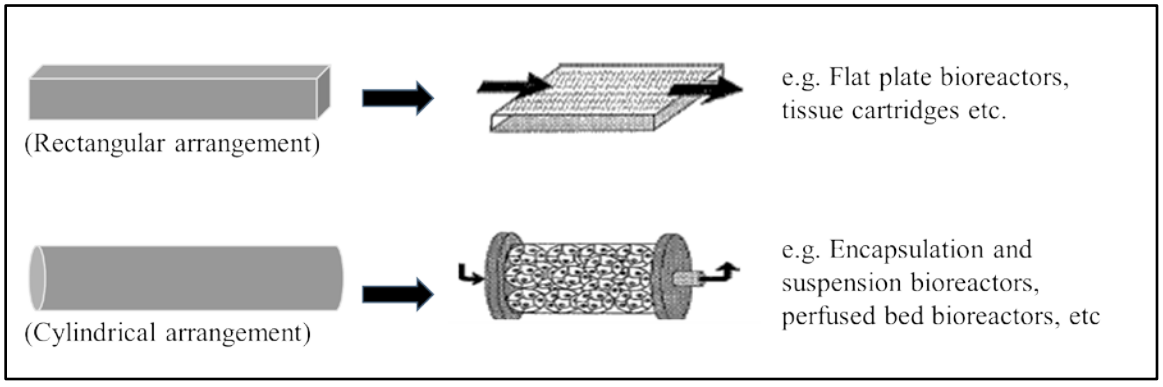

FIGURE 3.1: Geometry of the tissues considered in the MMT package and illustrations of their applications. The bioreactors shown are reprint from [18].

Thus the governing equations for the macro and micro model (Eq. 3.1 – 3.9) were discretized for two coordinate systems – the rectangular and the cylindrical coordinate systems. The equations were discretized using Crank-Nicolson method [123]. It utilizes trapezoidal rule for time discretization and forward and backward Euler method for space discretization. The Gauss Seidel iteration iterations were used to arrive at the approximate solution [124, 125]. The iterations were performed using Matlab (MathWorks, Natick, Massachusetts) software.

3.3.4 User Friendly Interfacing

The macro and micro models of the MMT were coupled with a Hyper Text Markup Language (HTML) coding to enable the user to input the dimension of the tissue, the cryoprotocols, and the required material and biophysical properties for the model. Two HTML pages were created using Microsoft Visual Studio 2008 (Microsoft Corp, Redmond, WA) to get the input from the users. The HTML pages were designed to be assessed through any web browsers, like Internet Explorer, Mozilla Firefox or Google Chrome. C –Sharp console embedded within Microsoft Visual Studio 2008 was then used to bridge the communication between the HTML pages and the Matlab codes.

In addition, the C-Sharp scripting also interfaced with a Database Management System (DBMS). The DBMS used for this application was done using Extensible Markup Language (XML) (.Net framework, Microsoft Corp., Redmond, WA). The XML interface enables the user to store the materials and biophysical properties used for the model and it can be retrieved whenever required. It reduces the hassle of inputting data multiple times for the same tissue. Thus, these features such as HTML and DBMS help create a user interface that is easy to use.

3.4 Material and Methods

To demonstrate the capability and application of the computational package, the model's predictions were compared to experimental results. For these experiments, primary rat hepatocytes cultured in a collagen gel matrix were cryopreserved. Details of the experimental process appear below.

3.4.1 Isolation and Culture of Hepatocytes

Sprague-Dawley male rats weighing 150-280 g were fasted 24 hours prior to isolation[‡] and hepatocytes were isolated by collagenase perfusion method [126]. The hepatocytes from the digested liver were isolated by mechanical disruption and centrifuged (Thermo IEC CEntra-CL3R, Thermo Scientific, MA) at 50 x g for 3 minutes. The viability of the centrifuged hepatocytes was evaluated immediately using trypan blue exclusion assay (Sigma-Aldrich, St. Louis, MO). Hepatocytes were then suspended in the culture media containing DMEM (Invitrogen, Gaithersburg, MD), sodium bicarbonate (3.7g/L), insulin (500 U/L), epidermal growth factor (20 µg/L), hydrocortisone (7.5 mg/L), 1% (v/v) of antibiotic/antimycotic solution (JR Scientific, Woodland, CA) and 10% (v/v) fetal bovine serum (HyClone, Thermo Scientific, Waltham, MA).

For the extracellular matrix, collagen type I gel was first prepared by adding 8 parts of 1.1 mg/mL PureCol collagen (Advanced BioMatrix, San Diego, CA) to 1 part of 10X DMEM solution. The pH was adjusted to 7.4 with 0.1N HCl and/or 0.1N NaOH. Next 0.5 mL of the prepared collagen was then coated on the 35 mm diameter tissue culture plates and incubated for an hour at 37^{o}C, 5% $C0_2$ for gelation. Then 2 X 10^6 cells were seeded in each tissue culture plate, and incubated at 37^{o}C, 5% $C0_2$ for 4 hours. Then

iii. [‡] The isolation of liver from rats was performed by Dr. Charles Lee from UNC, Charlotte.

a second 0.5ml collagen layer was layered over the cells to create a sandwich culture and incubated for 24 hours with 1 mL DMEM media.

3.4.2 Cryopreservation of the Sandwich Culture

The sandwich culture plates were placed on ice and then 2M DMSO in DMEM solution was added to them, incubated on ice for 10 minutes. Then the culture plates were transferred to the CryoMed Control Rate freezer (Thermo Forma, Waltham, MA) in cryobags and cryopreserved based on the cryoprotocols shown in Fig 3.2. The cryoprotocol CYP1 does not have any isothermal step until a temperature of -80^{o}C is reached whereas the CYP2 adopted from [134] has a 15 minutes isothermal step at -20^{o}C. The cryopreserved sandwich cultures in the cryobags were then transferred to a -80^{o}C Revco freezer (Kendro Laboratory, Asheville, NC) and stored for a week.

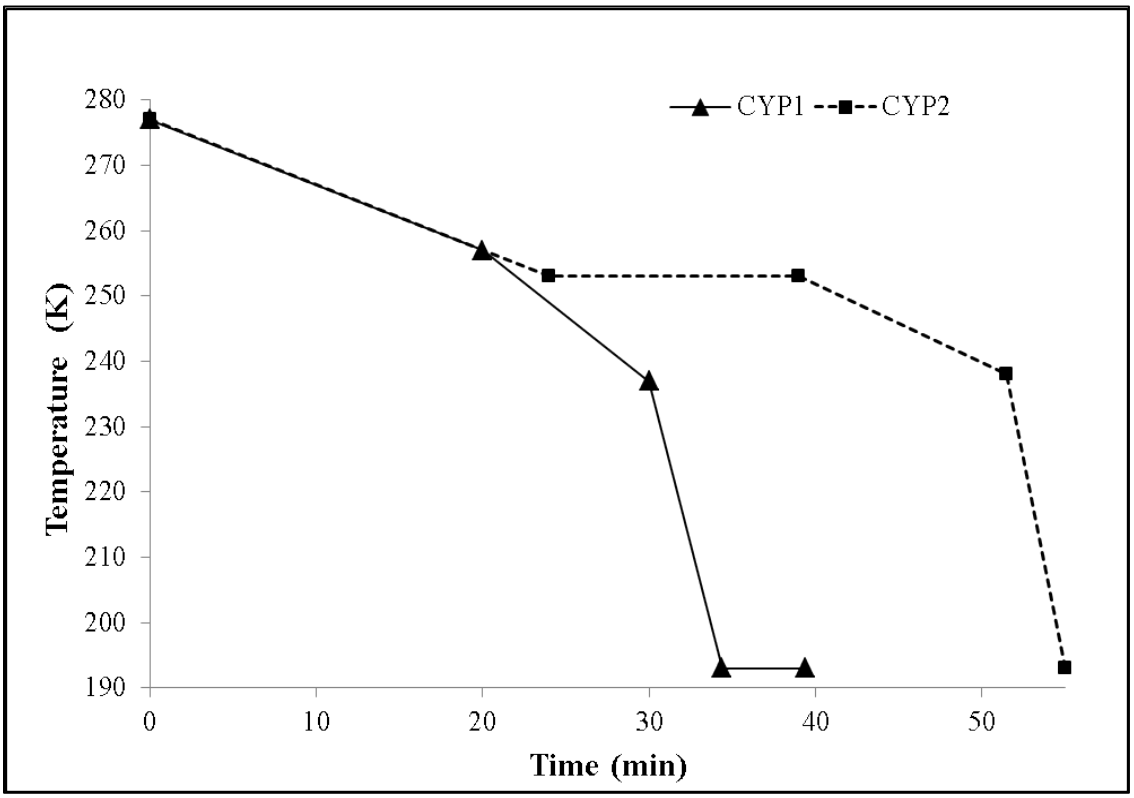

FIGURE 3.2: The two cyroprotocols used for cryopreservation of the sandwich hepatocyte cultures.

3.4.3 Cell Viability Assessment

The cryopreserved sandwich hepatocyte cultures were thawed via rapid immersion in a water bath maintained at 37^{o}C. The cultures were then washed twice with DMEM media to remove the DMSO from the sandwich culture. Then 1mL of DMEM media was added to the sandwich cultures and placed in an incubator at 37^{o}C, 5% CO_2 for 24 hours to allow cells to recuperate from the freeze-thaw process. The next day, culture plates were washed with 1X PBS solution and incubated with 1 µg/mL concentration of Hoechst and 2 µM Ethidium Homodimer (Molecular Probes, Eugene, OR) in PBS for 30 minutes. The cells were then fixed by adding 1mL of 10% formalin (VWR, West Chester, PA) and incubating for 20 minutes. Later, the cell viability was examined by confocal microscopy with DAPI (excitation 358nm; emission 461nm) and Texas red (excitation 596nm; emission 620nm) filters. The fluorescent images obtained were analyzed using MetaMorph Imaging System (Molecular Devices, Sunnyvale, CA).

3.5 Results

3.5.1 HTML Pages for User Inputs

Examples of the HTML pages created to improve the user friendliness of the MMT model are shown in Fig 3.3 and Fig 3.4. In the illustration, the pages were executed in Mozilla Firefox internet browser. The first HTML pages obtain the key MMT inputs such as the tissue's dimensions, details of the cryoprotocol to be analyzed, and details of the CPA loading steps and time. On clicking the "NEXT PAGE" button, the second HTML page is opened which allows the user to enter the material properties of the tissue and the biophysical parameters for the system under investigation. When the page is submitted, the material properties and the biophysical parameters are stored in the

database and also feed the inputs to the Macro model. A drop down box feature in the second HTML, allows the user to retrieve the materials properties already stored in the database of the MMT.

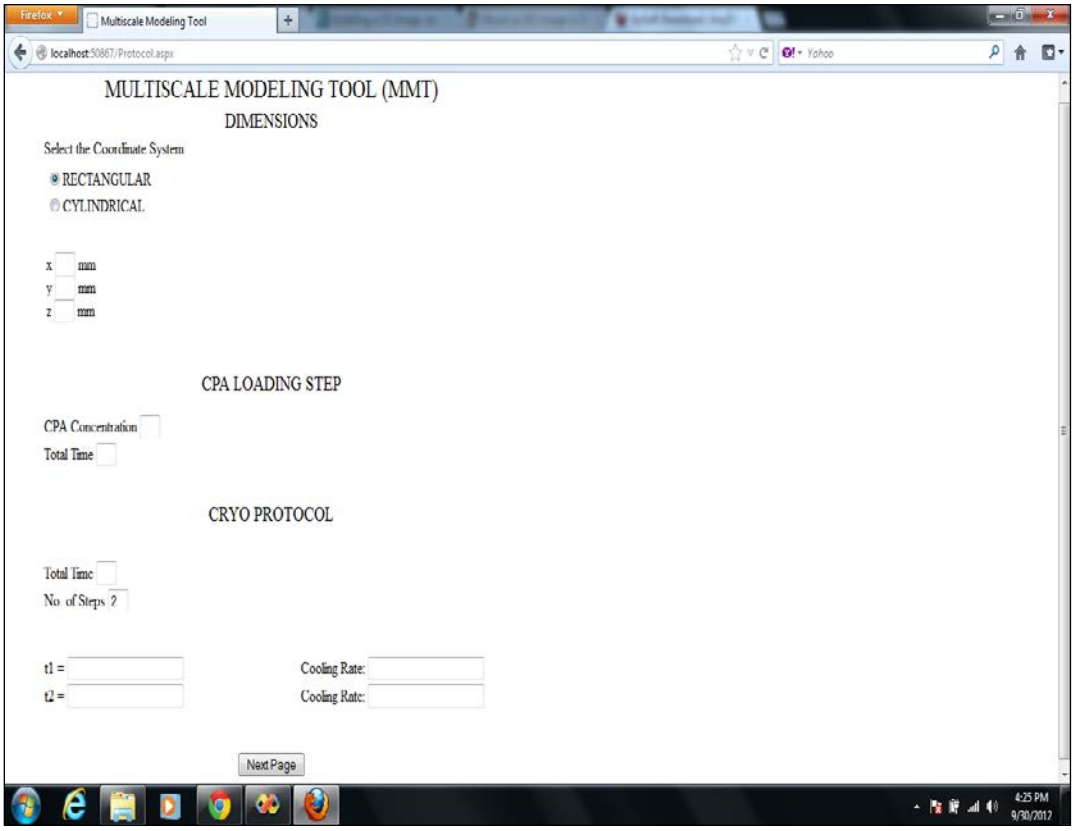

FIGURE 3.3: Screenshot of the first HTML page for the user to specify the tissue dimension and the cryoprotocol steps.

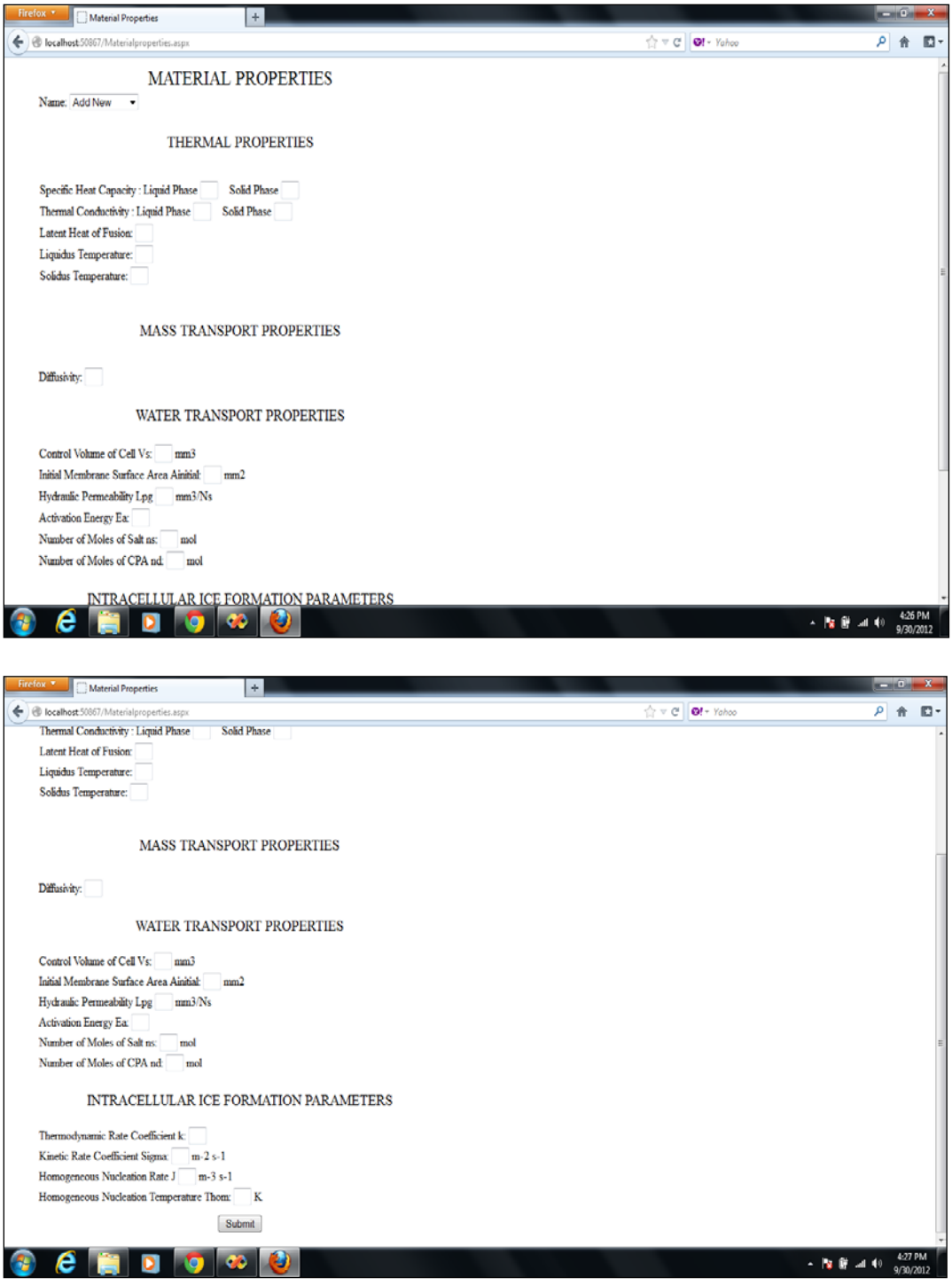

FIGURE 3.4: Screenshots of the second HTML page for the user to specify the material properties of the tissue and the biophysical parameter of the system.

3.5.2 Predictions of the Macro and Micro Model

In order to elucidate capability of the MMT, the predictions of the models for a 2 cm x 2 cm x 2 cm liver tissue subjected to the cryoprotocol CYP1 (Fig 3.2) are demonstrated. The material properties and the biophysical parameters considered for predictions are provided in Table 3.1. The model's output are obtained as a data sheet which can be analyzed using various data analysis software such as Techplot, Microsoft Excel etc. In the current illustration, Microsoft Excel was used for the data analysis.

TABLE.3.1: Material properties and biophysical parameters used in simulation of MMT [120, 158].

Symbol	Description	Values	Unit
ρ_l	Density of the liver tissue as liquid phase	1060	kg/m^3
ρ_s	Density of the liver tissue as solid phase	916.7	kg/m^3
C_l	Specific heat capacity in liquid phase	4.56	J/kg K
C_s	Specific heat capacity in solid phase	2.11	J/kg K
k_l	Thermal conductivity in liquid phase	0.47	W/m K
k_s	Thermal conductivity in solid phase	1.7	W/m K
T_l	Liquidus temperature (temperature when ice begins to form)	270	K
T_s	Solidus temperature (temperature when ice forms completely)	267	K
T_{hom}	Homogeneous nucleation temperature	234.35	K
L	Latent heat of fusion	6020	J/mol
V_{is}	Control volume of the hepatocytes	$7.7x10^{-7}$	m^3
A	Initial surface area of the cells	$1.89x10^{-9}$	m^2
L_{pg}	Hydraulic permeability at 273K	$3.1x10^{-13}$	m^3/Ns
E_a	Activation energy for water transport	$2.9x10^5$	J/mol
R	Universal gas constant	8.314	J/kg K
Ω	Kinetic rate coefficient at 273 K	$9.7x10^{52}$	$m^{-2}s^{-1}$
κ	Thermodynamic rate coefficient	$1.16x10^{-3}$	-
J	Homogeneous nucleation rate	$1.7x10^{18}$	$m^{-2}s^{-1}$

A schematic of the liver tissue dimensions analyzed in this representative demonstration of the MMT is shown in Fig 3.5. It shows the mid XY plane of the 3D tissue. For such a sample, the model makes use of the symmetry of the geometry and computes the results for a 1 cm x 1 cm x 1cm region, as highlighted in Fig 3.6. Furthermore, in order to illustrate the model's predictions, the results along the line AO (shown in Fig 3.6) on the mid XY plane (z =0 cm) are shown in the following section. It is to be noted that the point O represents the center of the tissue sample whereas the "point A" falls on the edge (YZ plane at x = 1cm) of the tissue sample.

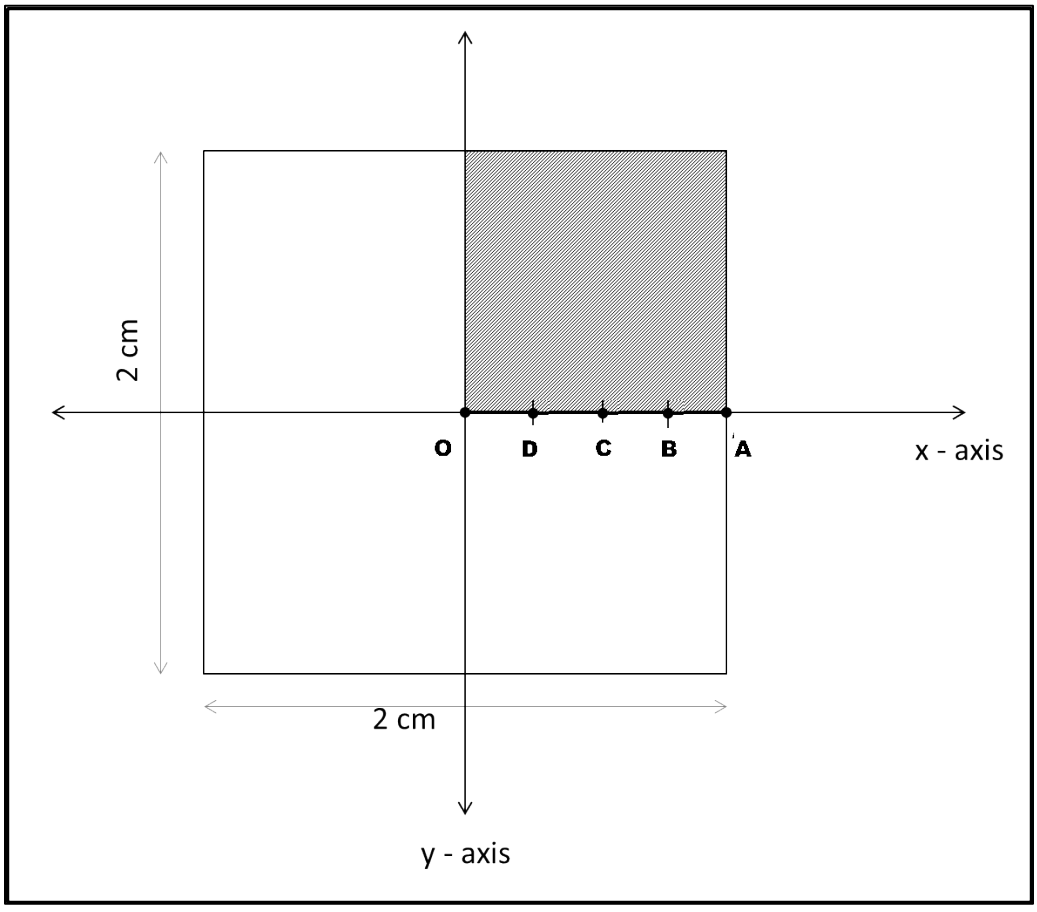

FIGURE 3.5: Schematic representation of the liver tissue used for illustration of the MMT package's predictive capabilities.

3.5.2.1 Distribution of the CPA concentration

The first step in the cryopreservation process is the loading of the CPA in the tissue sample. Ideally, a cryoprotective solution is added to the samples and incubated. The time of incubation is one of the control factors that determines the extent to which CPA can diffuse into the sample prior to the freezing process. In the current illustration, DMSO was considered as the CPA, and effective diffusion of the CPA in the region AO (shown in Fig 3.5) is plotted with respect to the time of incubation. Fig 3.6 depicts the concentration of the CPA into the cells along "line AO" as they were exposed to a fraction of the initial concentration of the CPA solution. It can be seen from this representative result that, with an increase in incubation time, more effective transport of the CPA to the center of the tissue is expected (point O). For shorter incubation periods (5 minutes in this illustration), the CPA concentration at the center of the tissue is very low. In practice, this could potentially lead to excessive dehydration of the cells in this region during the freezing process.

3.5.2.2 Thermal Response during Cryopreservation.

Following the CPA loading process, the freezing process is initiated at 277K. In modeling of the freezing process, it was assumed that metabolic activity of the cells are negligible below 277K, and so any further changes in the CPA distribution within the samples would have no effect on the cells' response.

The thermal history experienced by the cells along line AO (Fig 3.5) for the liver tissue sample in consideration is shown in Fig 3.7. The thermal response is shown for the first 15 minutes (a temperature range of 277K – 262K) of the cryoprotocol CP1 (Refer Fig 3.2). The results indicate a fairly linear heat transport into the tissue up to the liquidus

temperature (270 K). Below 270K, the phase change process is initiated and the liquid fraction starts to solidify. As a result, a mushy region of partial liquid and partial solid region exists in the tissue sample until the solidus temperature of 267K is reached. The phase change process and the existence of the mushy region can be identified by the non-linear temperature response in the tissue sample, as indicated in the graph (Fig 3.7). Below the solidus temperature, thermal variations within the sample become linear (not shown in the graph). These thermal responses were then utilized as the input for the micro model to predict the water transport behavior and probability of IIF.

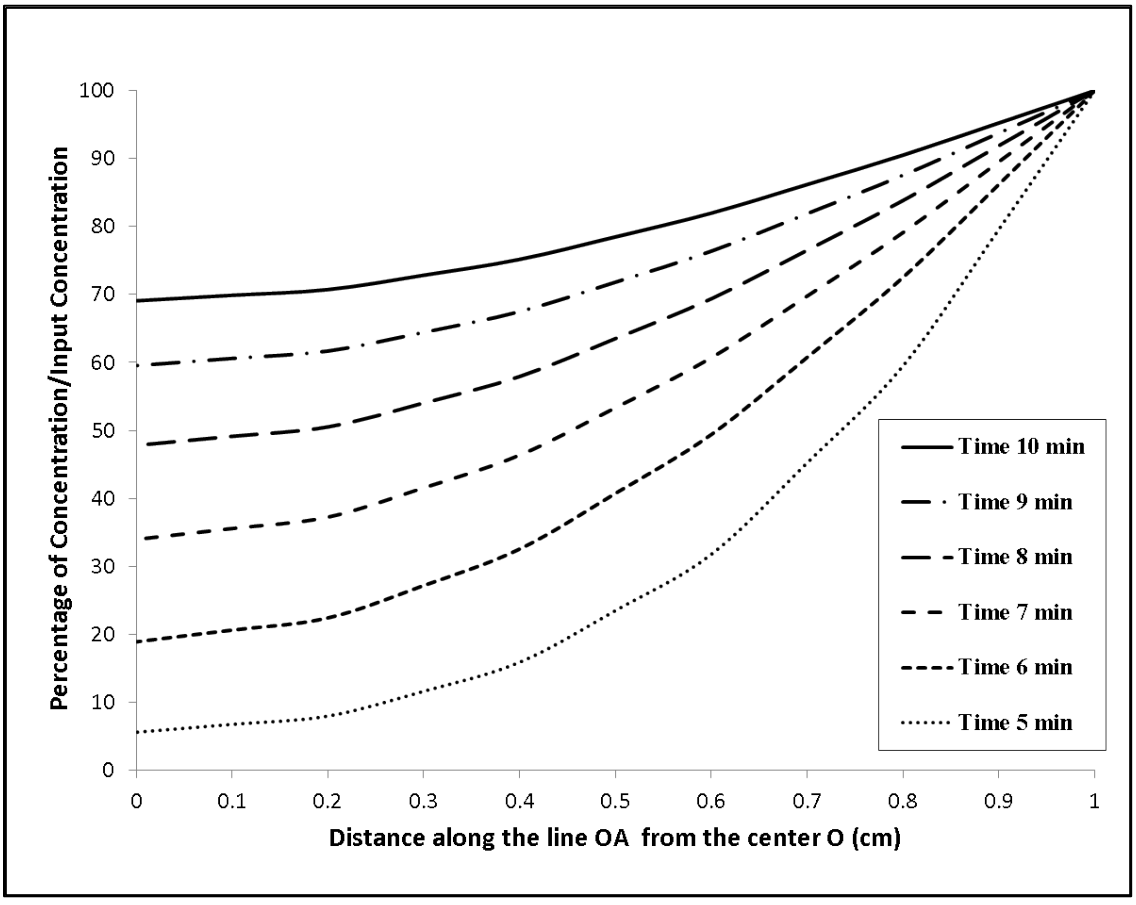

FIGURE 3.6: Concentration gradient of the CPA along the line AO of the tissue - with respect to varying time of incubation.

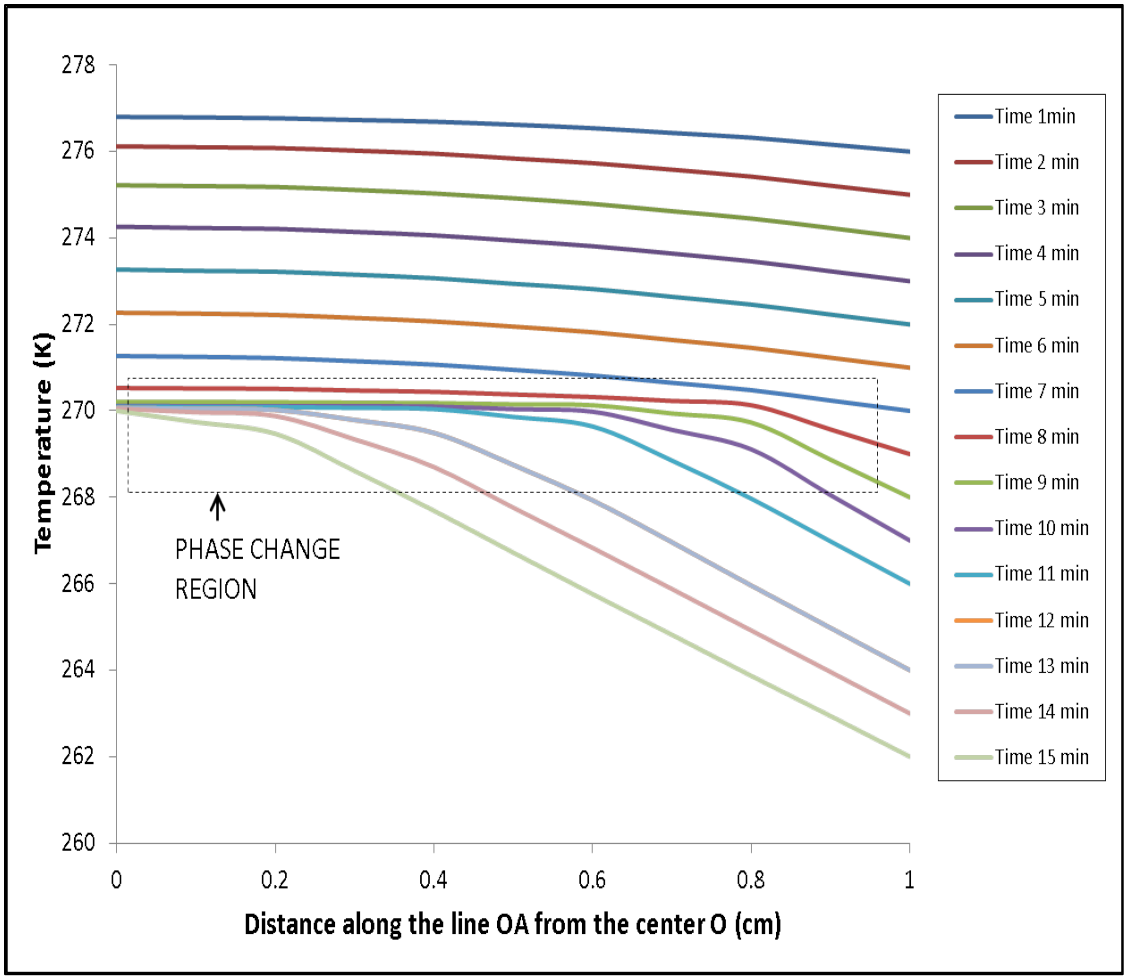

FIGURE 3.7: Temperature distributions along the line AO of the liver tissue for the first 15 minutes of the cryoprotocol CYP1.

3.5.2.3 Water transport

The cellular water transport effects were predicted using Eq. 3.6 for the tissue samples based on the effects of the thermal history from the macro model and the biophysical properties of the hepatocytes. Fig 3.8 demonstrates cellular water transport occurring at 5 locations on the line OA: 0 cm (point O), 0.25cm (point D), 0.5 cm (point C), 0.75 cm (point B) and 1 cm (point A) from the center of the tissue. The results predict that cellular water transport behavior of the cells at the center of the tissue sample (point O) is the highest. As shown in Fig. 3.8, cellular water transport is predicted to decrease

progressively with the increase in the distance from the center of the tissue (D, C, B and A respectively) and it is seen to be the lowest at point A, the region on the outer surface of the tissue directly exposed to the cooling convective flow.

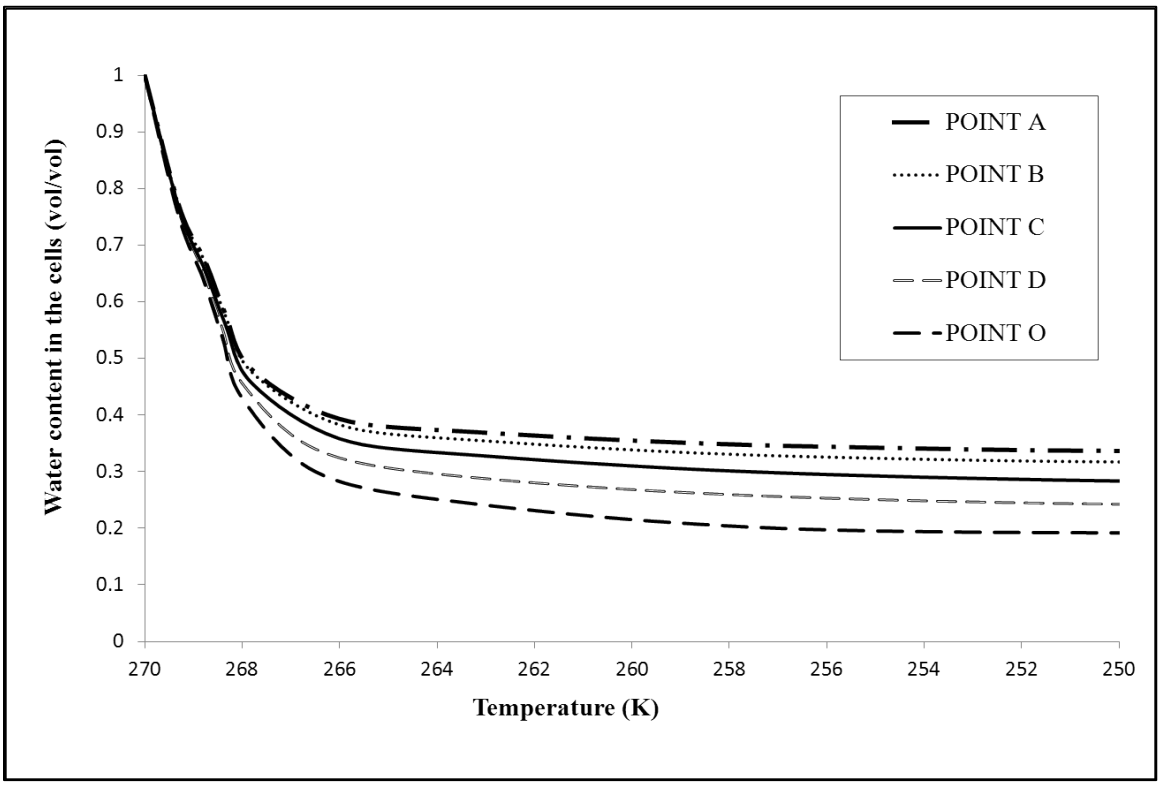

FIGURE 3.8: Normalized intracellular water content at five locations O, D, C, B and A at a normalized distance of 0, 0.25, 0.5, 0.75 and 1 respectively from the center of the sample liver tissue used to validate the MMT model.

3.5.2.4 Probability of intracellular ice formation.

Fig 3.9 demonstrates probability of IIF occurring at five points described in section 3.5.2.3. The graph indicated that the probability of IIF at different temperatures is fairly close for the five points and IIF can be avoided in the sample if the ice nucleation occurs at the temperature of 247.9K or a higher temperature. The probability of IIF is 50% at a nucleation temperature of around 244 K and for ice nucleation occurring below 241.5K, the PIIF is 100%. Since the viability of the cells in the tissue sample is affected

by the IIF, it is desired that the ice nucleation occurs at a temperature higher than 248K for the success of the cryoprotocol.

With such predictive capability of the MMT, it is possible to compare different cryoprotocols to optimize the cryopreservation process. In such cases, the cryoprotocol with the lowest ice nucleation temperature is desirable since the probability of heterogeneous as well as homogenous nucleation is higher at lower temperature.

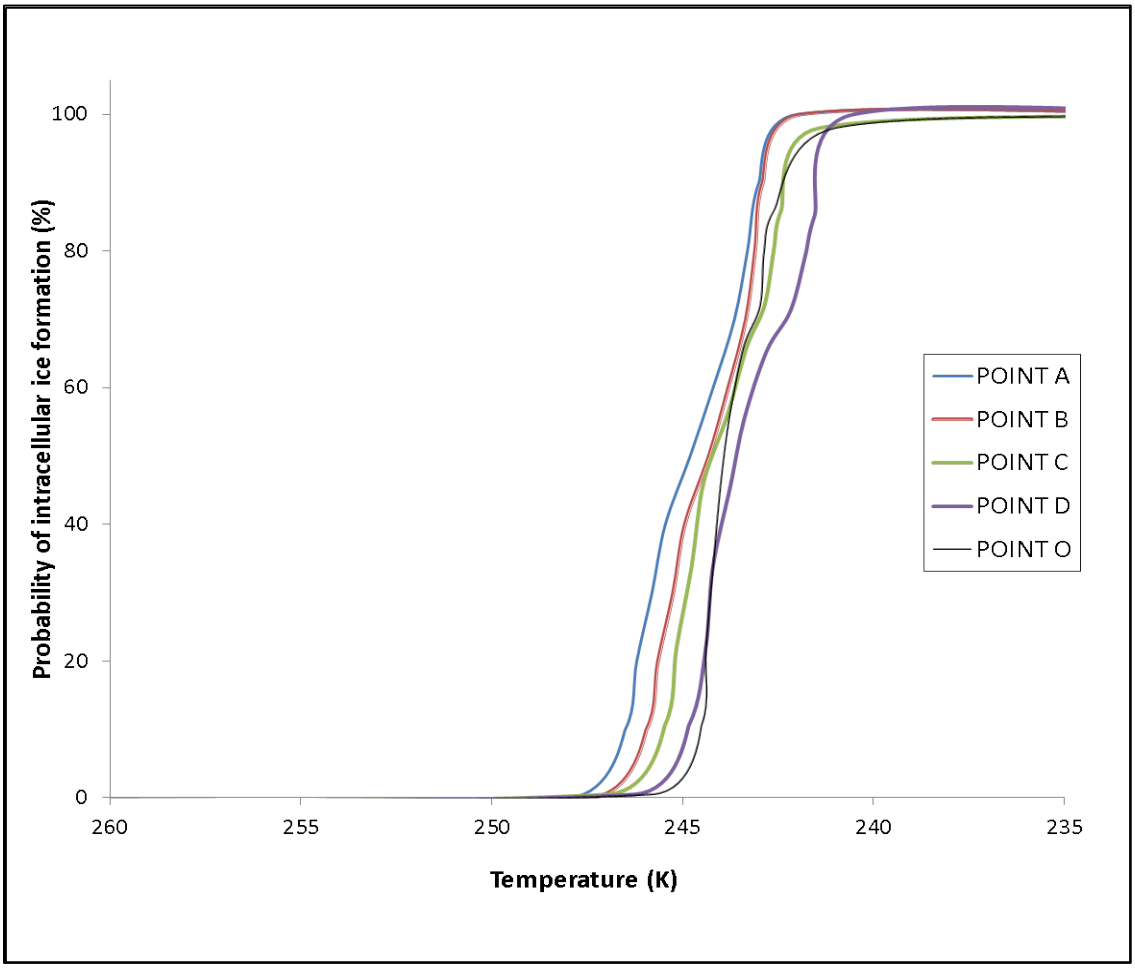

FIGURE 3.9: Probability of intracellular ice formation predicted at five locations O, D, C, B and A at a normalized distance of 0, 0.25, 0.5, 0.75 and 1 respectively from the center of the liver tissue.

3.5.3 Comparison of MMT's Prediction with Experimental Results

In order to validate the effectiveness of the computational package, the model's predictions were compared to experimental results. For these experiments, primary rat hepatocytes cultured in a collagen gel matrix was cryopreserved as described in Section 3.4. The viability of the cells at fields close to the center of the cultured samples was estimated using confocal microscopy and MetaMorph Imaging System. In the case of the computational predictions, the model was simulated for a cylindrical coordinate system with r=17.5mm and z = 10mm and the predictions for 50% PIIF at r = 0mm, z=5mm for two cryoprotocols (shown in Fig 3.3) were obtained.

The results of the MMT's prediction and the experimental cell viability are indicated in the Table 3.2. As per the model's prediction, the ice nucleation temperature for 50% PIIF was 245.94 K for CYP1 and 251.63 K for CYP2. In this case, the cryoprotocol with lower ice nucleation temperature is preferred, that is, CYP1 is more effective cryoprotocol than CYP2 as per the model's prediction. Likewise, the estimated cell viability at the center fields of the samples was 56% for CYP1 and 51% CYP2. Thus, both results indicate that the cryoprotocol CYP1 is more effective than CYP2 for the cryopreservation of the sandwich hepatocyte culture.

TABLE.3.2. Comparison of the MMT prediction and experimental cell viability

Cryoprotocol (Refer Fig 3.2)	Ice nucleation temperature for 50% PIIF predicted by the MMT (K)	Experimental cell viability for n=4 (Mean ± SE)
CYP1	245.94	56 ± 1.835
CYP2	251.63	51 ± 2.438

3.6 Discussion

The current study presents a user friendly computational tool for optimizing cryoprotocols for the safe storage of tissues and tissue equivalents. The numerical model of the MMT package was configured to analyze the cryopreservation effects on 3D tissues of simple geometry – rectangular and cylindrical. In the case of rectangular tissues, the governing equation were discretized and solved for a three dimensions (x, y and z) whereas for cylindrical tissues, only two dimensions (r and z) were required, assuming radial symmetry [127, 128].

The user friendly features of the MMT enables the user to provide key inputs such as the tissue or tissue equivalent's size and geometry, its material and biophysical properties, the cryoprotocol adopted etc. The drop down box in the HTML page 2 (Fig 3.4) allows the user to retrieve the material and biophysical property data from the XML database and displays the values in the appropriate text boxes. The user interface allows these values in the text boxes to be modified as per the users' requirements. But if the values retrieved from the database are modified, the interface would not allow the user to save the modified data in the database unless saved with a new name. To add new data to the database, the user needs to select "Add New" in the drop down box, provide the appropriate values in the text boxes and then click "Submit" button which will save the data to the XML database as well as provide the data as input to the macro and micro models for the MMT.

The concentration gradient of the CPA in the tissue is determined based on the user's input of the initial concentration in the cryoprotective solution and the time of incubation of the tissue in the CPA solution. The macro model of the MMT assumes a

one-step CPA loading process for the mass transport predictions. It is important to mention that this might not hold true for larger tissues. For large tissues, a multi-step loading process with increasing CPA concentration is recommended for effective loading and minimizing cell death by toxicity [129]. However, such a multi-step process can be easy added to the MMT if needed, by additional C – sharp scripting.

In addition, the model assumes that the cells in the tissue have negligible metabolic activity below 277K, such that further inflow of oxygen and other nutrients is not needed [130]. For this reason, concentration variations are analyzed only for the incubation period and not after the initiation of the freezing process. If the cell metabolic levels need to be considered for temperatures below 277 K, then it would be important to modify the macro model to incorporate a nutrient source for the cells (term S in Eq. 3.5).

The thermal history predicted by the model is based on the heat transport equation and incorporate the effects of phase change that occur during the freezing process. The phase change process initiates when the temperature of the tissue reaches the liquidus temperature. However, since the cooling rate is different for various regions within the tissue, some regions start to solidify while others are still in the liquid state [131]. Thus a mushy zone is established as the solid front propagates through the tissue, which results in a non-linearity in the heat transport as shown in Fig 3.7. The reason for such a non-linear variation is the difference in the thermal properties of the solid and liquid phase. Numerically modeling of this complex phase change phenomenon requires careful consideration. The current model assumes a first order relation between material properties of the liquid and solid phase, based on the liquidus-solidus fraction which is a standard norm used for phase change problems heat transfer [118, 129]. Increasing the

order of relation between the liquid and solid phase properties increase the numerical complexity and computational expense for limited improvement in the approximations [130].

The data from the macroscopic analysis are utilized by the micro model to evaluate cellular water transport in the tissue. The biophysical properties of the water transport are also critical for predicting cellular water transport [66]. The biophysical properties of water transport such as hydraulic permeability L_{pg} and activation energy of water transport across membrane E_a are system specific parameters and requires precise estimation for improved accuracy of the model's predictions [60].

The predicted cellular water transport in Fig 3.8 indicates that the cellular water transport was the highest at the center of the tissue. This is due so the relatively slower cooling rate experienced by the cells in the center of the tissue compared to the outer ones. With the slower cooling rate, the cells at the center of the tissue dehydrate more than the cells at the other cells [54, 111]. Another contributing factor is that the CPA concentration at the center of the tissue is relatively lower, which is expected to lead to faster dehydration of the cell [133, 134].

Similar to the cellular water transport predictions, the PIIF predictions are also dependent on the system configuration [115, 135]. Fig 3.9 predicted the PIIF for a liver tissue subjected to the cryoprotocol CYP1 (refer Fig 3.2). The prediction used the IIF parameters established by Karlsson et al. [120]. For the case considered, the results show that the temperature above which ice nucleation temperature needs to occur to avoid IIF is 247.9 K and fairly uniform throughout the tissue. Such a prediction might be due to the contribution of two contradicting factors: the thermal gradient and the water content of

the cells (Refer Fig 3.8). It is known that higher temperature gradients cause an increase in super cooling, leading to increased probability of heterogeneous ice nucleation on the plasma membrane (initiates at 258-268 K) [123, 136]. On the contrary, lower intracellular water content causes high intracellular solute concentration, resulting in increased probability of internal particle catalyzed heterogenous nucleation [134, 136]. Thus higher temperature gradients and lower water content increase the ice nucleation temperature. However, cells at the outer surface (point A) experience a higher thermal gradient, but have higher water content and vice versa for cells at the center of the sample (point O).

The PIIF results, and thereby the desired ice nucleation temperature thus estimated for a given cryoprotocol, can be used to compare the effectiveness of different cryoprotocols. During such comparisons, the cryoprotocol that enables ice nucleation to occur at the lowest temperature without any IIF is preferred. Thus the user friendly Multisacle Modeling tool (MMT) can be utilized to compare and optimize cryoprotocols for specific tissues, resulting in the potential for use in aiding the clinical, commercial, and research industries in improving the off-the-shelf availability of tissues and tissue equivalents. It also offers a cost effective solution for designing protocols for the successful cryopreservation of 3D biologically active tissues, tissue equivalents, and organs.

CHAPTER 4: EFFECTS OF OVER EXPRESSING AQUAPORINS ON THE CRYOPRESERVATION OF HEPATOCYTES.

4.1 Summary

Aquaporins (AQPs) are recently discovered family of proteins embedded in cellular membrane and acts as water transport channels. During cryopreservation, these water channel proteins are critical in regulating water transport across cellular membranes and preventing osmotic damages. Since cryopreservation of liver cells (hepatocytes), tissues and slices has been a major challenge over several decades and it is known that hepatocytes contain AQP8 and AQP9, we hypothesize that increasing the localization of these AQPs on the cellular membrane would help prevent osmotic damages to hepatocytes during cryopreservation. Freshly isolated rat hepatocytes were cultured on a collagen gel extracellular matrix (ECM) and treated with DiButyryl cAMP (Bt_2cAMP)/ Glucagon to increase AQP8 quantity at the cell membrane. Treatment of hepatocytes with Bt_2cAMP /Glucagon causes AQP8 localized at the pericanalicur vesicles to translocate to the cellular membrane, thus enhancing the number of water channels. This phenomenon is verified through two experiments – confocal immunofluorescence microscopy and cell shrinkage analysis. The immunofluorescence results showed significant increase in the AQP8s on the cell membrane of the treated cells and the cell shrinkage analysis showed significant enhancement in the water permeability of the treated cells compared to the controls. Furthermore, freshly isolated rat hepatocytes were treated with Bt_2cAMP, Glucagon and cryopreserved using standard

protocols in a controlled rate freezer. This resulted in a significant increase in the cell viability on warming. Conversely, the hepatocytes treated with mercuric chloride ($HgCl_2$) – a water channel inhibitor, had very low post-thaw viability. These results indicate that hepatocytes treated with Bt_2cAMP and glucagon causes increase of AQPs in the cellular membranes, prevents osmotic cell damages during cryopreservation and thus increases post-thaw viability. The results also suggest that such an increase in localization of AQPs on cellular membrane can also aid in improving the efficiency of cryopreservation of liver tissues and liver slices.

4.2 Introduction

In the cryopreservation of liver cells, tissue or slice, intracellular ice formation (IIF) is regarded as one of the major reasons for cell death [137, 138]. During the freezing process, an osmotic gradient develops between the intracellular and extracellular regions, resulting in permeation of water through the cellular membrane. With gradual increase in osmotic gradient over time, if water permeability of the cell membrane is limited, the resulting osmotic pressure causes the formation of intracellular ice. Hence, to avoid IIF, regulation of water transport across the cellular membrane is critical [120, 139].

Water movement across the cellular membrane has been known to be facilitated by aqueous pores and by direct permeation across the lipid bilayer [73]. However, recent discoveries have indicated the presence of water channels, known as aquaporins, a family of integral membrane proteins that facilitates osmotic movement of water across the cell membrane [74]. Of the 13 isoforms discovered so far, five of them were identified to be expressed in hepatocytes: AQP0, AQP8, AQP9, AQP11 and AQP12 [140-145].

Among these, AQP8s are localized in the plasma membrane [146], intracellular vesicles and the mitochondria. Prior experimental evidence shows that AQP8 has a tendency to translocate to the cellular membrane on the influence of choleretic stimulus [77, 80]. Therefore, increasing presence of AQPs on the cellular membrane by translocation of AQP8 from the intracellular vesicles can help increase the water permeation rate – thereby improve the cryopreservation success of liver tissues and slices.

Thus, in this chapter, the increase of AQPs by treatment with DiButyly cAMP (Bt_2cAMP) and glucagon and its effect on the post-thaw viability of the rat primary hepatocytes, i.e. the cryopreservation success are evaluated and discussed.

4.3 Materials and Methods

4.3.1 Isolation, Culture and Treatment of Hepatocytes

4.3.1.1Hepatocyte isolation

Sprague-Dawley male rats weighing 150-280 g were fasted 24 hours prior to isolation[§] and hepatocytes were isolated by collagenase perfusion method [126]. In brief, the rat liver was perfused with collagenase solution for approximately 10 minutes. The hepatocytes from the digested liver were isolated by mechanical disruption and filtering through a nylon mesh (105μm). The hepatocytes were then separated from the nonparenchymal cell fractions by centrifugation (Thermo IEC CEntra-CL3R, Thermo Scientific, MA) at 50 x g for 3 minutes. The viability of the centrifuged hepatocytes was evaluated immediately using trypan blue exclusion assay (Sigma-Aldrich, St. Louis, MO). If the resulting viability was smaller than 90%, percoll (GE healthcare, Waukesha, WI) centrifugation was performed to achieve a minimum of 90% viability for cell culture. Then the hepatocytes were re-suspended in the culture media containing DMEM

iv. [§]The isolation of liver from rats was performed by Dr. Charles Lee from UNC, Charlotte.

(Invitrogen, Gaithersburg, MD), sodium bicarbonate (3.7g/L), insulin (500 U/L), epidermal growth factor (20 µg/L), hydrocortisone (7.5 mg/L), 1% (v/v) of antibiotic/antimycotic solution (JR Scientific, Woodland, CA) and 10% (v/v) fetal bovine serum (HyClone, Thermo Scientific, Waltham, MA).

4.3.1.2 Culture of hepatocytes

Collagen type I gel based single gel culture of hepatocytes in tissue culture plates of 35 mm diameters were used for most of the experiments. The collagen gel was first prepared by adding 8 parts of 1.1 mg/mL PureCol collagen (Advanced BioMatrix, San Diego, CA) to 1 part of 10X DMEM solution. The pH was adjusted to 7.4 with 0.1N HCl and/or 0.1N NaOH. 0.5 mL of the prepared collagen was then coated on the 35 mm diameter tissue culture plates and incubated for an hour at $37^{o}C$, 5% $C0_2$ for gelation. Then 2 X 10^6 cells were seeded in each tissue culture plate, 1 ml of media was added and incubated at $37^{o}C$, 5% $C0_2$. The media was changed after 3 hours to remove the unattached cells and again incubated for another 24 hours.

4.3.1.3 Treatment of the hepatocytes

After 24 hours of incubation, hepatocytes were treated with a) 100 µM DiButyly cAMP (Bt_2cAMP) (Sigma-Aldrich, St. Louis, MO) or b) 1 µM glucagon (Sigma-Aldrich, St. Louis, MO) and incubated for 12 hours. For the controls, 1 mL of normal DMEM media was added to the culture plates and incubated for the same period as the treated ones. After 12 hours of incubation, a fraction of the treated and control culture plates were treated with 0.1 mM $HgCl_2$ – a water channel inhibitor for 5 min.

4.3.2 Evaluation of the Relocation of Aquaporins

4.3.2.1 Confocal immunofluorescence

For the confocal immunofluorescence experiments, collagen coated chamber slides were used instead of the tissue culture plates. Five hundred thousand isolated hepatocytes were plated on the collagen-coated chamber slides, and incubated at 37°C for 4 hours. The cells were then treated with a) 100 µM Bt_2cAMP in media, b) 1 µM glucagon in media and c) normal DMEM media (controls) and incubated for 12 hours. After the 12 hours of treatment, the hepatocytes were fixed with 2% formaldehyde for 10 minutes at room temperature and permeabilized with 0.2% Triton X-100 for 2 minutes. The cells were then treated with a blocking solution containing 3% BSA at room temperature and incubated overnight at 4°C with goat affinity-purified AQP8 antibodies (1:50, Santa Cruz Biotechnology Inc., Santa Cruz, CA). Then, the chamber slides were rinsed with PBS solution and treated with Alexa Flour 488 – conjugated donkey anti-goat HRP secondary antibody (Invitrogen, CA) for 1 hour. The dilution of the secondary antibody used was 1:400 in PBS. Then the cells were treated with 1 µg/mL concentration of Hoechst 33342 (Molecular Probes, Eugene, OR) and mounted with Pro- Long (Molecular Probes, Eugene, OR), an anti-fade reagents that suppress photobleaching and preserve the signals of the fluorescently labeled cells. Fluorescence localization of the AQP8 was then detected by immersion oil confocal microscopy with 100X magnification lens.

4.3.2.2 Cell shrinkage analysis

The cell shrinkage analysis was performed on treated and control samples prepared on the tissue culture plates as described in Section 4.3.1.2. Culture plates were

singly transferred to an Olympus IX70 microscope (Olympus America Inc, PA) mounted with a computer interfaced camera (Hamamatsu Corporation, Bridgewater, NJ). The media from culture plate was aspirated and 1 mL of 5M NaCl solution was added. The response of the cells to the hypertonic NaCl solution was captured at 40X magnification for every one minute interval – up to 20 minutes. The process was repeated one by one for the various treated and control samples. On completion of the process, the images were processed using software MetaMorph Imaging System (Molecular Devices, Sunnyvale, CA). Using MetaMorph, the variations of the cross-sectional area of the cells at various sites were measured over time to analyze the shrinkage behavior of the cells in the hypertonic solution.

4.3.2.3 Realtime polymerase chain reaction experiment[**].

Realtime PCR experiments were performed to verify whether the increase of AQPs in the cellular membranes was due to translocation of AQP8 or if new AQPs transcription occurred in the cells in response to the choleretic stimuli. Total RNA was isolated from the treated and control samples by TRIzol (Invitrogen, CA), DNase treatment and reverse transcription with Superscript III (Invitrogen, CA) were achieved according to the manufacturer's directions. The primers used for detection of AQP8 were "tcattgctaccttggggaac" and "gctcctgctcctggactatg" and for AQP9 were "tcgtctttgccatgtttgac" and "ccaatcataggacccacgac". Reverse transcriptase PCR (RT-PCR) was performed using these at 92^{o}C - 30s; 58^{o}C - 30s; 72^{o}C - 30s for a maximum of 35 cycles. PCR products were visualized on ethidium bromide gels and sequences verified. All experiments were performed in triplicate. RealTime PCR was run at 94^{o}C for 15 s;

v. [**] The RT-PCR experiments were conducted by Dr. Ashley Lakner from Carolinas Medical Centre, Charlotte, NC.

58^{o}C for 25 s; 72^{o}C for 20 s, read 5s. For RealTime PCR, the reaction mixture consisted of cDNA, forward and reverse primers (each 1 μL) at 5 nmol/L, 2 μl DEPC water, and 5 μL of SYBR Green Master Mix (Qiagen, Valencia, CA). The delta delta Ct method was used for quantification [147] and expression normalized to GAPDH, the housekeeping gene [148].

4.3.3 Cryopreservation of Treated and Control Samples

After the 12 hour treatment of the cell cultures was completed (Section 4.3.1.3), the treated and control samples were removed from the incubator and placed on ice. This was to reduce the temperature of the samples to 4^{o}C so that the samples were minimally affected by the addition of the CPA solution. In this investigation, two different CPA solutions – 20% Dimethyl sulfoxide in DMEM media and 20% glycerol in DMEM media were used. One milliliter of the cryoprotectant solution was added to the samples and incubated at 4^{o}C for 10 minutes so as to reach equilibrium. Then the samples placed in cryobags and they were transferred to the CryoMed Control Rate freezer (Thermo Forma, Waltham, MA), shown in Fig 4.1.

FIGURE 4.1: Equipment used for the controlled freezing of the samples. Shows the CryoMed Control Rate Freezer connected to the liquid nitrogen tank and the computer used to program and operate the freezer.

The control rate freezer was programmed to freeze the samples according to the freezing protocol indicated by Fig 4.2. The controlled cooling process was initiated at 4^{o}C and a cooling rate of 1^{o}C/min was maintained for 20 minutes, i.e., until -16^{o}C is reached. Then a cooling rate of 2^{o}C/min was maintained until -36^{o}C/min, and thereafter a cooling rate of 10^{o}C/min until a temperature of -80^{o}C was achieved. The samples were further maintained at -80^{o}C for 5 minutes to ensure equilibrium. At the end of the freezing process, the samples were transferred immediately to a -80^{o}C Revco freezer (Kendro Laboratory, Ashville, NC) and stored for a week.

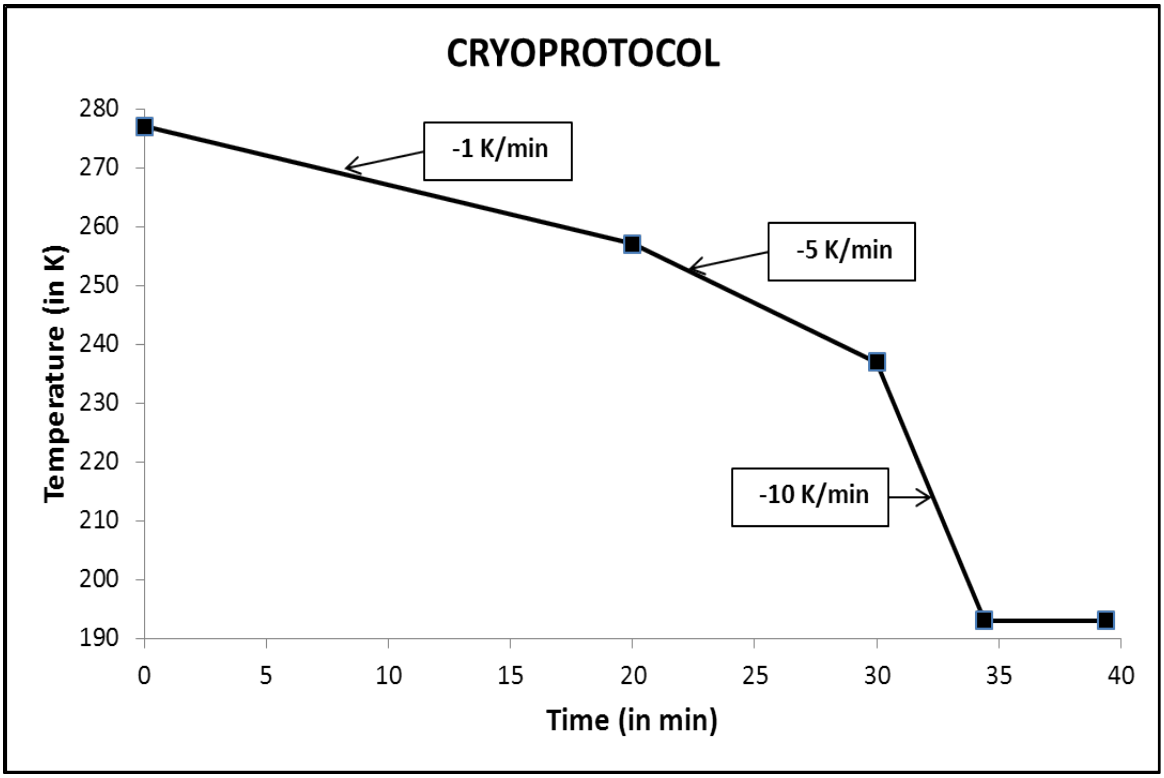

FIGURE 4.2: Cryoprotocol used in the control rate freezer for the freezing of the cell culture samples.

4.3.4 Evaluation of Post-thaw Cell Viability

The cryopreserved samples from the -80^{o}C freeze were transferred to a sterile glass box and plated in a water bath maintained at 37^{o}C, until the media in the frozen samples completely melted. At this juncture, the samples were approximately 5-10^{o}C and not at 37^{o}C. Immediately, the CPA containing media in the samples was aspirated to limit toxicity to the cells. Then, 1 mL of cell culture DMEM media was added to the samples and incubated at 37^{o}C for 10 minutes. After 10 minutes of incubation, the media in the samples was again refreshed in order to remove any remaining traces of CPA. These samples were then placed in the incubator at 37^{o}C, 5% CO_2 for 24 hours and allowed to recuperate from the freeze-thaw process.

After 24 hours of recuperation time, cell viability of the samples was determined using nucleic fluorescence dyes. The samples were washed with 1X PBS solution and incubated with 1 µg/mL concentration of Hoechst and 2 µM Ethidium Homodimer (Molecular Probes, Eugene, OR) in PBS for 30 minutes. Then the viability solution was aspirated and the samples were fixed by adding 1mL of 10% formalin (VWR, West Chester, PA) and incubating for 20 minutes. Later, the cell viability was examined through a confocal microscope with DAPI (excitation 358nm; emission 461nm) and Texas red (excitation 596nm; emission 620nm) filters. The fluorescent images obtained were then analyzed using MetaMorph Imaging System.

4.3.5 Statistical Analysis

One-way Analysis of Variance (ANOVA) was performed to determine the significant differences for all the data analyses. All the analyses were considered a two tailed test with the type I error, α as 5%. Most of the experiments were performed for doublet samples (in some case triplicates) and each experiment was repeated for a minimum of three rats.

4.4 Results

4.4.1 Confocal immunofluorescence

The confocal immunofluorescence microscopy images were captured at 100X magnification. Fig 4.3 shows the Alex Fluor 488 labeling of AQP8 for cultured hepatocytes treated for 12 hours with a) no choleretic stimuli (control), b) 100 µM Bt_2cAMP and c) 1 µM glucagon, for cells from three different rats. The blue color in the images represents the nuclei of the cells stained by the Hoechst dye. For the controls, the distribution of AQP8 is fairly even throughout the cytosol and the plasma membrane,

indicating AQP8 localization in the vesicles as well as the cellular membrane. In contrast, the images for the cells treated with Bt_2cAMP or glucagon show a higher density of AQP8 labeling along the cellular membrane. This verifies the translocation of AQP8 from the vesicle to the cellular membrane due to the effect of the treatments.

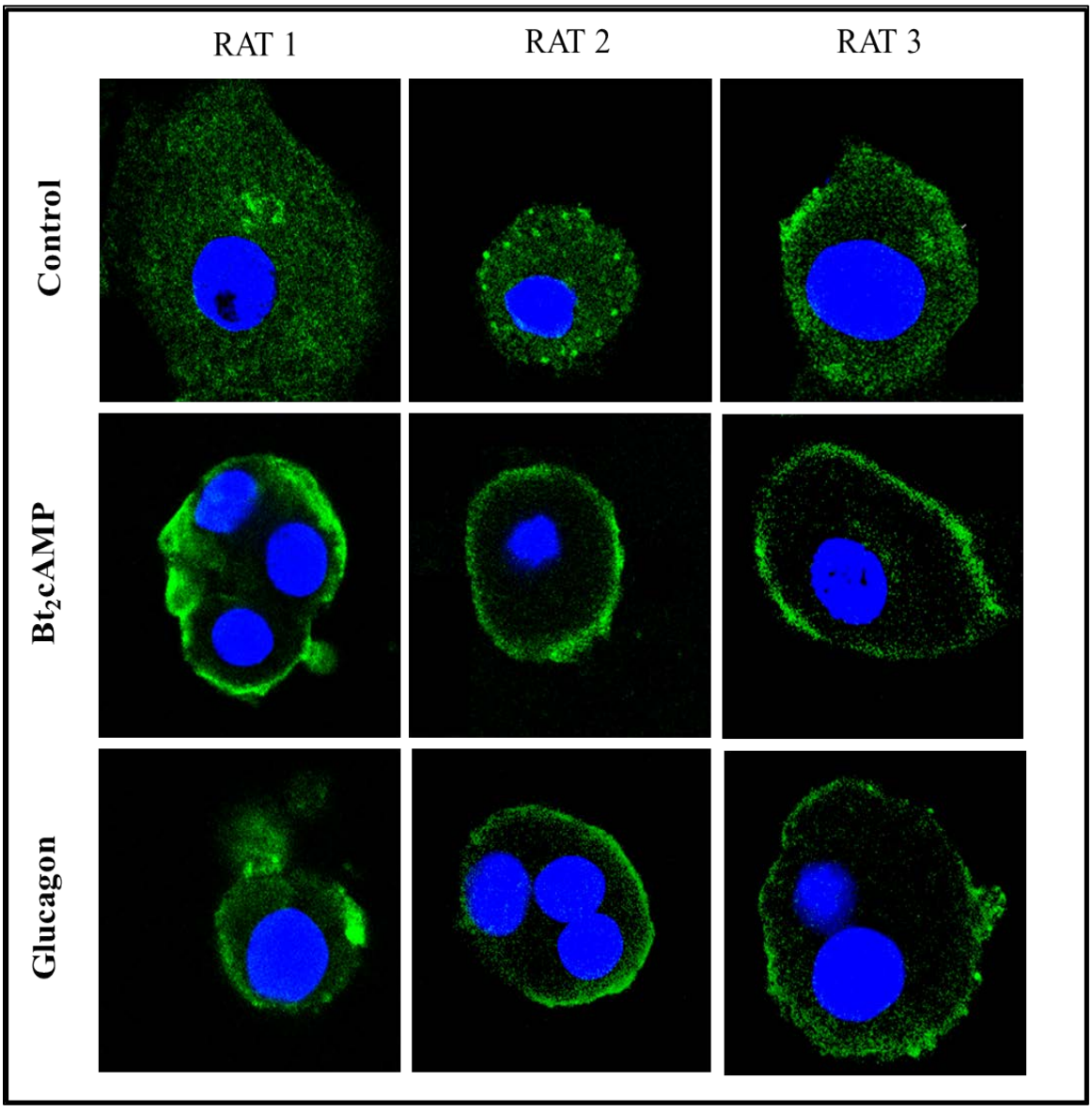

FIGURE 4.3: Localization of AQP8 in hepatocytes by confocal immunofluorescence microscopy. It shows the fluorescent labeling (green) of AQP8 in the control cells and cells treated with 100 µM Bt_2cAMP and 1 µM glucagon for 12 hours. The blue region represents the nucleus of the cells stained by the Hoechst dye. Objective 100X, Zoom 1.5.

Also confocal immunofluorescence microscopy was performed for control samples incubated in the absence of the a) primary antibody, b) secondary antibody and c) both to check for any non-specific labeling. No such non-specific fluorescent labeling was detected, confirming the integrity of the results obtained.

4.4.2 Cell shrinkage analysis

In the cell shrinkage analysis, the treated and control cells were subjected to a hypertonic environment. It initiated an osmotic water transport across the cellular membrane, resulting in the shrinking of the cells over time. The cells were monitored using the microscope – camera arrangement, and the images were captured at regular intervals. Fig 4.4 shows an image captured at the initialization of the shrinkage process.

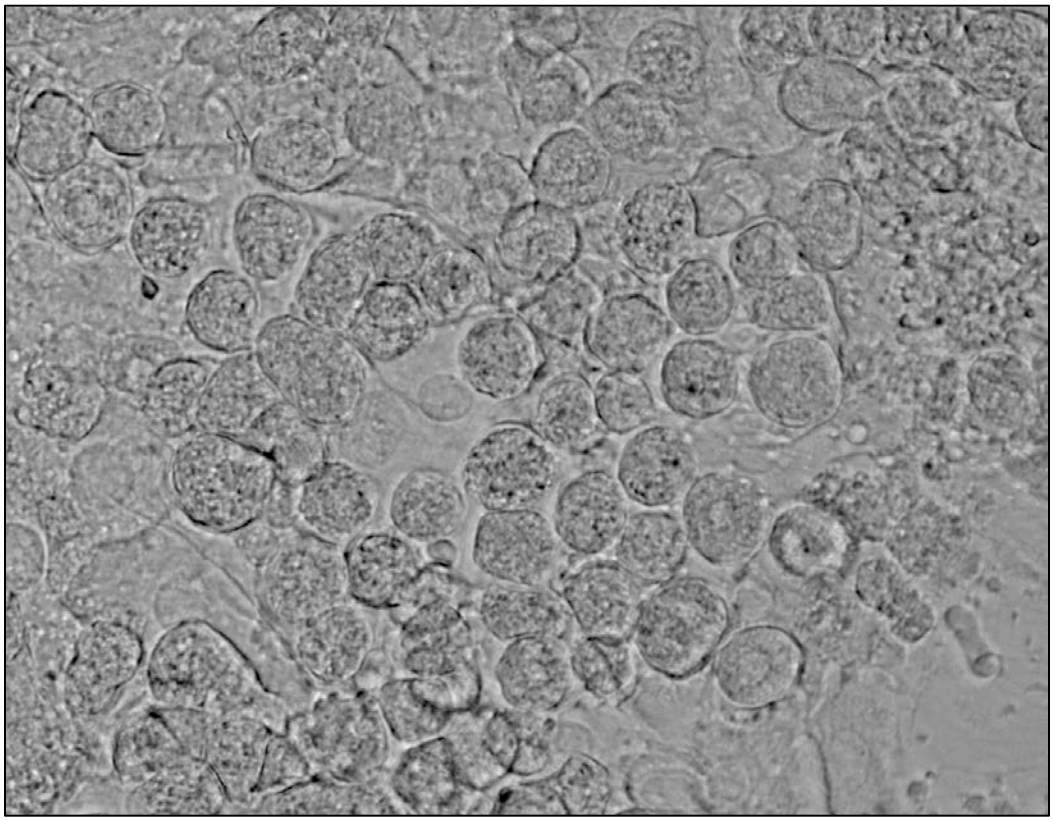

FIGURE 4.4: Sample of the morphology of the cells monitored during the cell shrinkage analysis. The image was captured with the cells in a hypertonic. Objective - 40X.

Analysis of images acquired over time for the various samples is collectively summarized in the graph shown in Fig 4.5. The cells treated with Bt_2cAMP or glucagon shows a significant decrease in their cross-sectional area over time as compared to the control cells. This indicates an increase in the osmotic water transport, thereby confirming the effects of the increase in the quantity of AQPs on the cellular membrane. Furthermore, the cells in the samples treated with $HgCl_2$, the water channel inhibitor, show no significant shrinkage behavior. It holds true even for the samples first treated with Bt_2cAMP and/or glucagon and then treated with $HgCl_2$. This is not shown in Fig 4.5 since their curves typically overlapped with the curve for the $HgCl_2$ treated cells. Thus the cell shrinkage analysis conclusively indicates that the water permeability of the cells treated with Bt_2cAMP/glucagon increase mainly due to increase in the water channels (AQPs) on the cellular membranes; and that those effects can be nullified by $HgCl_2$ treatment.

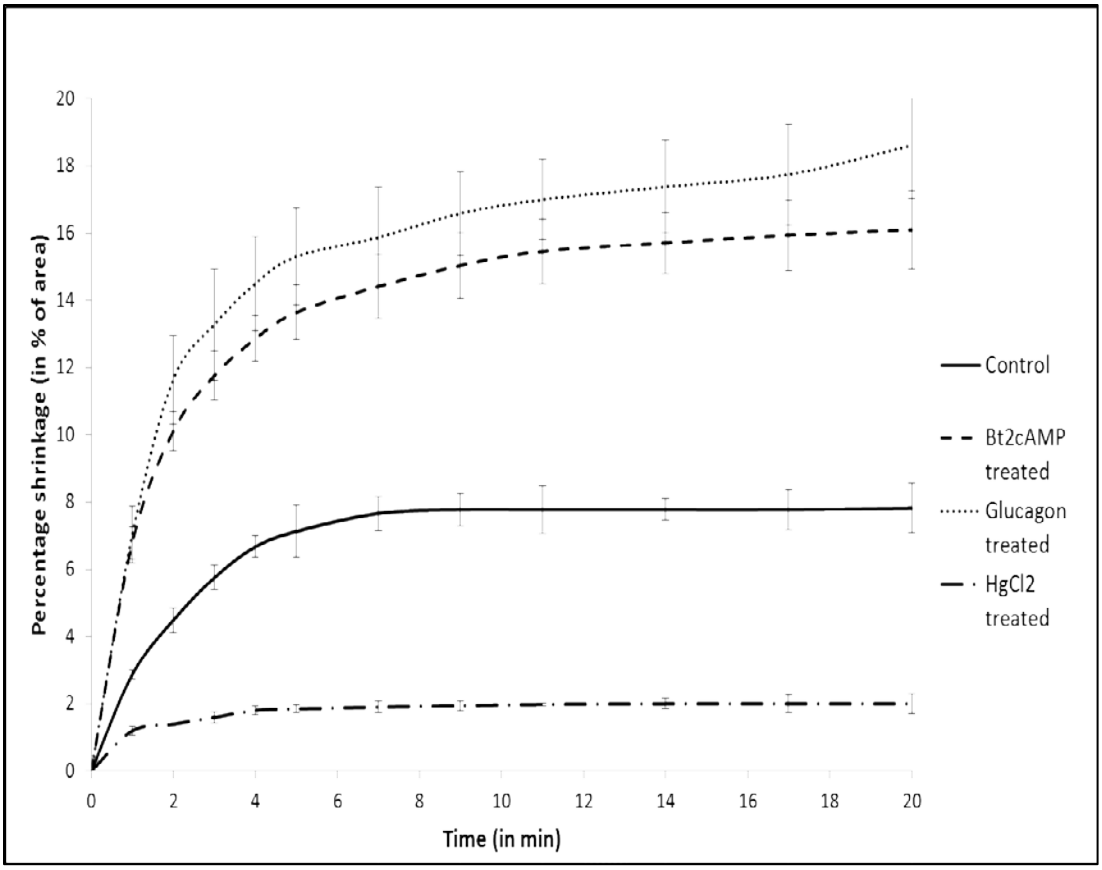

FIGURE 4.5: Cell shrinkage analysis results. The plot shows the percentage reduction in the cross sectional area of the treated and control cells over time under the influence of the hyperonic environment. n=5, Mean ± SE.

4.4.3 Real Time PCR Experiments

Realtime PCR experiments were next performed to analyze any variation in AQP8 and AQP9 mRNA expressions due to the treatments. The results from the experiments were inconclusive, as shown in Fig 4.6 and Fig 4.7. As shown in both figures, the standard errors for the experiments were too high, indicating a lack of repeatability of the reading. Hence, no significant conclusion could be made from the Realtime PCR experiments.

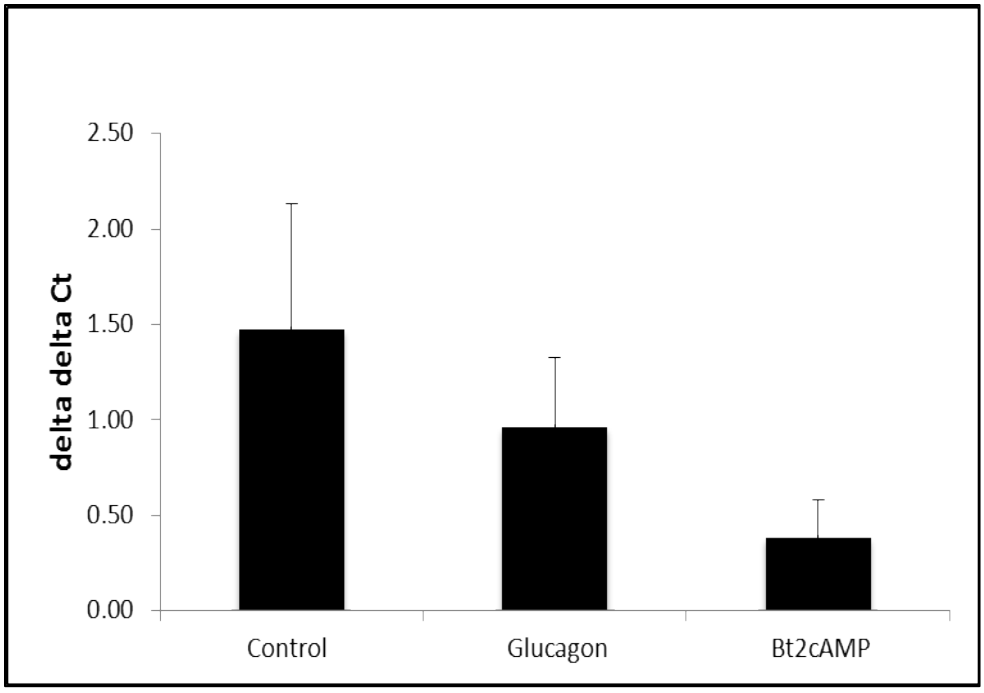

FIGURE 4.6: Realtime PCR results for AQP8 mRNA expression, n=5, Mean ± SE.

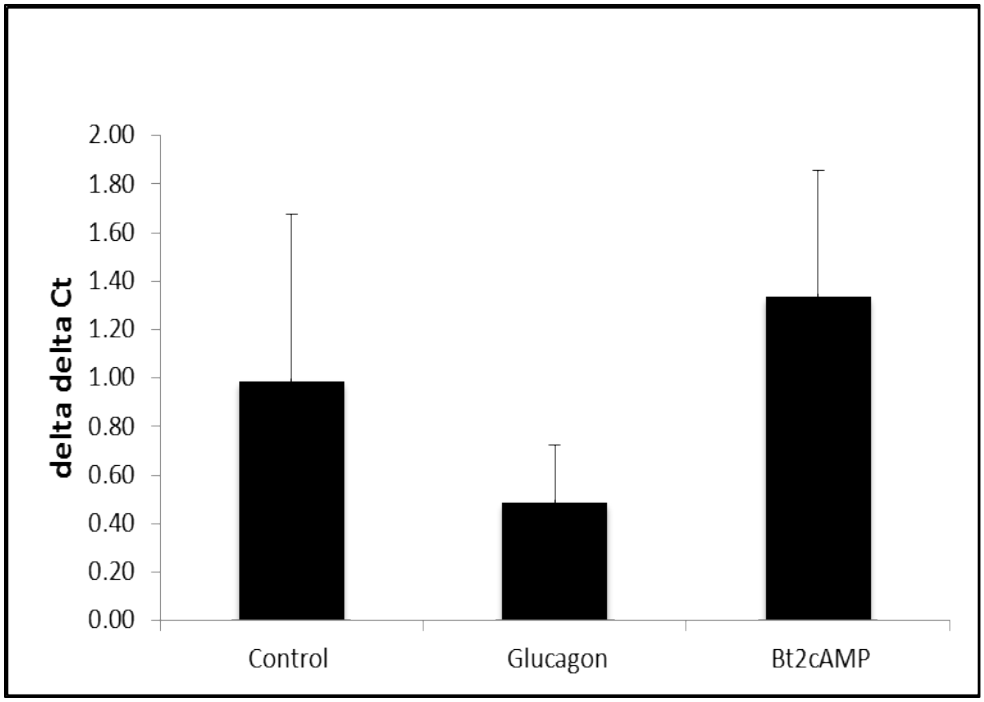

FIGURE 4.7: Realtime PCR results for AQP9 mRNA expression, n=3, Mean ± SE.

4.4.4 Effects of the Treatments on Cryopreservation Success

Controlled rate freezing of the treated and control samples, as indicated in Section 4.3.3, were carried out to cryopreserve the samples. The frozen samples were thawed after one week in the -80^{o}C freezer, allowed to recuperate for 24 hours in the incubator at 37^{o}C, 5% CO_2 and then their cell viability was evaluated. Images of the fluorescently stained samples were captured using confocal microscope with DAPI (reads Heochst stains – all cells) and Texas Red (reads Ethidium Homodimer stains – dead cells) filters. Examples of representative confocal images are shown in Fig 4.8.

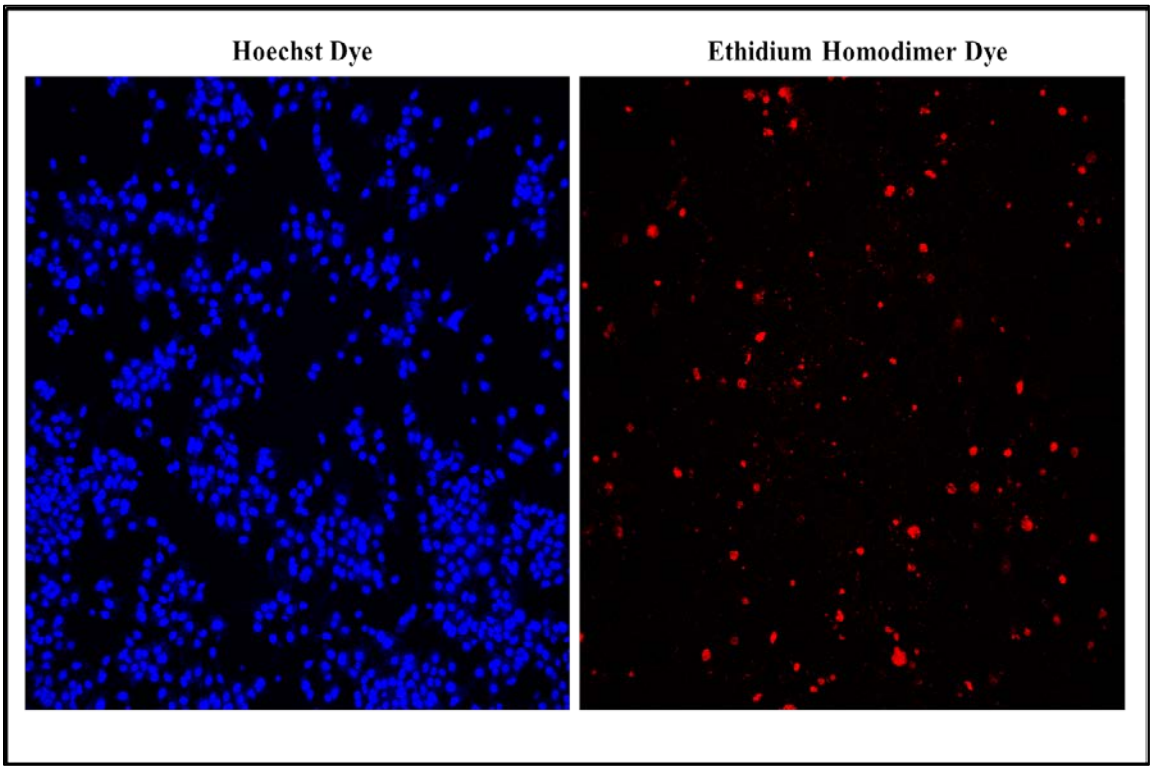

FIGURE 4.8: A Sample of the fluorescent stains of the hepatocytes obtained during the evaluation of the post-thaw cell viability. LEFT: Hoechst stains labeling the nucleus of all the cells in the field. RIGHT: Ethidium homodimer stains labeling the dead cells in the field. Objective – 10X.

For each sample, the confocal fluorescent images were captured for four randomly selected view fields. The images were then analyzed using MetaMorph Imaging System, which enabled a quantitative measurement of the viability in each field. The cell viability of each sample was then estimated from the cumulative cell viabilities of the four fields per sample. The comprehensive viability assessment for the treated and control culture samples are depicted in Fig 4.9 and Fig 4.10.

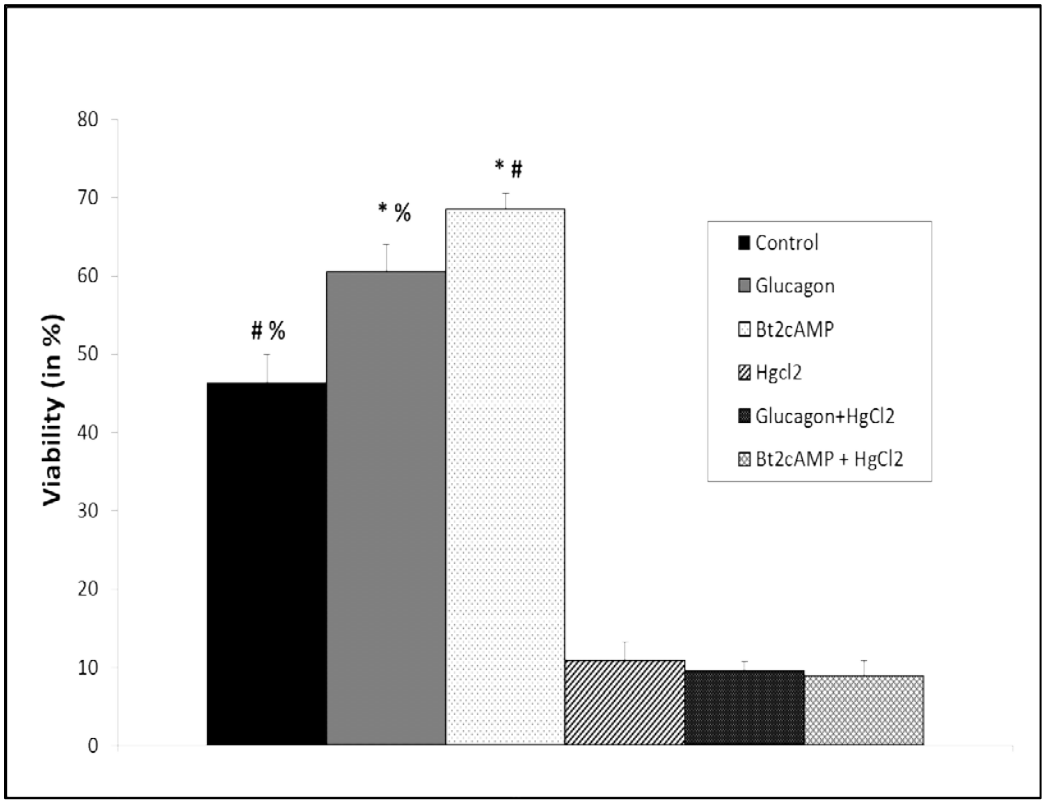

FIGURE 4.9: Post-thaw cell viabilities for treated and control samples with DMSO as the cryoprotective agent. n=4, * # %: $p<0.05$. Mean ± SE

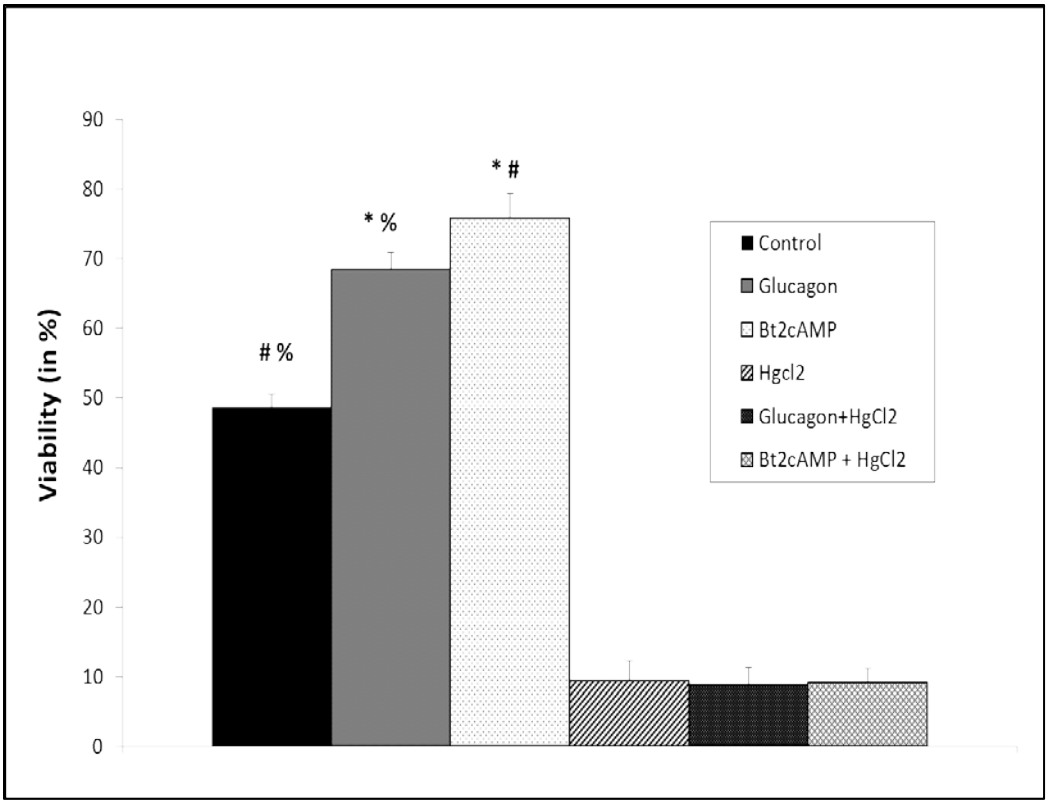

FIGURE 4.10: Post-thaw cell viabilities for treated and control samples with glycerol as the cryoprotective agent. n=4, * # %: $p<0.05$. Mean ± SE

Fig 4.9 represents the post-thaw viability measurement for the samples cryopreserved with 20% DMSO in DMEM as the cryoprotective agent, whereas Fig 4.10 represents the samples cryopreserved with 20% glycerol in DMEM. Both the results show a similar trend, in the sense that the cell viability of the cultures treated with Bt_2cAMP and glucagon was significantly higher than the control. They also suggest that the translocation of the AQPs by treatment with Bt_2cAMP or glucagon improves water transport properties of the cells during cryopreservation, resulting in increased cell survival.

Likewise, in both cases (i.e., when either DMSO or glycerol are used as the CPA), the samples treated with the water channel inhibitor $HgCl_2$, showed significantly lower cell viability. This can be attributed to two reasons. Firstly, $HgCl_2$ blocks the water

channels and reduces the water permeation rate during the freezing process, thereby increasing the probability of IIF. Secondly, during the post-thaw process it was seen that some of the $HgCl_2$ particles settled down in the culture plates, which could prove to be toxic for the recuperating cells.

Furthermore, by comparing the results of Fig 4.9 and 4.10, the relative effects of CPA choice on post-thaw cell viability for these AQP translocation studies, can be ascertained. Fig 4.11 represents the comparison of the post-thaw cell viabilities between the use of DMSO and glycerol as CPA, with respect to different treatments. In the case of the cells treated with Bt_2cAMP or glucagon, a significant increase in the cell survival is observed with the use of glycerol as the CPA, whereas no such significance is seen for the other cases. This suggests that glycerol is a more preferred CPA than DMSO when there is an increased AQPs expression in the hepatocyte cellular membrane.

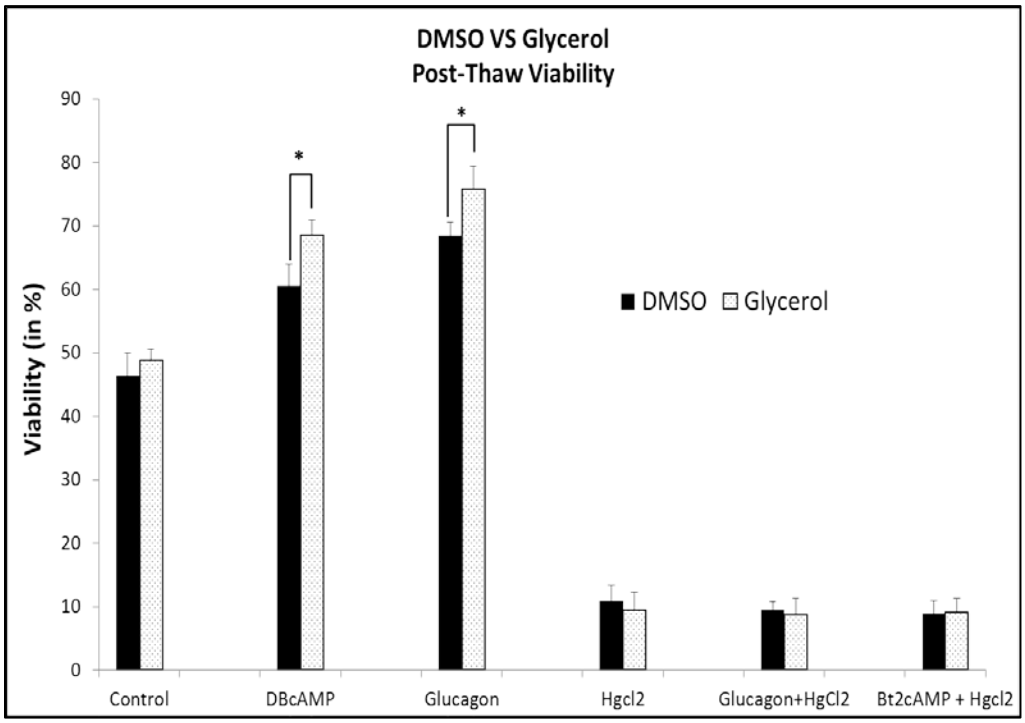

FIGURE 4.11: Post-thaw cell viability comparisons between use of DMSO and glycerol as CPA with respect to the different treatments. n=4, *: $p<0.05$. Mean ± SE

4.5 Discussions

In the current work, the hypothesis of increasing AQPs on hepatocyte cellular membrane by choleretic stimuli to improve the success of cryopreservation of liver tissue equivalent was investigated. Though similar studies have been performed for the successful cryopreservation of embryos, larvae, oocytes and kidney cells [69-72, 76], the role of AQPs in cryopreservation of hepatocytes has not been investigated yet. In the cases of embryos, larvae, oocyte and kidney, AQPs were artificially expressed on the cellular membrane prior to cryopreservation. Contrastingly, in the current investigation, the fact that AQPs can be increased in the cellular membrane by the translocation of AQP8 from the intracellular vesicles under the influence of choleretic stimuli such as DiButyly cAMP (Bt2cAMP) [80] and glucagon [77, 146, 149], was utilized. As such, it was verified by the confocal immunofluorescence which showed increased AQP8 localization at the cellular boundaries on treatment with Bt_2cAMP or glucagon (Fig 4.3).

With increase in the quantity of AQPs on the cellular membrane, it was expected that the water transport properties of the cells also should improve. This was verified by the cell shrinkage analysis, wherein the hepatocytes cultured in a collagen gel matrix were subjected to a hypertonic environment and their shrinking behavior was monitored over time. Such an analysis differs from the traditional swell-shrink analysis in which the swell – shrink behavior of individual cells are monitored in suspension [150] or flow [151] rather than in a collagen matrix. In the case of hepatocytes embedded in an ECM, the shrinkage of the cells is considerably restricted by its attachment to the ECM and the cell-cell interactions. Despite such restrictions, a significant increase in the cell shrink was observed by treatment of the cells with Bt_2cAMP and/or glucagon. This suggests that

such treatments can potentially improve water transport in liver tissues, slices and even in whole liver.

Furthermore, attempts were made to determine if the increase in the water transport properties of the cells were purely due to the translocation of AQP8 to the cellular membrane or if new AQPs were transcribed by the treatments. However, the results from the Realtime PCR turned out to be unsatisfactory to draw any clear conclusion. A major concern was the presence of the ECM which would retain some of the urea secreted by the cells. The urea mixes up with TRIzol during the lysing process and affects the RT-PCR results [152]. So the spin method for protein and RNA isolation as suggested by Heidebrecht et al [152] was tried but it did not prove to be helpful. However, prior research works [80, 140, 146] have successful checked for transcription (by RT-PCR technique) and translation (by immunoblotting technique) of AQPs due to Bt_2cAMP or glucagon treatments of isolated hepatocytes plated on collagen coated cover slips. The results indicated that neither transcription nor translation of AQPs occurs in hepatocyte treatment with Bt_2cAMP or glucagon. Hence, it was safe to consider that the increase in the water permeability of the cellular membrane was primarily due to relocation of the AQP8s.

On establishing the method of treatments and verifying the relocation of the AQPs, cryopreservation of treated and control culture samples were performed. The samples were thawed after one week, allowed to recuperate for 24 hours and then their post-thaw viability was estimated. It is to be noted that the post-thaw cell viability reported in this chapter is the ratio of the estimated number of live cells to the estimated total number of cells in the culture plates after fixing the cells with 10% formalin. This does not represent

the actual cell viability with respect to the 2 X 10^6 cells seeded at the initiation of the culture process because some of the dead cells would have detached and been washed off during the process of changing media, removing cryoprotective media, and the washing steps. In fact, it was estimated that roughly 1.4 – 1.7 X 10^6 cells remained attached to the culture plate at the end of the fixing step. So the reported cell viability might be slightly higher than the actual cell viability. However, this factor is not critical in the current investigation since this is a comparative investigation between the treated versus control samples and also treated and controls samples were all subjected to the same experimental processes.

The results from the post-thaw viability shown in Fig 4.9 and 4.10 confirmed the hypothesis that the increased AQP expression on the cellular membrane significantly improves the cryopreservation success. In addition, most of the culture samples treated with Bt_2cAMP exhibited higher cell viability compared to the ones treated with glucagon. One possible argument for it is that the 12 hours of treatment of cells with glucagon might not be sufficient for maximum relocation of the AQP8s. Literature suggests that the longer the cells are treated with glucagon, the more number of AQP8 translocate to the cellular membrane. Results from Soria et al [146] suggested that treatment of hepatocytes with glucagon for 36 hours showed 120% increase in the quantity of AQP8 on cellular membrane as opposed to 80% increase for a 16 hours treatment. On contrary, for Bt_2cAMP, some researchers indicate 10 min incubation is enough for effective translocation of AQP8 [140] whereas others recommend 12 hours [80]. Therefore, there is a need for better understanding of the mechanism of AQP8 translocation and

optimization of the time scale of the treatments with Bt_2cAMP and glucagon – a future prospect in this field.

Also it was observed from the result (Fig 4.11), that the choice of the cryoprotective agent (CPA) for the cryopreservation may affect the cryopreservation outcome. In the current investigation, use of glycerol as CPA showed significantly higher post-thaw cell viability compared to DMSO. A few probable explanations can be provided for preference of glycerol over DMSO. Firstly, DMSO has been identified as a water channel blocker [80, 153]. So, use of DMSO as CPA might in fact retard the water transport through the AQP water channels to some extent, thus exhibiting lower post-thaw viability. Secondly, AQP9 are known as aquaglyceropins, which facilitates the transport of glycerol across the cellular membrane [77, 78]. As a result, it might aid in better protection of hepatocytes from freeze injuries. However, the exact mechanism of how cryoprotectants protect the cells from freeze injury during freezing is yet unknown.

Overall, the current investigation was able to successfully confirm the hypothesis that translocation of AQPs in hepatocytes can indeed help improve its cryopreservation success. Furthermore, glycerol was identified as a preferred CPA for safe storage of hepatocytes with enhanced AQP localization of the cellular membrane. Also the results from the current work provide scope for a number of future research works. Some of those are 1) to analyze the effect of the translocation of AQPs on the post-thaw functional behavior of the cryopreserved hepatocytes, 2) to optimize the time scale of the Bt_2cAMP and glucagon treatment 3) to explore and identify other ways of over expressing AQPs on the hepatocyte cellular membrane (e.g., Viral vector expression via DNA cloning) and

4) to verify the effectiveness of this strategy in successful cryopreservation of large liver tissues, slices and even the whole livers.

CHAPTER 5: CONCLUSION

The focus of this dissertation was to enhance bioreactors' performance and application. Computational and experimental analyses were performed to address two main mass transport issues influencing the effective use of bioreactors for clinical use. From these analyses, the mechanism of oxygen transport during the operation of bioreactors and the mechanism of water transport during cryopreservation of cells/tissues used in bioreactors were better understood. As a result, effective computational and experimental strategies have been proposed as a step towards solving the mass transport issues with respect to bioreactors.

In Chapter 2, the problem of cells/tissues in bioreactors not receiving adequate levels of oxygen was investigated. A CFD based computational model was developed to analyze the oxygen transport behavior within the bioreactor. The model was used to predict and visualize the oxygen distribution within a cell space for various experimental conditions. It enabled identification of some of the critical factors that affect the oxygen distribution in the relevant cell space. With such capabilities, the CFD model can be effective in design optimization and development of new and improved bioreactors.

Chapter 3 addressed the issue of inadequate off-the-shelf availability of cells/tissues for use in bioreactors. More specifically, it provides a user friendly computational model (MMT) to help improve cryopreservation techniques for safe storage of tissues. The MMT was developed to predict the probability of ice formation during freezing of tissues by analyzing the thermal history it experienced and its

corresponding cellular water transport behaviors, for prescribed cryoprotocols. Thus, the model would enable comparison and optimization of cryoprotocols for effective storage of tissues at low temperature.

Chapter 4 focused specifically on improving the cryopreservation success of liver tissue equivalents. A strategy of improving the cellular water transport of hepatocytes during freezing by increasing the quantity of AQPs (water channel proteins) on the cellular membrane was hypothesized and experimentally tested. Experimental results showed a qualitative increase in the AQP localization on the hepatocyte cellular membrane and increased cellular water transport by treatments with choleretic stimuli. Such treatments also resulted in improved post thaw viability of hepatocytes - confirming the hypothesis. Thus, the strategy of increasing AQP expressions on the cellular membrane for cryopreservation successful might potentially pave way for more effective techniques to safely freeze the whole liver.

5.1 Future Research

This dissertation introduced a few effective methods for improving mass transport and cryopreservation of biological tissues. Among these, two computational models have been proposed. Computational models are usually developed based a number of assumptions, simplifications and approximations, so they always have scope for improvements. The CFD model discussed in Chapter 2 can be improved by modeling for uneven distribution of cells in the cell space, implementing Michaelis -Menten reaction, and turbulent media flow.

With regard to the MMT discussed it Chapter 3, the model was developed for simple geometries. The model needs to be extended to simulate various complex

geometries for more practical implementation. Also the model's predictions are highly dependent of the system specific biophysical parameters. These biophysical parameters have not been well characterized yet and hence there is a need for better methodologies for analyzing these parameters.

Chapter 4 describes the effectiveness of increasing AQPs in hepatocyte cellular membrane on its cryopreservation. However, future work is necessary to establish its effectiveness on post-thaw functionality of cells and its application to liver slices or even whole liver. In addition, since liver slices and whole liver are made up of different cell types, it would be necessary to analyze the effect of the treatments on cryopreservation of co-cultures of different liver cell types such as hepatocytes, Kupffer cells, hepatic stellate cells, etc. New methods and techniques for over expressing AQPs on the cellular membrane on hepatocytes can also be explored.

Overall, the current dissertation provides few heat and mass transport based strategies to enhance the effectiveness of bioreactors in industrial and clinical use. The computational and experimental strategies proposed would potentially aid in development of effective bioreactors and efficient cryoprotocols to support off-the shelf availability of cells for bioreactors.

REFERENCES

1. Langer R, Vacanti JP, 1993, Tissue engineering, Science 260:920–926.
2. MacArthur BD, Oreffo RO, 2005, Bridging the gap, Nature, 433 (7021): 19.
3. Mazariegos GV et al, 2002, First clinical use of a novel bioartificial liver support system (BLSS). Am. J. Transplant. 2: 260–266.
4. Nyberg SL et al, 1993, Evolution of the bioartifical liver - The need for randomized clinical trials. The American Journal of Surgery. 166(5): 512-521.
5. Borrai M et al, 2002, Advanced technology for extracorporeal liver support system devices. Intl J Art. Organs. 25(10): 939-949.
6. Park Y, Iwata H, Satoh S, Uesugi H, Ryu H, 2003, Method for evaluating metabolic functions of drugs in bioartificial liver, Biotech and Biopros Engg, 8(5): 279-285.
7. Iwahori T et al, 2003, CYP3A4 inducible model for in vitro analysis of human drug metabolism using a bioartificial liver, Hepatology, 37(3): 665-673.
8. Martin I, Wendt D, Heberer M, 2004, The role of bioreactors in tissue engineering. Trends in Biotech 22(2):80-86.
9. Powers MJ et al, 2001, A microfabricated array bioreactor for perfused 3D liver culture, Biotech and Bioengg. 78(3)\: 257-269.
10. Chromiak JA, Shansky J, Perrone C, Vandenburgh HH, 1998, Bioreactor perfusion system for the long-term maintenance of tissue-engineered skeletal muscle organoids, In vitro Cell. Dev. Biol – Animal, 34: 694-703.
11. Strain A, Neuberger J, 2002, A bioartificial liver--state of the art, Science 295 (5557): 1005–9.
12. Hongo T et al, 2005, Three-dimensional high-density culture of HepG2 cells in a 5-ml radial-flow bioreactor for construction of artificial liver. J Biosci Bioeng, 2005. 99(3): 237-44.
13. Zeilinger K, et al., 200, Liver cell culture in bioreactors for in vitro drug studies as an alternative to animal testing, ALTEX, 17 (1): 3-10.
14. Miranda JP, et al., 2010, Extending hepatocyte functionality for drug-testing applications using high-viscosity alginate-encapsulated three-dimensional cultures in bioreactors, Tissue Eng Part C, 16 (6): 1223-32.
15. Bravo D et al, 2000, Effect of storage and preservation methods on viability in transplantable human skin allografts. Burns 26: 367–378.
16. Rieke M, Gotwald E, Weibezahn K, Layer P, 2008, Tissue reconstruction in 3D-spheroids from rodent retina in a motion-free, bioreactor-based microstructure , Lab Chip, 8: 2206-2213.

17. Oegema TR et al, 2000, A simple cryopreservation method for the maintenance of cell viability and mechanical integrity of a cultured cartilage analog. Cryobiology 40: 370–375.

18. Allen JW, Hassanein T, Bhatia SN, 2000, Advances in bioartificial liver devices, Hepatology. 34(3)\: 447\-455.

19. Radisic M et al, 2006, Biomimetic approach to cardiac tissue engineering: O2 carriers and channeled scaffolds. Tissue Engg, 12: 2077-91.

20. Groot HD, Noll T, 1987, Oxygen gradients: The problem of hypoxia. Biochem Soc Trans. 15(6): 363-365.

21. Groot HD, Littauer A, 1989, Hypoxia, reactive oxygen and cell injury. Free Radic Biol Med. 6: 541-551.

22. Malda J, Klein TJ, Upton Z, 2007, The roles of hypoxia in the In vitro engineering of tissues. Tissue Engg. 13(9): 2153-2162.

23. Barazzone C, White CW, 2000, Mechanisms of cell injury and death in hyperoxia. Am J Respir Cell Mol Biol. 22: 517-519.

24. Parinandi NL, Kleinberg MA, Usatyuk PV, 2003, Hyperoxia-induced NAD(P)H oxidase activation and regulation by MAP kinases in human lung endothelial cells. Am J Physiol Lung CellMol Physiol. 284: L26-L38.

25. Bilodeau K, Mantovani D, 2006.Bioreactors for tissue engineering: Focus on mechanical constraints. A comparative review. Tissue Engg. 12(8): 2367-2383.

26. Hay PD et al, 2000, O2 transfer in diffusion-limited hollow fiber bio-artificial liver. Artifical Organs. 24(4): 278-288.

27. Hay PD, Veitch AR, Gaylor JDS, 2001, Oxygen transfer in a convection-enhanced hollow fiber bioartificial liver. Artifical Organs. 25(2): 119-130.

28. Brown DA et al, 2007, Analysis of oxygen transport in a diffusion-limited model of engineered heart tissue. Biotech and BioEngg. 97(4): 962-975.

29. Ju LK, Sundararajan A, 1995, The effects of cells on oxygen transfer in bioreactors. Biopros and Biosys Engg. 13(5): 271-278.

30. Nui M, Hammond P, Coger RN, 2009, The effectiveness of a novel cartridge-based bioreactor design in supporting liver cells. Tissue Engg. 15(10): 2903-2916.

31. Ju LK, Lee JF, Armiger WB, 1991, Enhancing oxygen transfer in bioreactors by perfluorocarbon emulsions, Biotech. Prog. 7(4): 323-329.

32. Tilles AW et al, 2000, Internal membrane O_2ation removes substrate O_2 limitations in a small-scale flat-plate hepatocytes bioreactor. International symposium on tissue Engg for therapeutic use 5.

33. Flendrig LM et al, 1997, In vitro valuation of a novel bioreactor based on an integral O2ator and a spirally wound nonwoven polyester matrix for hepatocyte culture as small aggregates. J Hepatology. 26: 1379-92.

34. Leung R, Poncelet D, Neufeld RJ, 1997, Enhancement of O2 transfer rate using microencapsulated silicone oils as O2 carriers. J Chem Tech Biotech. 68: 37-46.

35. Harrison BS et al, 2007, O_2 producing biomaterials for tissue regeneration. Biomat. 28: 4628-4634.

36. McClelland RE, Coger RN, 2000, Use of micropathways to improve O2 transport in a hepatic system. J Biomech Eng. 122(268): 268-273.

37. McClelland RE, Coger RN, 2004, Effects of enhanced O2 transport on hepatocytes packed within a bioartificial liver device. Tissue Engg. 10(1): 253-266.

38. McClelland RE, MacDonald JM, Coger RN, 2003, Modeling O2 transport within engineered hepatic devices. Biotech Bioengg. 82: 12-27.

39. Nui M, Clemens MG, Coger RN, 2008, Optimizing normoxic conditions in liver devices using enchanced gel matrices. Biotech Bioeng. 99: 1502-12.

40. Webster IA, Shuler ML, 1978, Mathematical models for hollow fiber enzyme reactors. Biotech Bioeng. 20: 1541-1556.

41. Smith MD, Cairns D, Gaylor JDS, Veitch AR, 1997, Analysis of O2 transfer in hollow fiber hepatocyte bioreactors. Artificial Organs. 21(6): 531.

42. Hutmacher DW, Singh H, 2008, Computational fluid dynamics for improved bioreactor design and 3D culture. Trends in Biotech. 26(4): 166-172.

43. Ledezma G et al, 1999, Numerical model of fluid flow and O2 transport in a radial-flow microchannel containing hepatocytes. J Biomech Engg. 121: 58-64.

44. Williams KA, Saini S, Wick TM, 2002, Computational fluid dynamics modeling of steady-state momentum and mass transport in a bioreactor for cartilage tissue engineering, Biotech. Prog. 18: 951-963.

45. Mazur P, 1970, Cryobiology- the freezing of biological systems, Science 168 (3934): 939–49.

46. Anchordoguy TJ, Rudolph A, Carpenter J, Crowe J, 1987, Modes of interaction of cryoprotectants with membrane phospholipids during freezing, Cryobiology, 24 (4): 342-331.

47. Bhat SN, Sharma A, Bhat SV, 2005, Vitrification and glass transition of water: insights from spin probe ESR, Phys Rev Lett, 95 (23): 235702

48. Coger R, Toner M, 1995, Preservation techniques for biomaterials, The biomat Handbook, 1557-1567.

49. Devireddy RV et al, 2002 Cryopreservation of equine sperm: Optimal cooling rates in the presence and absence of cryoprotective agents determined using a novel calorimetric method. Biol Reprod 66: 222–231.

50. Oegema TR et al, 2000, A simple cryopreservation method for the maintenance of cell viability and mechanical integrity of a cultured cartilage analog. Cryobiology 40: 370–375.

51. Petakov M et al, 2000, The influence of different cryopreservation protocols on the recovery and engraftment potential of hematopoietic stem and progenitor cells. Exp Hematol 28: 78–79.

52. Bravo D et al, 2000, Effect of storage and preservation methods on viability in transplantable human skin allografts. Burns 26: 367–378.

53. Zhang T, Rawson DM, 1995, Studies on chilling sensitivity of zebrafish (Brachydanio rerio) embryos, Cryobiology 32:239–246.

54. Karlsson JO, Toner M, 1996, Long term storage of tissues by cryopreservation: critical issues, Biomaterials, 17 (3): 243-256

55. Armitage WJ, Mazur P, 1984, Toxic and osmotic effects of glycerol on human granulocytes, The Am. J. Physio. 247 (5): 382-389.

56. Balasubramanian SK et al, 2007, Thermal injury prediction during cryoplasty through in vitro characterization of smooth muscle cell biophysics and viability, An. Biomed. Eng. 36 (1): 86-101.

57. Balasubramanian SK et al, 2006, Water transport and IIF parameters for a connective tissue equivalent, Cryobiology 52:62–73.

58. Berrada MS, Bischof JC, 2001, Evaluation of freezing effects on human microvascular–endothelial cells (HMEC), Cryo Lett., 22: 353–366.

59. Korniski B, Hubel A, 1998, A model of low-temperature water transport for hepatocyte spheroids, Annals of New York, Academy of Sciences 858 (1998) 183–190

60. Pitt RE, Steponkus PL, 1989, Quantitative analysis of the probability of intracellular ice formation during freezing of isolated protoplasts, Cryobiology, 26 (1), 44-63

61. Balasubramanian SK, Coger R, 2005, Heat and mass transfer during the cryopreservation of a bioartificial liver device: a computational model, Asaio J, 51 (3): 184 – 193.

62. Rubinsky B, Eto TK, 1989, Heat transfer with phase transition in biological materials, Cryo Lett., 10: 153–168.

63. Fick A, 1855, Phil Mag, 10 (30).

64. Mayur P, Coger R, 2008, A computational model for predicting intracellular ice formation in bioartificial liver devices, Dissertation, UNCC.

65. Oxytoby DW, 1992, Homogenous nucleation: theory and experiment, J. Phys.: Condens. Matter 4 7627

66. Mazur P, 1963, Kinetics of water loss from cells at subzero temperature and the likelihood of intracellular freezing, J general Physiology, 47: 347-369

67. Southard JH, Belzer FO. 1995, Organ preservation. Annu Rev Med 46: 235–247

68. Rypka M et al, 2006, A novel simplified ultra-freezing technique for cryopreservation of tissue slices, Cryobiology, 52: 193-199

69. Wang W, Ben R, 2004, Upregulation and protein trafficking of aquaporin-2 attenuate cold induced osmotic damage during cryopreservation, In Vitro Cell Dev. Biol. – Animal, 40: 67-70

70. Edashige K, Yamaji Y, Kleinhans FW, Kasai M, 2003, Artificial expression of aquaporin 3 improves the survival of mouse oocyte after cryopreservation, Biol. Reproduction, 68: 87-94

71. Hagedorn M et al, 2002, Altering fish embryos with aquaporin-3: An essential step toward successful cryopreservation, Biol. Reproduction, 67: 961-966

72. Abbeel EV et al, 2007, Osmotic responses and tolerance limits to changes in external osmolalities and oolemma permeability characteristics, of human in vitro matured MII oocytes, Human Reproduction, 22 (7): 1959-1972

73. Finkelstein A, 1987, Water movement through lipid bilayers, pores, and plasma membranes, Theory and Reality, Wiley.

74. Verkman AS et al, 1996, Water transport across mammakian cell membrane, Am. J. Cell Physiol., 270 (1): C12-30.

75. Borgnia M, Nielsen S, Engel A, Agre P, 1999, Cellular and molecular biology of aquaporin water channels, Annu. Rev. Biochem, 68: 425–458

76. Philip BN, Yi S, Elnitsky MA, Lee RE, 2006, Aquaporins play a role in desiccation and freeze tolerance in larvae of the goldenrod gall fly, Eurosta solidaginis, J Exp. Bio. 211: 1112-1119

77. Gradilone SA et al, 2005, Expression and subcellular localization of aquaporin water channels in the polarized hepatocyte cell line WIF-B, BMC Physiol.: 5-13.

78. Hashem M, 2010, Biochemical and expression studies on aquaporin 9 in wild and AQP9 knockout mice, Veterinarski Arhiv. 80 (1): 93-112.

79. Carbrey JM et al, 2003, Aquaglyceroporin AQP9: Solute permeation and metabolic control of expression in liver, PNAS, 100 (5): 2945-2950.

80. Garcia F et al, 2001, The water channel aquaporin-8 is mainly intrcellular in rat hepatocytes and its plasma membrane insertion is stimulated by cyclic AMP, J Biol Chem., 276 (15): 12147-12152

81. Yang B, Zhao D, Verkman AS, 2006, Evidence against functionally significant aquaporin expression in mitochondria, J boil. Chem., 281 (24): 16202-16206

82. Burton SG, 2001, Development of bioreactors for application of biocatalysts in biotransformations and bioremediation, Appl. Chem., 73(1): 77-83.

83. Bartolo DL, Schweder JG, Haverich A, Bader A, 2000, A novel full-scale flat membrane bioreactor utilizing porcine hepatocytes: cell viability and tissue-specific functions, Biotech Prog. 16: 102-108.

84. Niklason LE, Langer R, 2001, Prospects for organ and tissue replacement, J Am Med Asso. 285(5): 573-576.

85. Maguire P et al, 2000, Bioartificial organ support for hepatic, renal and hematologic failure, Critical Care Clinics. 16(4): 681-694.

86. Dore E, Legallais C, 1999, A new concept of bioartificial liver based on a fluidized bed bioreactor, Ther Apher. 3:264 -267.

87. Kawada M et al, 1998, Massive culture of human liver cancer cells in a newly developed radial flow bioreactor system: ultrafine structure of functionally enhanced hepatocarcinoma cell lines, In Vitro Cell Dev Biol Anim. 34: 109-115.

88. Martin Y, Vermette P, 2005, Bioreactors for tissue mass culture: Design, characterization, and recent advances, Biomaterials. 26(35): 7481-7503.

89. Radisic M, Malda J, Epping E, Geng WL, Langer R, Vunjak-Novakovic G, 2006, Oxygen gradients correlate with cell density and cell viability in engineered cardiac tissue, 93(2): 332-343.

90. Brown DA et al, 2007, Analysis of O2 Transport in a Diffusion-Limited Model of Engineered Heart Tissue, Biotech. Bioeng. 97: 962-975.

91. Shames IH, 1982, Mechanics of fluid, MacGraw-Hill.

92. Subramanian RM, Chandel N, Budinger GR, Schumacker PT, 2007, Hypoxic conformance of metabolism in primary rat hepatocytes: A model of hepatic hibernation. Hepatology. 45 (2): 455-464.

93. Sardonini A, Dibiasio D, 1992, An investigation of the diffusion-limited growth of animal cells around single hollow fibers. 40(10)\: 1233\-1242.

94. Roy P et al, 2001, Analysis of O2 Transport to Hepatocytes in a Flat-Plate Microchannel Bioreactor, Annals of Biomed Engg. 29\: 947\-955.

95. Sikavitsas VI, Bancroft GN, Mikos AG, 2002, Formation of three-dimensional cell/polymer constructs for bone tissue engineering in a spinner flask and a rotating wall vessel bioreactor. J of Biomed matr res. 62(1): 136-148.

96. Granet C et al, 1998, Rotating-wall vessels, promising bioreactors for osteoblastic cell culture: comparison with other 3D conditions. Cell Engg. 3: 512-519.

97. Reynolds O, 1874, On the extent and action of the heating surface of steam boilers, Proc. Manchester Lit. Phil. Soc. 8.

98. Steeman HJ, Janssens A, Paepe MD, 2009, On the applicability of the heat and mass transfer analogy in indoor air flows. International Journal of Heat and Mass Transfer. Intnl J. Heat and Mass Transfer, 52(5-6): 1431-1442.

99. Incropera FP, DeWitt DP, 1996, Fundamentals of Heat and Mass Transfer, John Wiley & Sons, New York.

100. Lagerlund TD, Low PA, 1991, Axial diffusion and Michaelis-Menten kinetics in oxygen delivery in rat peripheral nerve, Am. J. Physiology. 260(2.2): 430-440.

101. McGoron AJ, Nair P, Schubert RW, 1997, Michaelis-Menten kinetics model of oxygen consumption by rat brain slices following hypoxia. Annals of Biomedical Engg. 25(3): 565-572.

102. Michaelis L, Menten M.L, 1913, The kinetics of invertase activity, Biochemistry. 49: 333-369.

103. Winter A, 2003, Cartilage like gene expression in differentiated human stem cell spheroids: A comparison of bone marrow–derived and adipose tissue–derived stromal cells arthritis and rheumatism, Arthritis Rheum. Volume: 48 Issue: 2, p. 418-425

104. Alley M et al, 1988, In Vivo and in Vitro Enhanced Antitumor Effects by Pentoxifylline in Human Cancer Cells Treated with Thiotepa, Cancer Res. 48; 4375

105. Polge C, Smith A.U, Parkes A.S,1949, Revival of spermatozoa after vitrification and dehydration at low temperature, Nature, 164, pp. 666–676

106. Meryman M, 1974, Freezing Injury and its Prevention in Living Cells, Annual Review of Biophysics and BioEngg Vol. 3: 341-363

107. Farrabt and Ashwood- Smith, 1980; Cryobiology; Cryopreservation of organs, tissues, etc, Pitman Medical

108. Rall WF, Fahy GM, 1985, Ice-free cryopreservation of mouse embryos at -196 degrees C by vitrification. Nature (journal) 313 (6003): 573–575

109. Mazur P., 1984, Freezing of living cells: mechanisms and implications, Am. J. Gen Phys 247, C125–C142.

110. Scheiwe M W, Korber C., 1983, Basic investigations on the freezing of human lymphocytes, Cryobiology 20, 257–273.

111. Toner M, Tompkins R G, Cravalho E G, Yarmush M L, 1992, Transport phenomena during freezing of isolated hepatocytes, AICHE Journal 38 1512–1522.

112. Yarmush M.L. et al, 1992, Hepatic tissue engineering: development of critical technologies, Annals of New York Academy of Sciences 665, 238–252.

113. Armitage W.J., Juss B.K., 1996, The influence of cooling rate on survival of frozen cells differs in monolayers and in suspensions, Cryoletters 17, 213–218.

114. Acker J.P. et al, 1999, Intracellular ice formation is affected by cell interactions, Cryobiology 38, 363–371.

115. Irimia D, Karlsson J.O.M., 2002, Kinetics and mechanism of intercellular ice propagation in a micropatterned tissue construct, Biophysical Journal 82, 1858–1868.

116. KR Diller, JF Raymond, 1990, Water transport through a multicellular tissue during freezing: a network thermodynamic modeling analysis, Cryo Lett, 11, pp. 151–162

117. L.E. McGann, M Stevenson, K Muldrew, N Schachar, 1988, Kinetics of osmotic water movement in chondrocytes isolated from articular cartilage and applications to cryopreservation, J Orthop Res, 6, pp. 109–115

118. Minkowycz WJ, Sparrow EM, 1996, Advances in numerical heat transfer, Taylor and Francis publication, Vol 1.

119. Shih TM, 1984, Numerical heat transfer, Taylor and Francis publication.

120. Karlsson JO et al, 1993, Nucleation and growth of ice crystals inside cultured hepatocytes during freezing in the presence of dimethyl sulfoxide, Biophy. J, 65 (6): 2524-2536

121. R.L. Levin, E.G. Cravalho, C.E. Huggins, 1976, A membrane model describing the effect of temperature on the water conductivity of erythrocyte membranes at subzero temperatures, Cryobiology 13, 415–429.

122. Karlsson JO, Cravalho EG, Toner M, 1994, A model of diffusion limited ice growth inside biological cells during freezing, AIP: 4442-4455

123. Crank J, Nicolson P, 1947, A practical method for numerical evaluation of solutions of partial differential equations of the heat conduction type, Proc. Camb. Phil. Soc. 43 (1): 50–67

124. Hageman L. and Young, D, 1981, Applied Iterative Methods. New York: Academic Press.

125. Jeffreys H. and Jeffreys, 1988, B. S. Methods of Mathematical Physics, 3rd ed. Cambridge, England: Cambridge University Press, pp. 305-306, 1988.

126. Seglen P.O.,1976, Preparation of isolated rat liver cells. Methods in cell biology, 13: p. 29-83.

127. DeCarlo, R, 1989, Linear Systems: A State Variable Approach with Numerical Implementation, Prentice Hall, NJ.

128. Kotsiantis S, Kanellopoulos D, 2006, Discretization Techniques: A recent survey, GESTS International Transactions on Computer Science and Engg, Vol.32 (1), pp. 47-58

129. Sum AK, Pablo JJ, 2003, Molecular simulation study on the influence of dimethylsulfoxide on the structure of phospholipid bilayers, Biophy. J, 85(6): 3636–3645.

130. Carey HV, et al., 2003, Mammalian hibernation: Cellular and molecular responses to depressed metabolism and low temperature, Physiol Rev, 83 (4): 1153-1181.

131. Dantzig JA, 1989, Modeling liquid–solid phase changes with melt convection, Int. J Num. Meth. Eng. 28 (8): 1769–1785.

132. Voller VR, Prakash C, 1987, A fixed grid numerical modelling methodology for convection-diffusion mushyregion phase-change problems, Int. J Heat and Mass Transfer, 30 (8): 1709–1719.

133. Smith DJ, Schulte M, Bischof JC, 1998, The effect of dimethylsulfoxide on the water transport response of rat hepatocytesduring freezing, J Biomech. Eng. 120 (5): 549-558

134. Nui M, Coger R, 2008, Engineering liver tissue devices for enhanced transport, improved function and storage, PhD dissertation, UNC Charlotte.

135. Irimia D, Karlsson JO, 2005, Kinetics of intracellular ice formation in one-dimensional arrays of interacting biological cells, Biophy. J. 88 (1): 647-660

136. Toner M, Ernest GC, Marcus K, 1990, Thermodynamics and kinetics of intracellular ice formation during freezing of biological cells, AIP: 1582 – 1593.

137. Harris CL, et al., 1991, Cryopreservation of isolated hepatocytes: intracellular ice formation under various chemical and physical conditions, Cryobiology, 8(5):436-44

138. Hubel A, et al., 1991, Intracellular ice formation during the freezing of hepatocytes cultured in a double collagen gel, Biotechnol Prog. 7 (6):554-559.

139. Wolkers WF, et al., 2007, Effects of freezing on membranes and proteins in LNCaP prostate tumor cells, Biochimica et biophysica acta, 1768 (3): 728-736.

140. Huebert RC, et al., 2002, Expression and localization of aquaporin water channels in rat hepatocytes. Evidence for a role in canalicular bile secretion, J Biol Chem. 277: 22710-17.

141. Calamita G, et al., 2001, Expression and immunolocalization of the aquaporin-8 water channel in rat gastrointestinal tract. Eur J Cell Biol, 80: 711-719.

142. Elkjaer ML, et al., 2001, Immunolocalization of aquaporin-8 in rat kidney, gastrointestinal tract, testis, and airways, Am J Physiol, 81: F1047-57.

143. Tani T, et al., 2001, Immunolocalization of aquaporin-8 in rat digestive organs and testis. Arch Histol Cytol, 64: 159-68.

144. Elkjaer ML, et al. 2000, Immunolocalization of AQP9 in liver, epididymis, testis, spleen, and brain, Biochem Biophys Res Commun., 276: 1118-28.

145. Nicchia GP, et al., 2001, Tissue distribution and membrane localization of aquaporin-9 water channel: evidence for sex-linked differences in liver, J Histochem Cytochem 49: 1547-56.

146. Soria L, Gradilone SA, Larocca CM, Marinelli RA, 2009, Glucagon induces the gene expression of aquaporin-8 but not that of aquaporin-9 water channels in the rat hepatocyte, Am J Physiol Regul Integr Comp Physiol 296: R1274–R1281.

147. Livak KJ, Schmittgen TD, 2001, Analysis of relative gene expression data using real-time quantitative PCR and the 2(-Delta Delta C(T)) Method, Methods, 25 (4):402-408.

148. Barber RD, Harmer DW, Coleman RA, Clark BJ, 2005, GAPDH as a housekeeping gene: analysis of GAPDH mRNA expression in a panel of 72 human tissues, Genomics, 21 (3): 389-395

149. Gradilone SA, 2003, Glucagon induces the plasma membrane insertion of functional aquaporin-8 water channels in isolated rat hepatocytes, Hepatology, 37(6): 1435-1441.

150. Majno G, Joris I, 1995, Apoptosis, oncosis, and necrosis. An overview of cell death, Am J Pathol. 146(1): 3–15.

151. Stoll B, Gerok W, Lang F, Häussinger D, 1992, Liver cell volume and protein synthesis. Biochem. J, 287(1): 217–222.

152. Heidebrecht F,et al., 2009, Improved protocols for protein and RNA isolation from three-dimensional collagen sandwich cultures of primary hepatocytes, Anal Biochem. 2009 393(1):141-144.

153. Gradilone SA, et al., 2002, Hepatocyte membrane water permeability measured by silicone layer filtering centrifugation, Analytical Biochem. 302: 104–107

154. Uryasha VF, et al., 2006, Heat capacity and physical transitions in collagen and solubility of water in it, Russian J. Gen. Chem., 76 (9): 1363-1367.

155. Lide DR, 1999, CRC Handbook of Chemistry and Physics, Ed. 80.

156. Wilke CR, Chang P, 1955, Correlation of diffusion coefficients in dilute solutions, A.E.CH.E. J., 1: 264-270.

157. Rotem A, Toner M, Tompkins R, Yarmush M, 1992, Oxygen uptake rates in cultured rat hepatocytes, Biotechnol Bioeng 40: 1286–1291.

158. Pazhayannur PV, Bischof JC, 1997, Measurement and simulation of water transport during freezing in mammalian liver tissue, J. Biomech. Eng., 119 (3): 2669-277.